Vehicle Safety Institute

Christoph Drießen, BSc

Investigation of Lithium plating in LIBs using non-destructive electrochemical methods

MASTER'S THESIS to achieve the university degree of

Diplom-Ingenieur

Master's Degree Program: Mechanical Engineering and Business Economics

Submitted to

Graz University of Technology

Supervisor: Ass.Prof. Priv.-Doz. Dipl.-Ing. Dr.techn. Christian Ellersdorfer

Co-Supervisor: MSc Syed Muhammad Abbas

Vehicle Safety Insitute

Graz, 09th of October 2023

ABSTRACT

Replacing fossil fuels with electricity is a promising solution to reduce the amount of greenhouse gas emissions in the transport sector. Lithium-ion batteries (LIBs) are one of the most promising electrical energy storage systems. During their use as a power source in electric vehicles, different ageing mechanisms take place inside and influence their lifetime. One of the most detrimental is lithium plating (LP) on the graphite anode surface. After arising under special boundary conditions like low temperatures, high C-rates and a high state of charge it not only boosts a further degradation, it may also have a negative impact on the safety of LIBs. For this reason, this thesis deals with the identification of different boundary conditions facilitating LP in high-energy lithium-ion pouch cells. Further motivation is the identification of this ageing mechanism with non-destructive methods. Voltage relaxation profiles, differential voltage analysis, incremental capacity analysis and anode potential measurements are analysed for usage in high energy cells.

In the experimental section commercial pouch cells are cycled based on a designed test matrix with C-rates from 1C to 3C and temperatures from 0 °C to 22 °C. With the help of the identification methods, critical boundary conditions are identified to induce LP. Based on this, additional cells are cycled to a SoH of 80 % for further studies.

In the cycling section it becomes visible, that LP is a favour reaction for increasing C-rates and decreasing temperatures. For both boundary conditions, the cells showed a higher sensitivity to temperatures rather than for the charging rate. With a cycling temperature of 10 °C in combination with 1.5C clear signs of LP are visible, for 0 °C it occurs also with 1C. During the use of high C-rates other mechanisms, which affect the amount of LP must be taken into account during the cell cycling.

To analyse LP in commercial high energy pouch cells the differential voltage analysis and incremental capacity analysis successfully show visible signs for the onset of LP. The voltage relaxation profiles show clear lithium stripping plateaus in the cell voltage, but combined with the anode potential measurement this method is called in question, where the relaxation plateaus are ascribable to the positive electrode. Further, the anode potential measurement in commercial cells with non-pure graphite anodes should be considered carefully while using, because this method did not show the characteristic sign for LP.

ACKNOWLEDGEMENTS

At this point I would like to thank my supervisors, Dipl.-Ing. Dr.techn. Gregor Gstrein and MSc Syed Muhammad Abbas, for the support, expertise and guidance throughout my Master's thesis journey. I am deeply grateful for your motivation, the insightful and constructive comments and suggestions.

Thank you to Univ.-Prof. Dipl.-Ing. Dr.techn. Hermann Steffan for the opportunity to complete my thesis at the Vehicle Safety Institute, to Dipl.-Ing. Dr.techn. Jörg Moser and Ass.Prof. Priv.-Doz. Dipl.-Ing. Dr.techn. Christian Ellersdorfer for the use of the facilities in the Battery Safety Center Graz and to Ass.Prof. Priv.-Doz. Dr. Ilie Hanzu for the support and discussions during the evaluation of the results.

My thanks also go to all employees of the Vehicle Safety Institute and the Battery Safety Center Graz. The camaraderie, shared knowledge, and collaborative spirit made the working environment enriching. Your insights and discussions were instrumental in shaping my research.

I would also like to thank my parents and my brother for the endless encouragement over all the years and the belief in my abilities. Your constant support throughout not only my studies, but my entire life has been a big motivation for me. Without you I would not be where I am today.

Thanks also to my friends for the support and the understanding, especially during weeks of studying all day. I am thankful for the days and nights you distracted me from the stressful university life and sharing personal moments with me during this journey.

A special thank you goes to my girlfriend Victoria that you accompanied me on this path and being there for me during the challenging moments of this journey. Your love, patience, and understanding in stressful times made this journey a lot easier for me.

TABLE OF CONTENTS

LIST OF FIGURES

LIST OF TABLES

1 INTRODUCTION

The reduction of greenhouse gas emissions is one of the main topics facing the transport sector today. Transport electrification, which means replacing fossil fuels with electricity as the main power source, is a promising solution and more and more electric vehicles (EVs) have been developed by numerous manufacturer [1]. Due to the increasing number of EVs on the global car market [2], a broad application of diverse energy storage and conversion technologies becomes even more important. One of the most promising electrical energy storage system to meet the wide range of requirements of electric vehicles are lithium-ion batteries (LIBs) [1]. Their unique benefits, such as high energy density, high power density and good cycling performance make them favorite for use in automotive applications [3], [4]. It should be explained that an EVs battery pack is an interconnection of several cells in series and parallel connections forming the battery pack [5]. A typical lithium-ion cell structure is shown in the following Figure 1.1. It consists of a positive (cathode) and negative (anode) electrode with a separator and electrolyte between [1]. To form the negative electrode, graphite as a layered structure active material is coated on a copper current collector. Metal-oxide like Nickel-Mangan-Cobalt (NMC) or Lithium-Iron-Phosphate (LFP) are common crystal structured active materials which are coated on an aluminium current collector to form the positive electrode [1].

During cell assembly these components put together in several layers to different types of cells. Most common types nowadays are pouch, cylindrical, or prismatic cells [6]. Every type has its own characteristic features with regard to the manufacturing process, the materials used and the cell properties. In this thesis only pouch cells are examined and therefore care should be taken when making possible comparisons with other cell types. Lithium-ion cells work on the principle of the galvanic cell with charging and discharging cycles [7]. During a charging process, illustrated in Figure 1.1, electrons e^- move through the external circuit by the charger from the cathode to the anode. In the same time Li-ions de-intercalate out of the cathode, then transfer through the electrolyte to the anode and intercalate into the graphite [1], [8]. During the discharge process, the reverse reaction happens, Li-ions de-intercalate from anode and are transferred towards cathode, giving up e^- to the external circuit [8]. The task of the porous separator between the electrodes is to avoid an internal short circuit, hold the electrolyte and only allows the Li-ions in the electrolyte to pass through [9]. Due to cyclic

application, means charging and discharging the cell, calendric storage, and use under different environmental conditions, ageing mechanisms can take place at the previous mentioned components and influence the lifetime of a lithium-ion cell [10]. Side reactions, structural changes, materials losses, or consumed electrolyte are some predominant mechanisms resulting in a reduction of power and capacity at the end of the battery's life [11]. Therefore the understanding of different ageing and degradation mechanisms leading to either capacity or power loss becomes more and more important to make EVs commercially viable. Concerning the ageing mechanisms in LIBs, the deposition of metallic lithium on anode, also known as lithium plating (LP), is one of the most detrimental ageing mechanism [1], [3], [12]. LP occurs under special boundary conditions (BCs) on the surface of the graphite anode. It not only exacerbates degradation but can also compromise the safety of lithium-ion batteries (LIBs) [3]. For this reason, understanding the mechanisms of LP as an ageing mechanism becomes even more important. The mentioned BCs which are favorable for the deposition of metallic lithium are low temperatures, high charging currents and a high state of charge (SOC) [3], [11], [12], [13], [14]. Extensive research is being conducted into detection and characterization techniques to better understand this phenomenon and increase the safety during use of lithium-ion batteries. This thesis gives an overview of the ageing mechanisms happen in lithium-ion batteries and covers the topic of lithium plating in more detail. Therefore, the investigation of LP using analytical methods in commercially available higher energy LIBs is the main focus of this thesis.

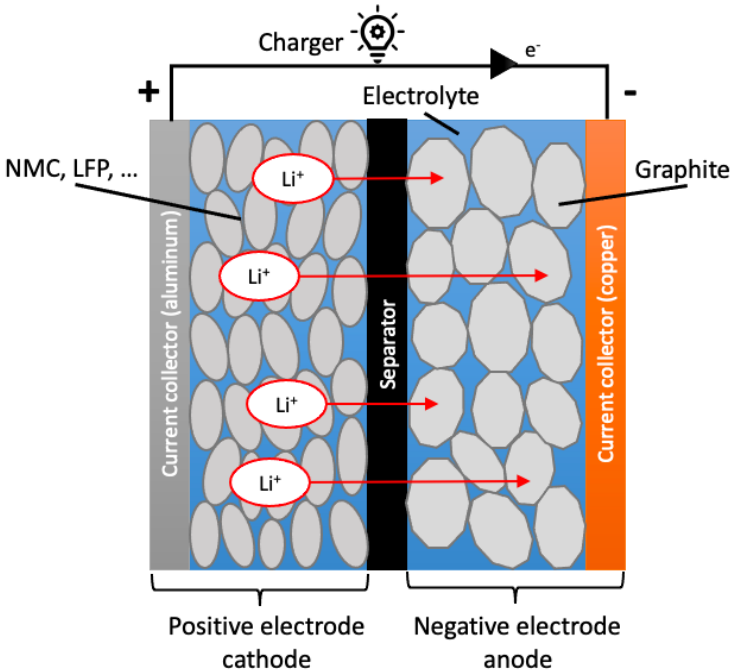

Figure 1.1: Structure of a lithium-ion cell (replication of [6])

1.1 Review of Literature

Cycling at different temperatures and self-recovery capability are some critical challenges for lithium-ion batteries to become more commercially viable [1]. Based on different environmental and usage conditions, complex physical and chemical mechanisms take place inside the cell and lead to a reduction of the cell capacity (capacity fade) and the cell power (power fade) [11]. This change in properties can be described by the ageing. An estimation factor for the ageing degree of a cell is for example the State-of-Health (SoH) [15]. The SoH describes the actual condition of the battery compared to a new battery [6]. In addition to the effected lifetime of the cell the safety performance is another critical aspect to be taken into account. Because of the complex behavior, the identification and understanding of the different ageing and degradation mechanisms are one of the most challenging goals [1]. According to literature the main degradation modes of LIBs can be split up into three parts: loss of lithium inventory (LLI), loss of active material on the negative electrode (LAM_{NE}) and loss of active material on the positive electrode (LAM_{PE}) [16], [10]. The loss of electrolyte (LE) is another degradation mode, which only occurs in connection with the modes above and is therefore not declared as a fourth. Following Figure 1.2 shows the main degradation mechanisms, which happens inside a cell, leading to the mentioned three degradation modes.

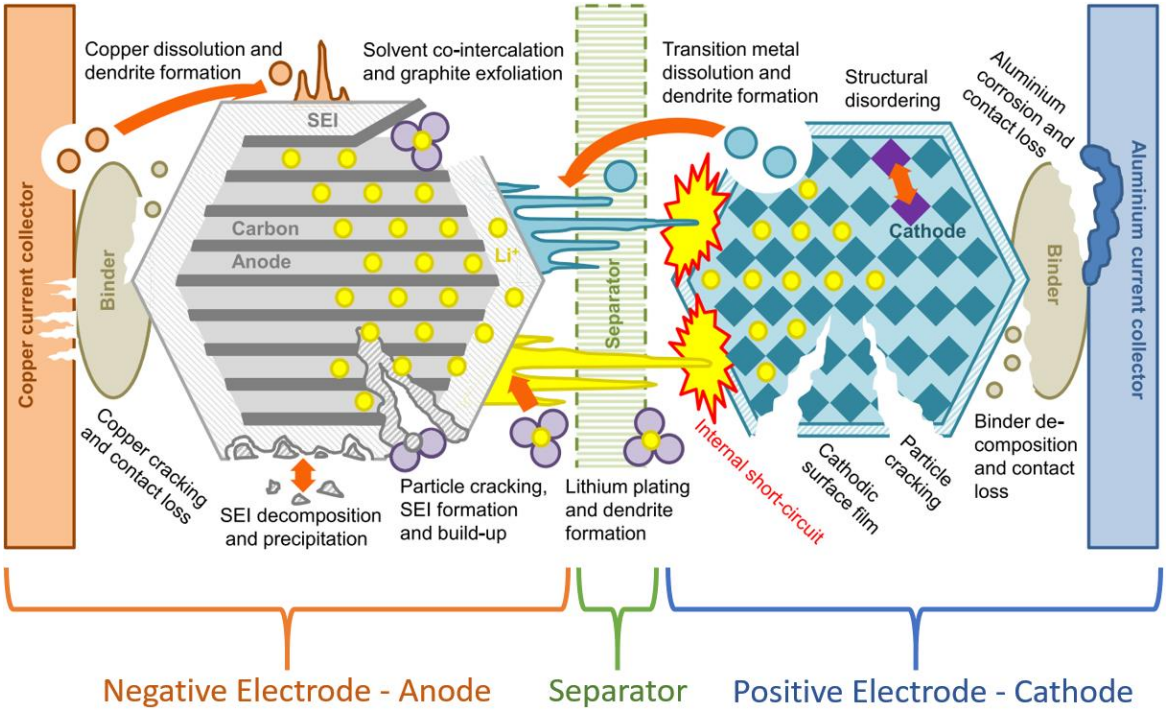

Figure 1.2: Different degradation mechanism in lithium-ion cells [10]

In the first case of LLI, side reactions can lead to a capacity fade, because the lithium ions are no longer available for the intercalation process [10]. An example for this degradation mode is the formation of the so called solid electrolyte interphase (SEI) at the surface of the anode active material [17]. This layer is formed in the first charging cycle of every lithium-ion cell due to consumption of the electrolyte in combination with a loss of lithium inventory [17]. It allows the transport of Li-ions and prevent further electrolyte decomposition [16], [17]. During usage in high temperature conditions, a decomposition of the SEI can happen and lead to an additional layer formation at the new uncoated sites which leads to further degradation [1], [10], [11]. LLI also occur as a result of irreversible lithium plating, also known as “dead lithium” [1], [3], [13]. This specific ageing mechanism will be described in more detail in the following paragraph.

A loss of active material on both electrode sides can arise due to high mechanical stress and current load [10]. Particles crack out of the active material or the active material can lose electric contact with the current collector [6], [10], [11]. The binder material decomposition and the corrosion of the current collectors are further mechanisms which are assigned to LAM [10]. All of this loss of active material leads to a reduction of the capacity and power of the cell. With a detailed look only at the active material of the positive electrode, high current loads can induce a LAM_{PE} due to a structural disordering of the material [4], [11], [10]. In this specific case, the insertion of lithium on the positive side is no longer possible and the capacity is reduced [10]. A typical degradation mechanism leading to LAM_{NE} and LLI is lithium plating [10]. Favored conditions for this deposition of metallic lithium are low temperatures, high current rates and high state of charge (SOC) [3], [11]-[14]. In severe cases this deposition can lead to a dendrite formation, pierce the separator and results into a short circuit with following thermal runaway [1], [3]. It not only boosts a reduction of capacity and power, it is an even more important point while looking at the safety aspect. Therefore, this phenomena will be discussed in more detail in the following chapters.

Overall, the battery ageing can be described as a combination of multiple complex mechanism based on material parameters, as well as the condition under cycling and storage, reducing their lifetime [11].

1.2 Motivation

As part of the before mentioned ageing mechanism, lithium plating can occur under special cycling and environmental conditions. Next to its reduction of capacity and power, the safety aspect of the dendrite formation becomes even more important for this specific ageing mode. Therefore, the motivation of this thesis is the identification of different boundary conditions facilitating lithium plating in high-energy lithium-ion pouch cells. Different non-destructive electrochemical methods should deal as an analyses tool to identify and quantify the amount of lithium plating during cycling. This should lead to more real-world application-related understanding of when, where, why and how much lithium is deposited on the graphite anode surface of commercial used lithium-ion cells. Further motivation is the possibility to induce lithium plating in commercial high energy cells for subsequent study and questions, like the difference in the mechanical behaviour during a crash in comparison with a fresh cell.

1.3 Objectives

The goal of the thesis is the study of lithium plating in commercial available high energy cells. After start with a literature review on ageing mechanisms, a theoretical background of the phenomena of lithium plating and different investigation methods, specific boundary conditions should be determined to induce LP under laboratory conditions in the Battery Safety Centre Graz (BSCG). The following experimental part describes the cycling of commercial lithium-ion pouch cells under the predetermined boundary conditions to induce lithium plating and analyses of the cycle data with specific non-destructive identification methods. For this thesis the following objectives are defined:

- Experimental investigation on lithium plating (LP) in commercial pouch LIBs
- Identification of boundary conditions for targeted production of LP in commercial LIBs
- Application of those BCs on fresh and aged LIBs to induce LP for investigation.
- Data acquisition, evaluation and correlation of the results
- Comparison of test results based on non-destructive electrochemical methods

2 LITHIUM PLATING

Complex physical and chemical mechanisms take place inside a lithium-ion cell during usage and can influence their lifetime [10]. Capacity losses, power losses and also a difference in the safety performances are outcomes of this change in properties, which is referred to the ageing of the cell [10], [11], [14]. As part of the previously mentioned ageing mechanisms, one of the most detrimental is the deposition of metallic lithium [1]. This phenomena occurs at the graphite anode surface during the charging process and is favored by low temperatures, high charging currents and a high state of charge (SOC) [3], [11]-[14]. These conditions may drop the anode potential below 0 V vs. Li/Li^+ during charging and make lithium plating thermodynamically possible [13]. Besides the capacity loss of LP due to the LLI, this can lead to a growth of so called “dendrites” [1], [18]. In the worst case scenario this formation of deposited lithium metal can pierce the separator and induce a short circuit of the cell [18]. Followed by an increase in cell temperature the thermal runaway is the most fatal outcome [19]. Different application conditions can define different morphologies of lithium plating during appearance and split it up in reversible and irreversible parts [1], [3], [13]. In the following paragraphs the occurrence and favorable conditions will be described in more detail. Followed by the safety factor, different identification methods are discussed to sum up the topic of lithium plating.

2.1 Charging Transfer

Lithium plating goes along with the charging process of a LIB. Figure 2.1 shows the structure of a typical lithium-ion cell with the intercalation process during charging [1]. In the charging process Li-ions de-intercalate out of the cathode, then transfer through the electrolyte to the anode and intercalate into the graphite sides [1], [3], [13]. The intercalation process, can be split up in three parts: 1.) Li-ions diffuse out of the cathode, 2.) Diffusion of solvated Li-ions in the electrolyte, and 3.) De-solvated Li-ions pass the solid electrolyte interface (SEI) and intercalate in the anode active material - also known as charge transfer process [1], [3], [20], [21]. This third part can be broken into three sub processes: i.) Li-ions strip off their solvation shell (de-solvation), ii.) De-solvated (naked) Li passing through the SEI, and iii.) Solid-state diffusion into graphite [1]. Charging at high currents, low temperatures or high SOC can

influence this charge transfer and solid diffusion processes and lead to lithium plating instead of Li-ion intercalation [3], [12], [20]-[22] In the following chapter this reaction and also a classification of the plated lithium metal is discussed in more detail.

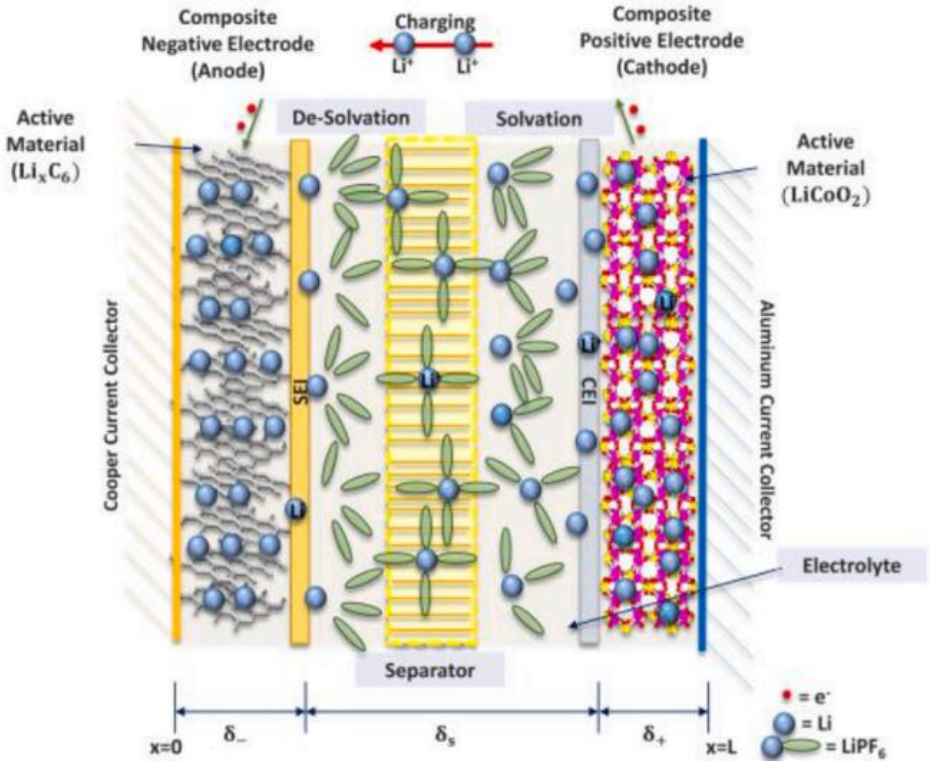

Figure 2.1: Intercalation process during charging of a lithium-ion cell [1]

2.2 Reactions & Classifications

Shown in the previous paragraph, lithium plating goes along with failure in the intercalation process during charging [3], [12], [20], [21]. Following equation (1) shows the complete insertion of Li^+-ions into the graphite anode electrode during charging from left to right, with $0 \leq x + \delta \leq 1$ [1], [3], [22], [23].

$$xLi^+ + Li_\delta C_6 + xe^- \rightarrow Li_{x+\delta} C_6 \quad (1)$$

The intercalation process is a diffusion limited process, means only a certain amount of Li^+-ions can be embedded into the graphite sides per unit time at a given temperature [24]. In connection with LIBs, Li^+-ions can intercalate into graphite at a potential range of 65-200 mV vs. Li^+/Li [22]. Anode potentials below 0 V vs. Li/Li^+ make lithium plating thermodynamically possible [13]. When lithium deposits on the anode surface, it can be described with the

following equation in two directions (2). A partial or full deposition of lithium on the anode surface is shown from left to right [1], [3], [22], [23].Right to left define the stripping process, which is described below in more detail.

$$(1 - X)Li^{+} + (1 - X)e^{-} \rightarrow (1 - X)Li \tag{2}$$

During charging, the current defines the velocity of the Li^{+}-ions coming to the anode surface. Under the condition of lithium deposition, the charging current can be divided into the intercalation current and the lithium plating current [1], [3], [23]. The following

Figure 2.2 describes the process which makes lithium deposition possible [23]. A complete intercalation of Li-ions during charging is shown on the left, with only the intercalation current (green) acting. Li_xC_6 describes the mixture of lithium and graphite. During the central and right figure the charging process continues and the free sites for Li intercalation in the graphite layer decrease. This causes the intercalation current to decrease while the plating current (blue) increases [3]. Due to this, more and more Li^{+} arrive on the graphite anode surface and the transport rate of Li^{+} from electrolyte gets higher than the intercalation rate [1], [3], [23]. This drives the anode potential to drop below 0 V vs. Li/Li^{+} and Li deposition becomes thermodynamically allowed [3], [13].

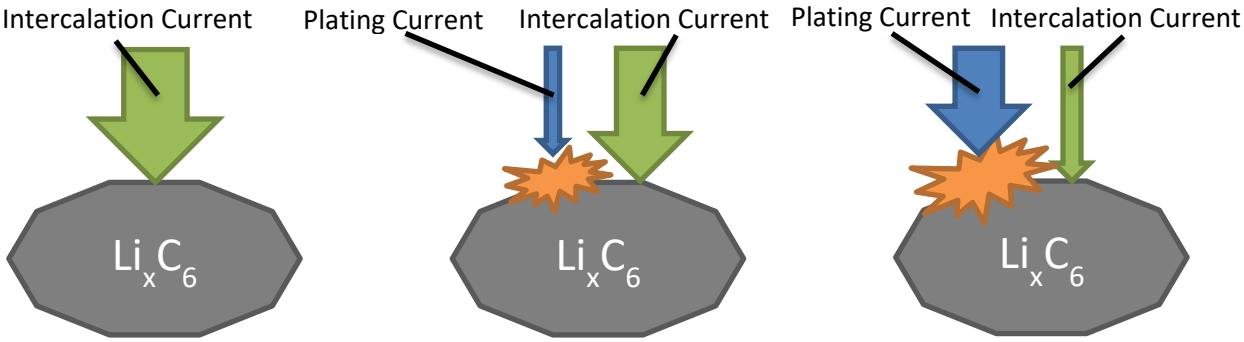

Figure 2.2: Intercalation- & plating current during lithium deposition (replication of [23])

Charging is a dynamic process, where kinetic and thermodynamic factors can lead to a graphite electrode overpotential [13]. The kinetic causes can be split up in three parts: i.) charge transfer, ii.) the mass transfer or electrolyte concentration, and iii.) lithium solid phase in the negative electrode [13], [25], [1]. As already mentioned in the introduction, the thermodynamically favourable conditions are low temperatures, high charging currents (high C-rates), and high SOC [3], [11]-[14]. All these factors cause a polarization of the electrode and

make deposition of lithium possible. Following Figure 2.3 shows the classification of lithium plating and the following reactions during occurrence at the negative electrode. When lithium plating happens, it can be either reversible or irreversible [1], [3], [13]. According to their occurrence, both parts can end up in two reactions. The reversible part can be split up into the reinsertion into graphite and lithium stripping. On the other side, the irreversible part can build a second SEI film or losses electrical contact and form dead lithium [1], [26].

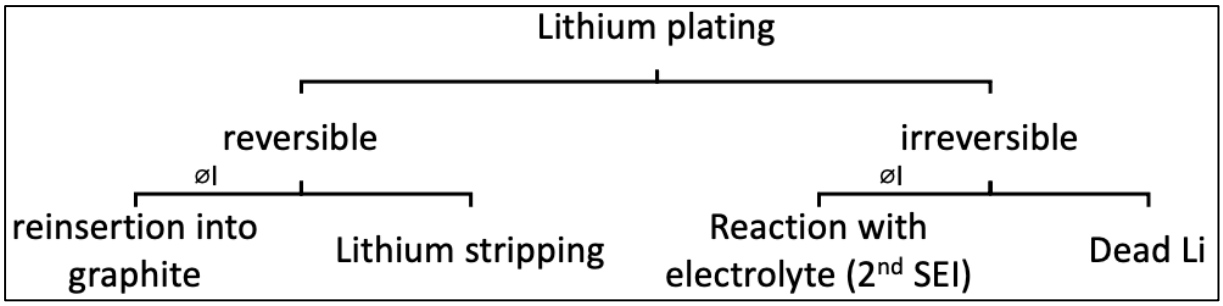

Figure 2.3: Classification of lithium plating during occurrence (replication of [13]

Which type of reaction the plated lithium undergoes after deposition depends on the current and is shown in Figure 2.4. Without any external current (ø I), it may undergo two subsequent reactions. The first reaction is shown in Equation (3), with $\delta + x + \delta \leq 1$. It represents a reinsertion of deposited lithium into the graphite during resting time from left to right and is assigned to the reversible part [1], [3], [22]. Equation (4) shows the reaction of the deposited Li with the electrolyte (R). It often results in a secondary SEI film and therefore it can be assigned to the irreversible part [1], [3], [22].

$$\varepsilon Li + Li_{\delta+x}C_6 \rightarrow Li_{\delta+x+\varepsilon}C_6 \tag{3}$$

$$R + Li \rightarrow R - Li \tag{4}$$

During discharge, with an external current, it also may undergo two subsequent reactions. Equation (5) shows the so called reversible “lithium stripping” where Li goes back in the system through re-intercalation into graphite or transfer back to the cathode [1], [3], [26].

$$Li \rightarrow Li^+ + e^- \tag{5}$$

In addition to the mentioned lithium stripping, there also exists a fourth one which is so called “dead lithium” [27]. It happens when a portion of deposited lithium lost electrical contact with

the graphite. The lithium is no longer available for further charging transfers and therefore it can be assigned to the irreversible part [1], [3], [13], [23], [27].

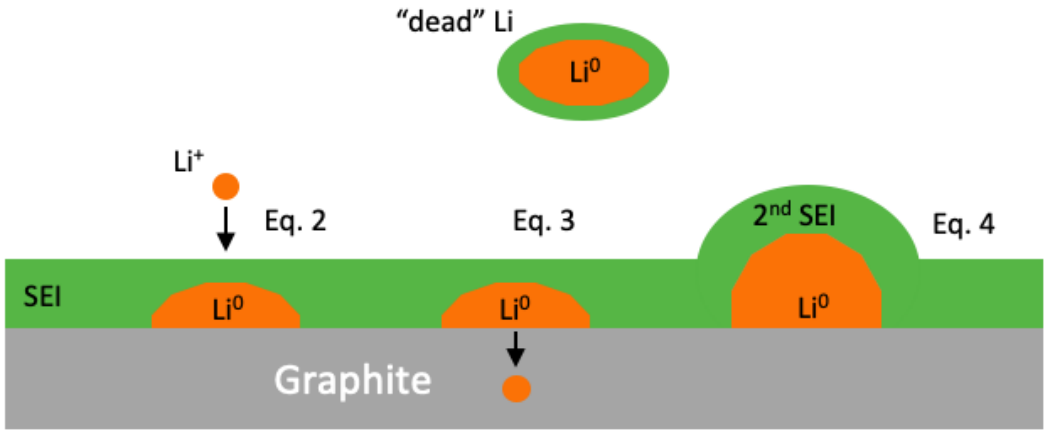

Figure 2.4: Graphic of different lithium deposition classifications (replication of [13], [28], [29])

In addition to the classification into reversible or irreversible, the deposited lithium can be sub-divided into three types of deposition, which are shown in Figure 2.5: i.) homogeneous plating, ii.) local plating, and iii.) marginal plating (on the edges) [3], [13], [23]. The silver colored areas represent the lithium deposition. Working and charging conditions, most depending on the current rate, define these morphologies of plated lithium (Sagane et al. 2013). Homogeneous plating with constant thickness of deposited lithium is more a theoretical ideal conception. If gradients of temperature, SOC, or charging current change during cycling or ageing, it will get inhomogeneous [13], [30]. Local plating tends to occur if lower local temperatures, higher local SOC, higher local current densities, or higher local surface pressure dominate [13], [31]. Marginal plating around the edge of an anode is favoured when the battery design in form of anode-cathode-ratio is too small [13], [32]. Next chapter will discuss the influencing factor for lithium plating in more detail.

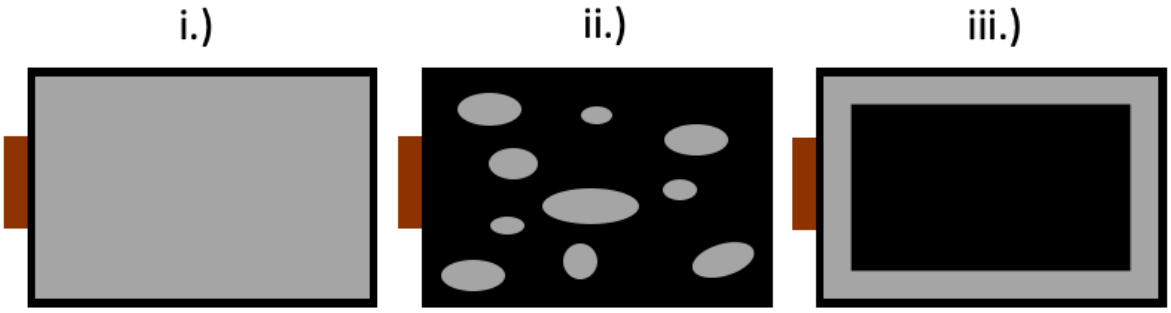

Figure 2.5: Types of lithium deposition on graphite anode surface (replication of [13])

2.3 Factors Affecting Lithium Plating

According to the classifications and different types of lithium plating, it can arise due to influence factors of the charge transfer kinetics in the electrolyte and the solid-state diffusion process [3], [22]. The main parameters which can drop the anode potential below 0 V and make LP possible are low temperatures, high charging C-rates, and high SOC [3], [11]-[14]. Beside these hazardous operation conditions cell defects, localized pressure or overall aging of the cell can lead to lithium plating or promote a deposition on the graphite anode surface [1], [13], [33]. In this chapter the mentioned favourable application conditions are discussed in more detail.

2.3.1 Hazardous Condition - High Charging C-rates

For LIB implementation in EVs, fast charging capability is becoming increasingly important. In order to make this possible, a higher charging current (C-rate) has to be applied. Limits during fast charging are mainly present due to the limited Li^+ insertion process at the graphite anode [1]. Following Figure 2.6 shows the intercalation process of Li-ions in the graphite active material while applying high charging currents. During charging with high C-rates, a lot of Li^+ (orange dots) move from cathode to the graphite anode and accumulate on the interface between the electrode and the electrolyte [1], [13]. While ongoing charging, the charging rate is more likely to exceed the intercalation rate. Therefore, the concentration gradient of Li^+ on the interface rises until it becomes saturated [1]. This leads to a higher anode polarization. The anode potential drops below 0 V vs. Li/Li^+ and lithium plating is thermodynamically possible [1], [3], [13]

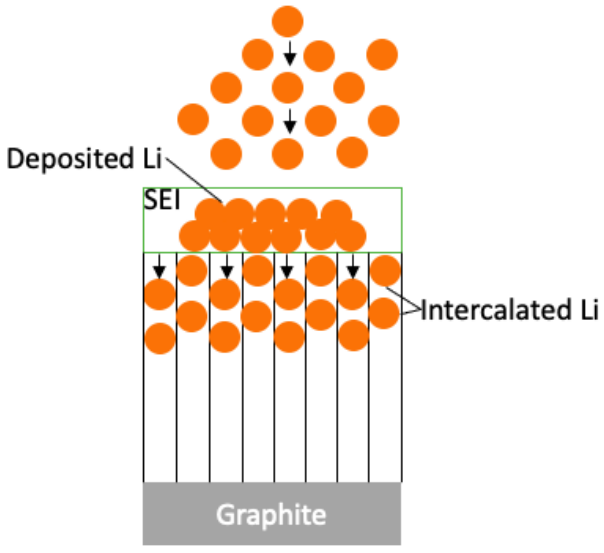

Figure 2.6: Factors affecting LP - high charging C-rates (replication of [1] & [3])

2.3.2 Hazardous Condition - Low Temperature

Acceptable temperatures for LIBs are between -20 °C and 60 °C [34], but the optimal temperature range is between 15 °C and 35 °C [35]. Lower temperatures can influence fast charging, reduce the power and energy output, and favour deposition of lithium on the anode surface [1], [35]. This low temperature performance is caused by two factors: 1.) poor solid diffusivity of lithium-ion in the electrode, and 2.) poor charge-transfer rate [1], [3]. The first factor is influencing the deposition of lithium due to a poor solid diffusivity of Li-ions in the electrode. It becomes more and more favoured when the concentration gradient of Li-ions on the surface rises until it reaches the maximum value [1], [3], [13]. Second limiting factor during low temperature charging is the poor charge transfer rate. The charge transfer, described in the previous chapter, and the ionic conductivity is limited down at low temperatures [36].Therefore, an applied current leads into a large overpotential and an increased anode polarization [1], [3]. The anode potential drops below 0 V vs. Li/Li^+ and lithium plating is thermodynamically possible [13]. Following Figure 2.7 shows the deposition of metallic lithium on the active material due to the slowed down charge transfer with low temperatures. It must be mentioned, that also higher temperatures can lead to accelerated degradation of a lithium-ion cell [1], [3], [13], [35].

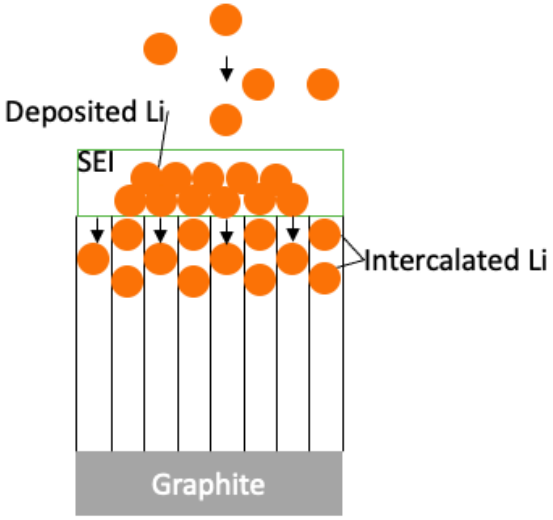

Figure 2.7: Factors affecting LP - low temperature (replication of [1] & [3])

2.3.3 Hazardous Condition - High SOC

For every cell chemistry, there exists an upper and lower cut-off voltage, which is in most cases predefined by the manufacturer. Charging the cell beyond this upper limit is known as “overcharging” (high SOC) [1]. Following Figure 2.8 shows the problem of lithium deposition

with high SOC, where the cell is already full with intercalated Li and the current keeps flowing. The concentration of Li-ions exceeds the limit which the anode can store. Therefore, the concentration gradient of Li^+ on the interface between the electrode and the electrolyte rises [3]. When it becomes saturated the anode potential drops below 0 V vs. Li/Li^+ and lithium plating is thermodynamically possible [1], [3], [13].

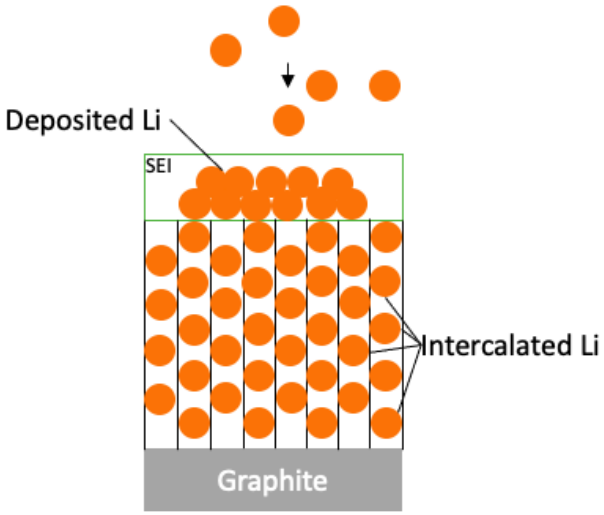

Figure 2.8: Factors affecting LP - high SOC (replication of [1] & [3])

2.3.4 Localized pressure & battery design

Cell defects, a localized pressure or a poor battery design can result in local anode lithium plating due to inhomogeneous distributions of current density and temperature [1], [37], [38]. In connection with the high SOC in the previous section, a too small designed anode/cathode ratio or negative/positive ratio can lead to lithium deposition, because not all available Li-ions can intercalate in the graphite anode [1], [39].

Another critical point could be a cell defect due to localized pressure. Structural changes of the separator in the deformed area can lead to pore closing, which generate high lithium concentration at these sites [1], [37], [38]. This results in high overpotential and make it a favourable nucleation site for LP [1], [33], [37], [38].

2.3.5 Ageing of the cell

The main ageing modes in LIBs are loss of lithium inventory (LLI), loss of active material on the negative electrode (LAM_{NE}) and loss of active material on the positive electrode (LAM_{PE}) [16], [10]. In an aged cell, the deposition of metallic lithium on graphite surface can happen even under normal operation conditions [1], [4]. For example, LAM_{NE} can cause a cell imbalance

and over-lithiation on the graphite surface leading to lithium plating [1]. Overall, ageing during lifetime of a cell can influence the lithium deposition but also lithium deposition can lead to a further boosted degradation [1], [13].

2.4 Safety Relevance of Lithium Plating

In the previous chapters, the focus was on LP in general, the reaction and factors when lithium plating occur. LP not only boosts a further degradation, it may also have a negative impact on the safety of LIBs. One of the most severe case is the formation of so called lithium “dendrites” [1], [18]. This deposited lithium is formed during the charging process and can rise up to a dendrite-like structure. Low temperatures and the thereby slow solid diffusivity of lithium-ion into carbon and/or reduced lithium ion diffusion in the electrolyte are favorable conditions [11], [40]. Dendrites are very fragile, can break off to dead lithium and lead to LLI [1]. The most catastrophic outcome caused by lithium dendrites is the short circuit due separator penetration [1], [18]. Following Figure 2.9 shows this unwanted rise of metallic lithium, where the dendrites pierce the separator and lead to a short circuit.

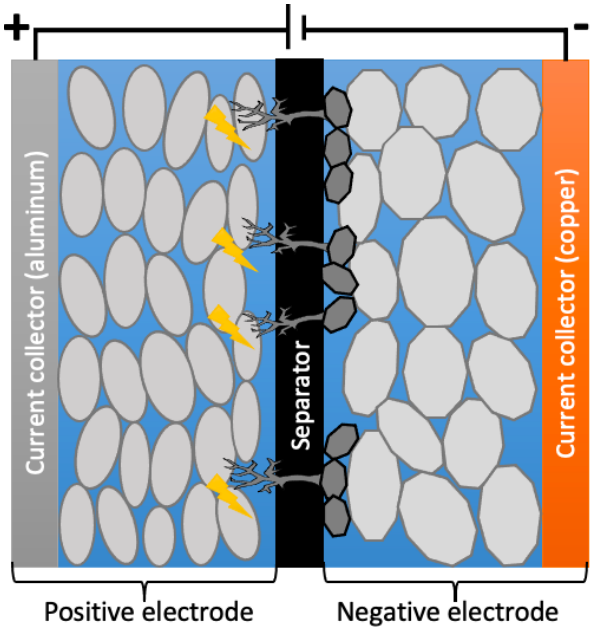

Figure 2.9: Structure of a lithium-ion cell with rising dendrites

Another safety relevant process are exothermic reactions caused by deposited or dead Li leading to heat generation [13]. To predict the occurrence of lithium plating in every form and prevent the catastrophic thermal runaway, detection methods become even more important. Following chapter should give a more detailed view about the different identification methods for the deposition of lithium.

2.5 Identification Methods

Multiple research has been conducted into detection and characterization methods for lithium plating to better understand this ageing phenomena and increase the safety during use of lithium-ion batteries. *Paul et al.* classified the techniques as shown in the following Figure 2.10.

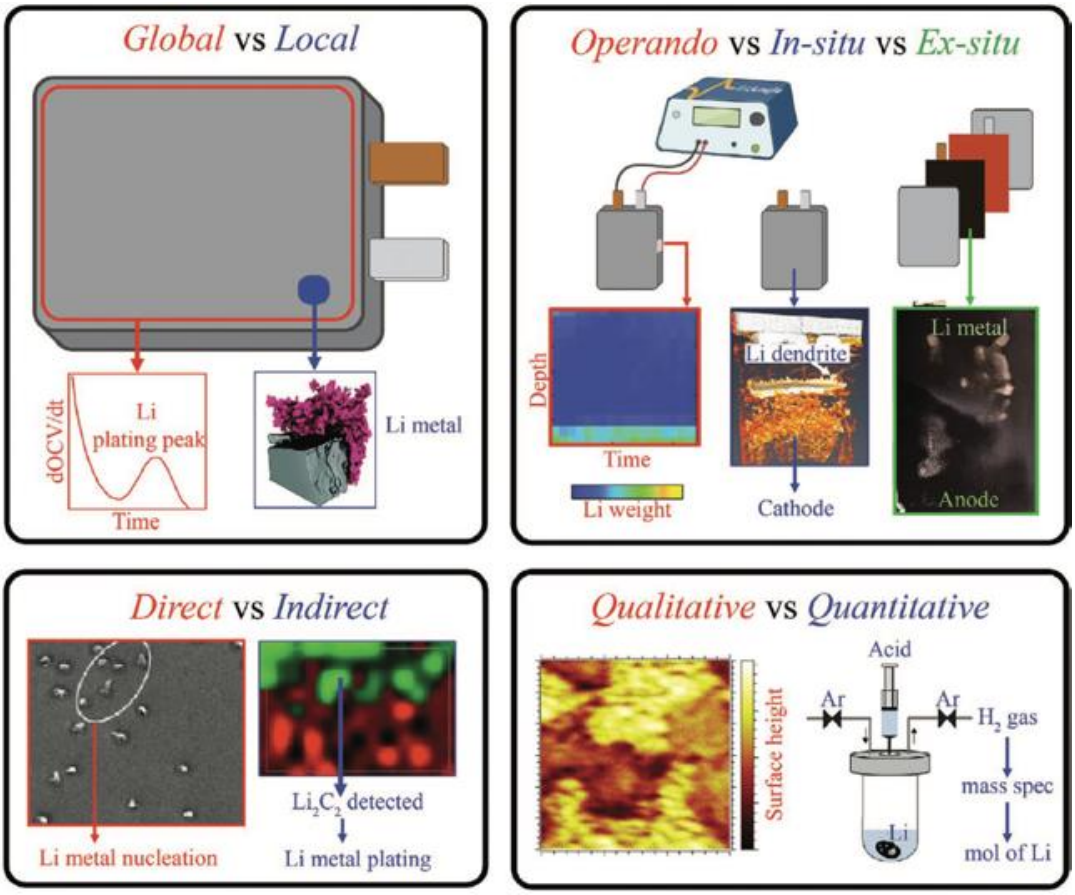

Figure 2.10: Classification of lithium plating identification methods [41]

The first classification in global or local detection technique is based on the length scale of detection relative to the length scale of the cell [41]. Global methods provide a summed value over the entire cell, while local methods deliver information on parts of the cell.

Second classification depends on the condition of the cell during detection or characterization, where it can be operando, in situ or ex situ [41]. In situ and operando methods are non-destructive and get information out of the fully assembled cell. The difference between those two techniques is the detection as a function of time. While in situ methods deal with cells in steady state, operando methods are done in real time and provide dynamic cell information.

On the other hand, ex situ methods typically take apart the cell and perform post mortem characterization.

Another split off follows due to direct detection of Li or indirect detection via changes in electrochemical, mechanical or chemical signature of the cell [41].

Finally, the information obtained by the technique defines the last division, where it can be a qualitative or quantitative method [41].

In literature there exist various identification methods which can be split up based on the described classification. A summary and classification of the different techniques which can be found in literature is shown in Table 2.1. Each of these methods has different requirements and gain different information about lithium plating. In this thesis, attention is paid to the electrochemical in situ or operando methods. Based on electrochemical signals, these techniques represent a feasible tool for online detection of Li plating [1]. They do not need special requirements and can be easily implemented in battery management systems (BMS) of LIBs. Most common electrochemical methods are voltage relaxation profiles, differential voltage analysis, incremental capacity analysis, anode potential measurements, and impedance spectroscopy [1].

Schindler et al. studied the voltage relaxation profile in combination with the impedance spectroscopy as non-destructive, operando methods. Small commercial lithium-ion cells with a rated capacity of 1.1 Ah are charged with 1C – 3C and discharged with C/40 – C/5 at sub-ambient temperatures down to -25 °C. Plateaus can be seen in the plotted voltage relaxation profile at the occurrence of lithium deposition in reference to a mixed potential. Due to their parameter variation, they formed limits of detectability for the mentioned methods. For example with too little applied charge, the mixed potential cannot be resolved in the relaxation profile. They also introduced the voltage differential during relaxation to trace the temporal progression and the potential level of the characteristic mixed potential evolving in the case of lithium plating. The usage of both differential methods has shown to be a suitable combination of understanding the underlying processes of lithium plating [42].

Differential voltage analysis (DVA or dV/dQ) during discharge as a nondestructive detection and quantification method for lithium plating in cylindrical 25540 cells with a capacity of 2.5 Ah was studied by *Petzl et al.*. Defined charge steps with C/2 to 1C in combination with sub ambient temperatures down to -26 °C and various charge throughputs are investigated. Analyzation of the peak in the differential voltage curve during discharge in combination with

capacity measurement was used to identify the complete mass of deposited lithium. For low to medium SOC values they found a linear SOC dependence of the plated lithium mass. With lower temperature the growing rate rises and the SOC starting point when lithium deposition occurs was shifted to lower values. They also found out more degradation with higher charge rate and they refer it to aggravated LP with increasing charge current [43].

Chen et al. applied incremental capacity analysis (ICA) while charging experimental three-electrode pouch cells with charging currents in the range of C/2 to 4C. They combined ICA with measurements of the anode potential and post-mortem SEM imaging to demonstrate a correlation of Li plating onset with a specific peak in the IC profile. Another analysis of an experimental multi-layer pouch cell showed a growing peak as charging rate increases and correlates with the graphite anode voltage minimum. The peak was sensitive to small amounts of lithium plating and evolves during extended fast-charge cycling due to the reduced lithium plating with a reduced lithium inventory [44]

In one of the newest studies, *Liu et al.* used nondestructive and destructive analysis to study battery aging over specific low-temperature cycles with followed high temperature cycles. Commercial 18650-type cylindrical cells with a capacity of 2.5 Ah and cycling rates of 0.5C – 1.5C were used in the study. The temperature range for the cycles is between -10 °C and 50 °C. During their study they used electrochemical impedance spectroscopy (EIS) and capacity tests. They divided the battery aging into dead lithium and SEI growth. Low temperature cycling increases the lithium plating content and dead lithium is prominent, which causes more capacity fading than SEI growth. High-temperature cycling after low-temperature cycling leads to consume of plated lithium. Therefore, electrolyte decomposition and SEI growth are the main aging mechanism [12].

Length scale	Type	Method	Reference
Global	Electrochemical	Voltage Relaxation Profile (VRP)	[1],[3],[23],[41],[42],[43],[45]
		Differential Voltage Analysis (DVA)	[1],[12],[41],[43],[46],[47], [48],[49],[50],[51]
		Incremental Capacity Analysis (ICA)	[1],[12],[44],[52],[53],[54]
		Coulombic Efficiency (CE)	[1],[3],[41]
		Impedance Spectroscopy (EIS, PEIS)	[1],[12],[41],[42],[44],[49], [52],[55]
		Anode Potential – Reference Electrode (RE)	[1],[3],[44],[51],[56],[57]
	Mechanical	Dilatometry	[41]
		Acoustic methods (TOF)	[41]
		Calorimetry	[41]
		Gravimetric	[41]
	Spectroscopic	Nuclear Magnetic Resonance (NMR)	[1],[3],[41]
		Electron Paramagnetic Resonance	[41]
	Chemical	Mass Spectrometry Titration (MST)	[41]
		Inductively Coupled Plasma Mass Spectrometry	[41]
		Titration Gas Chromatography (TGC)	[41]
Local	Qualitative Surface-Based	Scanning electron microscopy (SEM)	[1],[3],[12],[41],[44],[46],[47]
		Transmission electron microscopy (TEM)	[1],[3],[41]
		Atomic force microscopy (AFM)	[1],[41]
		Optical Imaging/ Microscopy	[1],[41],[44],[48],[56]
	Quantitative Imaging-Based	Neutron Depth Profiling (NDP)	[41]
		X-Ray tomography	[41]
		Neutron Tomography/ Radiography	[41]
		Nuclear Magnetic Resonance Imaging	[41]
	Diffraction Based	X-Ray diffraction (XRD)	[12],[41]
		Neutron diffraction	[3],[41]
	Spectroscopy Based	Time of Flight 2nd Ion Mass Spectrometry (TOF-SIMS)	[41]
		X-Ray Photoelectron Spectrometry (XPS)	[1],[12],[41]

Table 2.1: Detection and characterization methods for Li plating

2.5.1 Anode Potential – Reference Electrode

The most obvious and reliable sign for the detection of lithium deposition is the direct measurement of the anode potential at the graphite electrode. Due to special operating conditions, described in Chapter 2.3, the negative electrode gets polarized and the potential falls below 0 V vs. Li/Li^+, making LP thermodynamically possible [1], [3], [13]. The measurement of the anode potential in commercial cells is not possible, therefore a specific setup with an additional inserted third reference electrode (RE) is needed. With this RE the direct measurement of both potentials, anode and cathode, is possible [1], [13], [57], [58]. This experimental cell setup must be prepared under special laboratory conditions, inert atmosphere, to enable safe operations [3]. Additionally, material, location, and size of the reference electrode can affect the potential measurements [57], [58]. Due to the modified design, cell opening and RE insertion in the cell, a loss of stack pressure has to be considered as well.

It is an effective method to identify the effects of charging rate and temperature on anode potential [3]. *Rangarajan et al*. used a three-electrode pouch cell to quantify the amount of lithium plating. They defined parameters such as plating period, plating power, and plating energy to compare the effects of different charging protocols. The following Figure 2.11 shows an example of the anode potential vs Li/Li^+ on the vertical axis and the capacity on the horizontal axis during a charge cycle under LP favourable BCs.

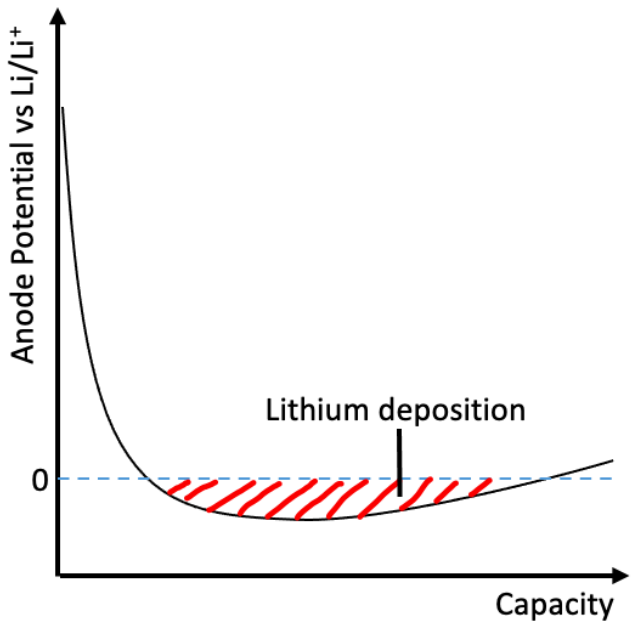

Figure 2.11: Exemplary diagram of anode potential vs. Li/Li^+ vs. capacity (replication of [56])

It can be seen that a part of the curve goes below 0 V vs. Li/Li$^+$, which is an indication for lithium plating on the anode active material surface [1], [13], [57], [58] [56]. The curve area below the 0 V line can be taken as an indication for the amount of plated lithium [56]. Therefore it is assumed that an increasing curve area below 0 V is connected to an increasing amount of lithium plating. Another approach is, to plot the anode potential vs Li/Li$^+$ in connection with the time on the horizontal axis. The longer the anode potential remains negative, the more lithium is plated [56].

2.5.2 Voltage Relaxation Profile

The Voltage Relaxation Profile (VRP) is an operando method to detect reversible LP in LIBs with graphite anodes. It is a non-destructive technique, does not require any special equipment and is therefore a suitable method for on-board detection of LP [1], [3], [23], [41], [42], [45], [51]. In this method the open-circuit voltage (OCV) is measured during relaxation time after a defined charge cycle [42]. Following Figure 2.12 illustrates the plot of the inverted OCV (black line) on the y-axis and the relaxation time after a charge cycle on the x-axis.

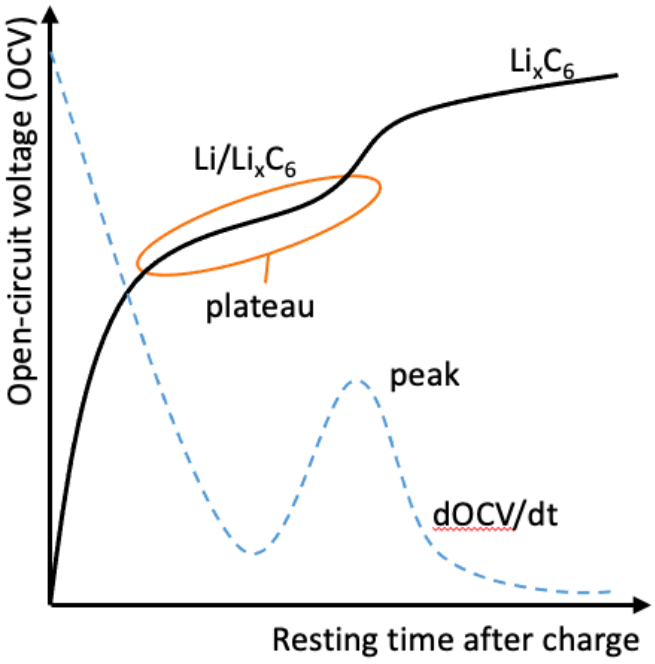

Figure 2.12: Exemplary voltage relaxation profile & corresponding dOCV/dt curve (replication of [51])

A plateau in the plotted voltage relaxation profile is a sign for LP during charging [23], [42], [51]. It arises during the relaxation phase through the chemical intercalation of deposited lithium in the graphite anode material. This means, the mixed potential when lithium is deposited Li/Li_xC_6 transitions to a pure potential Li_xC_6 [42], [51]. If no LP is happening, the

voltage relaxes to a stable value without a plateau. Smart et al. proposed that the length of the LP plateau is a sign for the amount of plated lithium. A further analyzation of these relaxation profiles was done by Schindler et al., who developed the technique using the time derivative of the OCV during relaxation. It can be seen as a variation of the differential voltage analysis, which is described in more detail in the next paragraph. In Figure 2.12 the blue dotted line shows the time derivative of OCV curve in black. Contrary to the plateau in the OCV curve, a peak occurs if lithium is deposited during charging and intercalated or stripped back in the graphite electrode during relaxation [42]. The time when this peak occurs during relaxation seemed to be related to the amount of Li that chemically inserts into graphite [42]. If no LP has occurred, or the amount of plated lithium is less than 1% of the graphite capacity [41, 42], the peak is not visible.

2.5.3 Differential Voltage Analysis during discharge

The differential voltage analysis during discharge (DVA or dV/dQ) is a global, non-destructive method for the detection of lithium plating [1], [3], [12], [41], [43], [46], [48], [49], [50]. It requires no additional cell components and offers a good detection in cells with LP in a significant amount of at least 1.5-5% of the graphite capacity [41]. In contrast to the VRP, which is used during the relaxation after charge, the voltage profile during the constant current (CC) phase of the discharge cycle is the basis of the DVA. A plateau in the discharge voltage occurs, when the mixed potential of lithium deposition on the anode surface transitions into a pure potential due to so called lithium “stripping” [3], [43].

With the use of the differential voltage dV/dQ, quantitative results can be obtained concerning the amount of stripped lithium [43]. The voltage is therefore differentiated by the capacity. If lithium plating happens during charging, the stripping process represents a peak in the dV/dQ plot [43]. The peak indicates the end of this stripping process during discharge [43], [45], [48]. Following Figure 2.13 shows an exemplary plot of a DVA curve during discharge CC phase, with dV/dQ on y-axis over the charge throughput during discharge on x-axis.

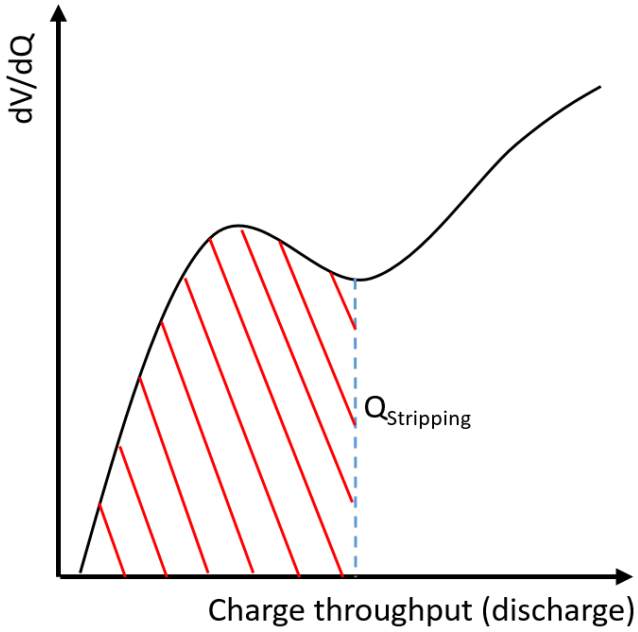

Figure 2.13: Exemplary differential voltage analysis peak during discharge (replication of [3])

During discharge, all reversible plated lithium is stripped which signals the peak in the DVA signal [43], [45]. The position of the peak is defined as the stripped charge amount $Q_{Stripping}$. Means, the capacity at the DVA peak is predominant a result of the stripped back lithium [43]. Width, amplitude and position of the peak can change with SOC range, C-rate and temperature [43], [46], [48], [49]. Cell degradation is another point which has to be taken into account with a shift of the peak [49].

2.5.4 Incremental Capacity Analysis

The incremental capacity analysis (ICA or dQ/dV) is the inverse of the differential voltage analysis described in the previous paragraph. It is a global non-destructive, in situ method and enables quantification of the degradation modes like LLI and LAM [1], [12], [41], [44], [49], [52], [54]. In combination with the low computational requirements, this is a suitable method for implementing in a battery management system (BMS). ICA is a chemistry depended method, means every LIB chemistry will have different response in form of an ICA curve [54]. The curve of this method is based on the derivative of the capacity with respect to the voltage [44]. Therefore, the area under the curve is the total capacity. During charging and discharging electrochemical reactions take place inside the cell at specific voltages. For each reaction a peak is observed in the ICA curve [12], [44], [53], [55]. Important information with reference to LIB aging and in narrower sense lithium plating, is the change of the peak positions in the curve. Changes can happen due to LLI and LAM, which can be divided in LAM_{PE} at the cathode

and LAM_{NE} at the anode [44], [52], [53], [55]. An exemplary charge cycle IC curve with the cell voltage on the x-axis and dQ/dV on the y-axis is shown in the following Figure 2.14.

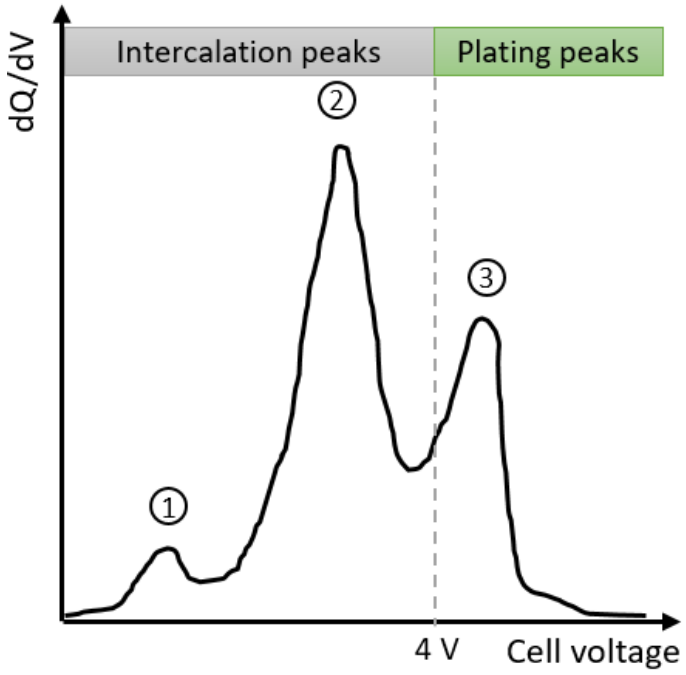

Figure 2.14: Exemplary ICA curve during charge cycle (replication of [12] & [44])

The peaks are numbered from left to right with 1, 2 and 3. Peak 1 and peak 2 are observed at voltages below 4 V and referred to intercalation peaks [44], [53]. With increasing C-rate these peaks can shift towards higher voltages because of the higher cell polarization [44]. Peak 1 belongs to the intercalation process in the negative electrode [54], [12] and peak 2 shows the NMC phase change between 3.6-3.8 V [12], [44]. The additional peak 3 above 4 V belongs to the phenomena of LP [44], because the anode potential drop below 0 V vs Li/Li^+ happens in higher cell voltage (difference between cathode and anode potential) regions. Changes in LLI and LAM can influence the peak positions and intensities [53]. For the specific case of LP the evaluation of Peak 3 is in focus of this thesis.

3 EXPERIMENTAL METHODS

High charging C-rates, low temperatures and high SOC are favoured conditions to induce lithium plating in LIBs [3], [11], [12], [13], [14]. Due to an advanced ageing of the cell, localized pressure or a poor cell design, this phenomenon can arise even under normal charging conditions [1], [13] [33]. In worst case scenarios the deposited lithium can form dendrites, pierce the separator and induce a short circuit [1], [18]. To avoid such safety-relevant situations and get more information about the cell condition, electrochemical methods are feasible tools for online detection of LP. In this part of the thesis the following four methods are applied on data created during cycling of commercial high energy cells:

- Voltage Relaxation Profile Analysis
- Differential Voltage Analysis
- Incremental Capacity Analysis
- Anode Potential Measurements

Following Figure 3.1 shows the procedure of this experimental section. It starts with a detailed look into the whole test setup, followed by the section of data generation during cell cycling. Based on the created cycling data, the last step deals with the electrochemical methods to identify lithium plating. The following sections describe all these parts in more detail.

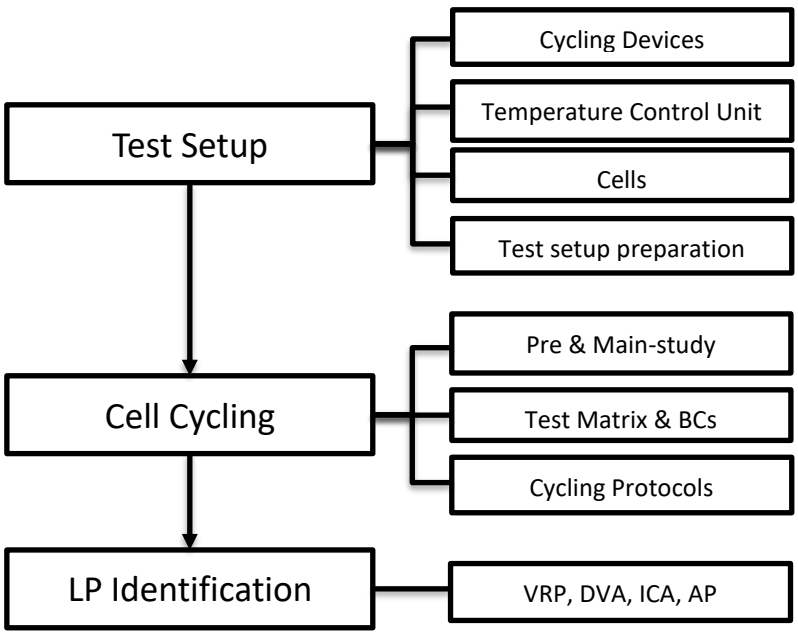

Figure 3.1: Procedure of Experimental Part

3.1 Test Setup & Prerequisite

Basis for charging and discharging of commercial high energy lithium-ion cells is a special test setup, which can ensure a safe execution. All of the test setup equipment is provided by the Battery Safety Centre Graz (BSCG) at the Technical University of Graz. The innovative test possibilities under laboratory conditions are used for assembling a test setup to assess the cells under favourable boundary conditions (BCs) for LP. Following Figure 3.2 shows the structure of the whole test setup in BSCG.

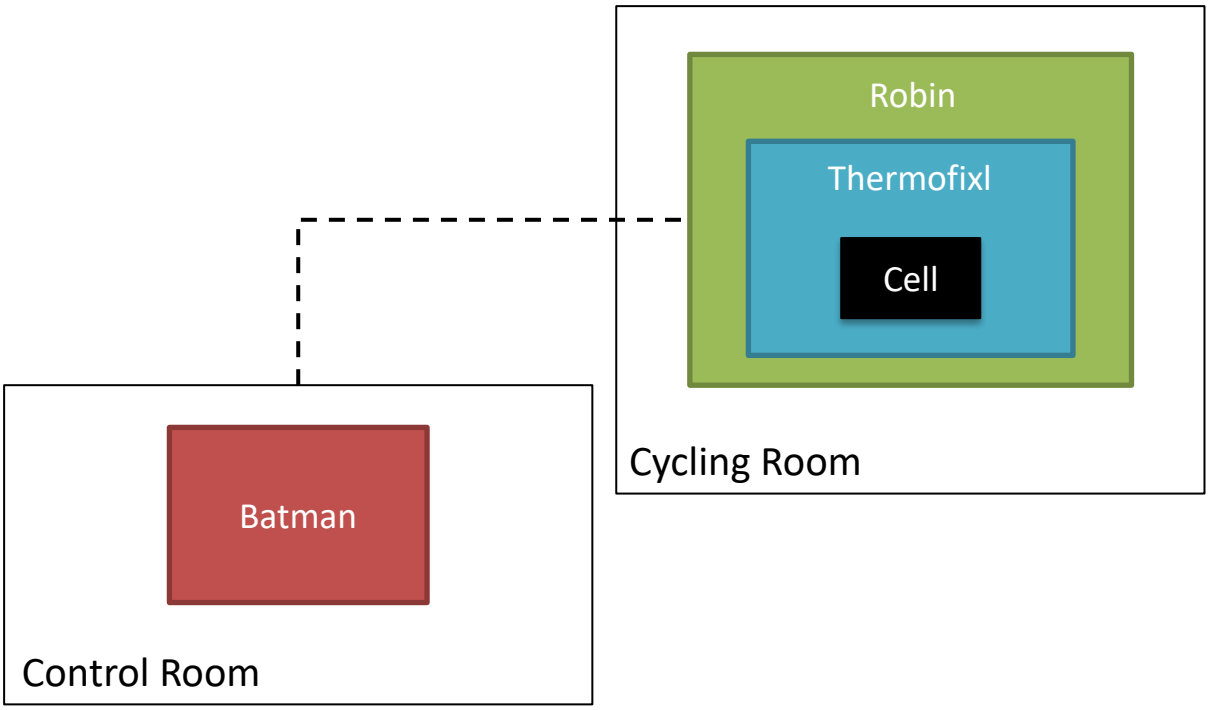

Figure 3.2: Structure of test setup in Battery Safety Centre Graz (BSCG)

Due to safety reasons the setup takes place in two separated rooms. The whole control of the test takes place in the control room. This room includes an electrical cycling unit (BATMAN) as well as the data acquisition system for recording the measurement data. With the help of shielded cables the control room is connected with the cycling room, where the cell cycling takes place.The cycling room includes the conditioning and clamping device (ROBIN), which enables the proper connection of different cell geometries, and a temperature control unit (Thermofixl) on cell level. All individual parts of the two rooms, their components and functions, are shown in more detail in the following sections.

3.1.1 Battery Testing, Monitoring and Cycling Unit - BATMAN

The electrical cycling of the cells as well as the data acquisition and recording of various measurement data is done by a battery testing, monitoring and cycling (aka. BATMAN) unit. This unit is designed by the institute and has a specially programmed cycling software. It enables the charging and discharging of batteries with a nominal power up to 10 kW for charging and 4.8 kW for discharging [59]. Both, charge and discharge, in a range of 0 to 80 V and 0 to 340 A [59]. To ensure a safe operation and control of the test cycles the BATMAN is placed in the control room and connected with the conditioning and clamping device (ROBIN) in the cycling room, as shown in Figure 3.2. Following Figure 3.3 shows a picture of the BATMAN unit with the operating computer plus software on the left side and the DAQ and the charging and discharging devices on the right side. More detailed information about the loading unloading devices can be found in the Appendix section A.2.

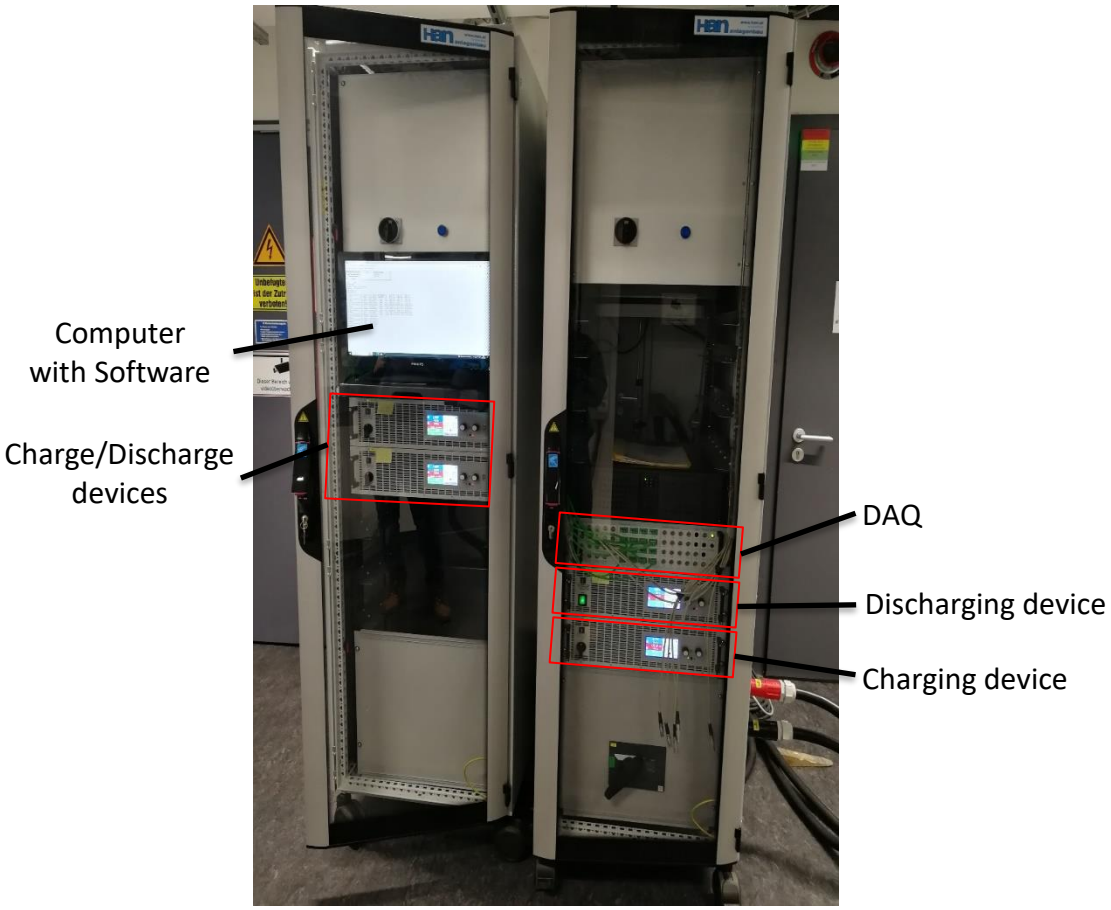

Figure 3.3: Battery Testing, Monitoring and Cycling unit (BATMAN)

3.1.2 Robust Battery Conditioning and Clamping Device - ROBIN

A robust battery conditioning and clamping device (aka. ROBIN), pictured in Figure 3.4, builds the basis for the cell cycling with different BCs in the cycling room. This device is connected with the BATMAN in the control room and with semi-automated clamping devices it enables the charge and discharge of varying battery geometries [59]. The ROBIN device has a special flooding tub, where the additional temperature control unit is placed during operation, to ensure a safe environment also during cell failure. A controlled pre-tension can be applied during charging and discharging processes. This is possible with a central mounted spindle in combination with a pressure plate and a mounted load cell. In our application the ROBIN device is only used for clamping the battery for charging and discharging.

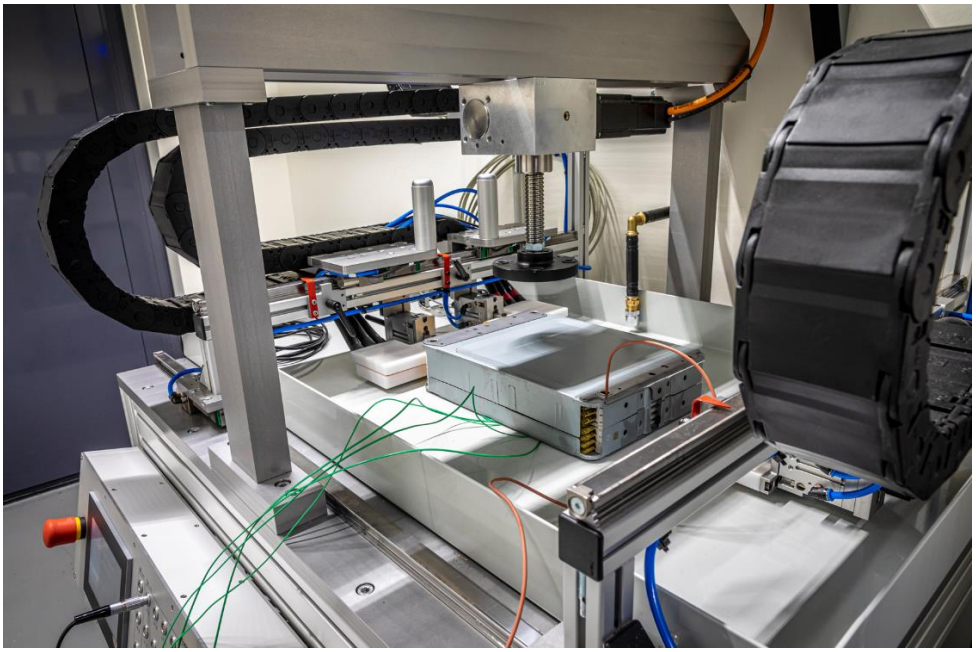

Figure 3.4: Robust Battery Conditioning and Clamping Device (ROBIN) [59]

3.1.3 Temperature control unit - Thermofixl

The last part of the basis setup is the temperature control unit, which is called “Thermofixl” and placed in the flooding tub of the ROBIN device. With this unit, it is possible to heat up and cool down the cell temperature during cycling between approximately 0 °C and 60 °C. The temperature control is based on a software, where you can define the desired cell temperature. A schematic view of the Thermofixl with the different parts is pictured in Figure 3.5. It consists out of an upper and lower plate with the cell placed in between. Each plate is built up on 5 temperature control modules with individual temperature control.

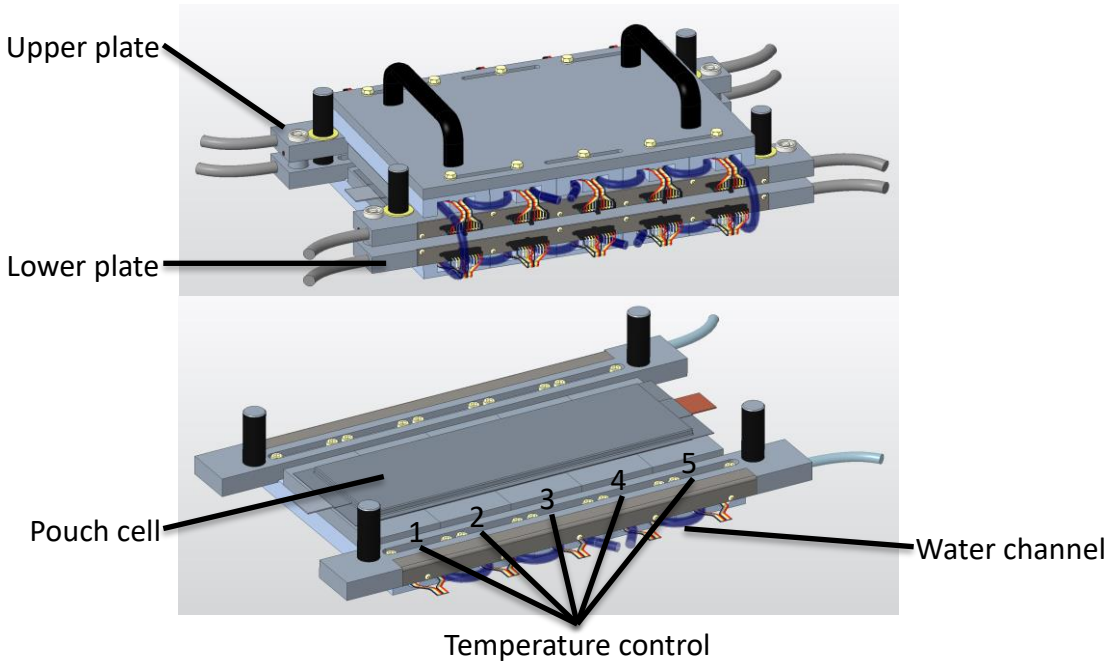

Figure 3.5: Schematic view of the Thermofixl with inserted pouch cell

To get a better understanding of the module function, following Figure 3.6 shows the schematic structure. Each temperature control module consists of an aluminium plate with two Peltier elements and two heatsinks glued on. Two PT1000 temperature sensors are measuring the plate temperature and two NTC temperature sensors monitor the temperature of the water cooled heatsinks. These modules enable a homogenous temperature control across the cell surface. More detailed information about the individual parts can be found in Appendix A.2.

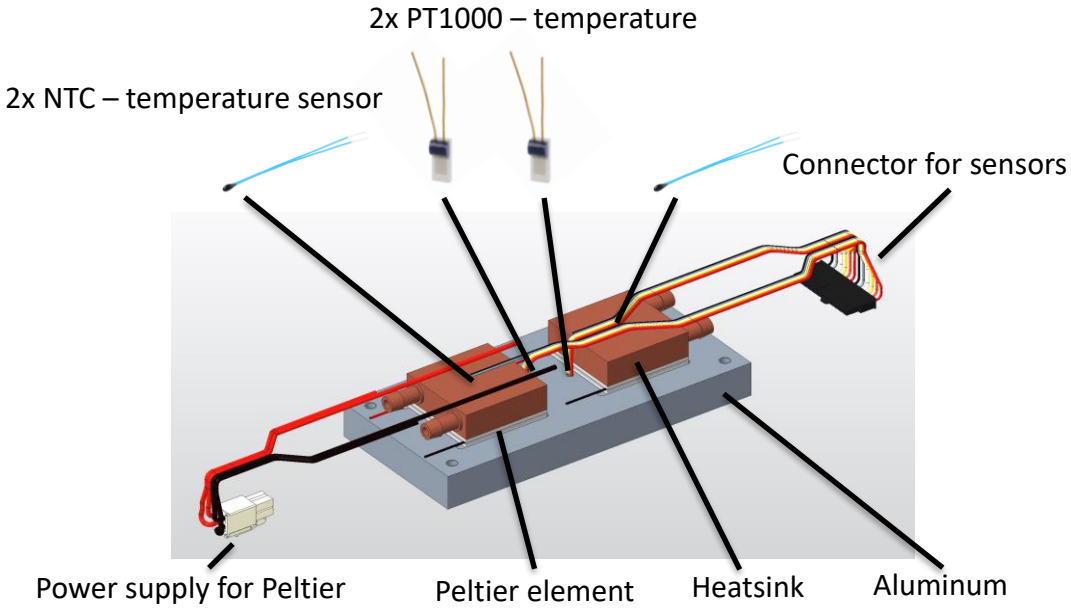

Figure 3.6: Temperature control module of Thermofixl

3.1.4 Cells

The cells used for all the experimental work are commercially available pouch cells with a nickel-manganese-cobald oxide (NMC712) cathode and a graphite/silicon anode. These high energy cells have a nominal capacity of 64.6 Ah [60]. Following Figure 3.7 shows a picture of the cell from the top, with the positive tab on the left side and the negative tab on the right side. This opposing cell tab position should reduce the height to suit an automotive underfloor. With a closer look it can be seen, that the tab position is off-center to be closer to the cooling plate on the ground. As an example for the commercial application, this pouch cell is used in the Audi e-tron GT quattro and the 2019 Porsche Taycan [60]. More information about the used cell is shown in Table 3.1.

Figure 3.7: Top front view of the lithium ion pouch cell

Manufacturer	LG Chemical Limited
Cell Model	E66A Lithium-Ion Polymer Battery
Cell type	Pouch
Chemistry	NMC712 / Graphite + SiO
Body dimensions	354 x 101 x 11.4 mm
Pouch dimensions (cooling area)	318 x 100 mm
Tabs dimensions	30 x 7-10 x 0.6 mm
Weight	896 g
Capacity	64.6 Ah
Nominal Voltage	3.665 V
Maximum Voltage	4.25 V
Minimum Voltage	2.8 V
Volumetric energy density (C/3; 25 °C)	648 Wh/L
Gravimetric energy density (C/3; 25 °C)	263 Wh/kg

Table 3.1: Cell specifications [60]

3.1.4.1 Reference Electrode Cells

To use the anode potential measurement as an identification method for LP, a specific cell preparation is necessary. For this, the previously shown commercial pouch cell, Figure 3.7, is adjusted with a third electrode. The so-called reference electrode (RE) enables the direct measurement of the anode and cathode potential during charging and discharging. Following Figure 3.8 shows the preparation procedure of the reference electrode cell in more detail. Step 1 involves the manufacturing of the RE. A drilled copper wire, coated with lithium, is wrapped in a separator and afterwards soaked in replica electrolyte. For the insertion of the RE nearby the negative electrode tab, in step 2 a special ceramic knife is used to cut a hole in the pouch material. Step 3 includes the insertion of the electrolyte soaked RE into the pouch, followed by the gluing process in step 4. This glue should seal the pouch, hold the RE in place and enable a safe operation.

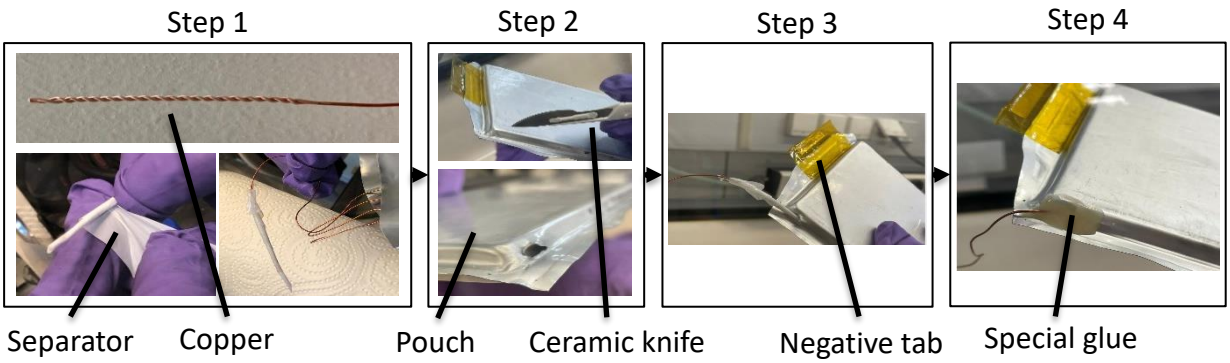

Figure 3.8: Preparation steps of the reference electrode cell

All of these preparation steps are done in a glove box with inert atmosphere, pictured in Figure 3.9. It has to be mentioned that the whole manufacturing process was done in cooperation with the Institute for Chemistry and Technology of Materials (ICTM).

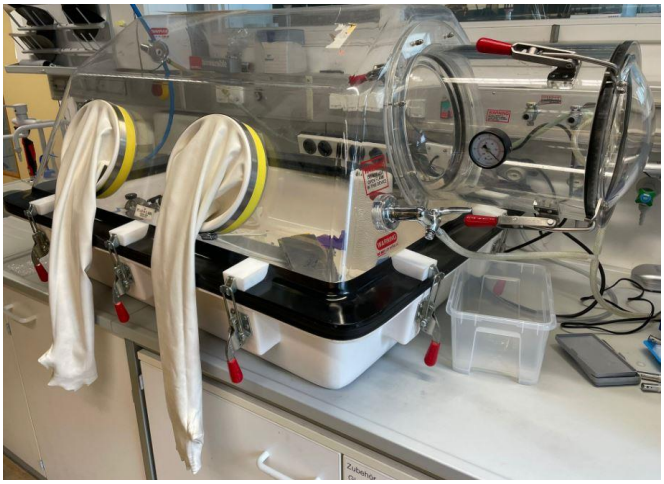

Figure 3.9: Glove box for reference electrode cell preparation at ICTM

3.1.5 Localized Pressure

It is already mentioned in the theoretical part, that a localized pressure on the cell surface can induce structural changes of the separator [38]. This can lead to closed pores, a high lithium concentration at these sites and lithium plating is more prominent in comparison to undeformed areas [1], [37], [38]. To realize a higher local pressure in addition to the global pressure on the cell surface, an impactor is used between the cell and the Thermofixl surface. The configuration of the test setup for a single cell with the additional impactor is shown in Figure 3.10.

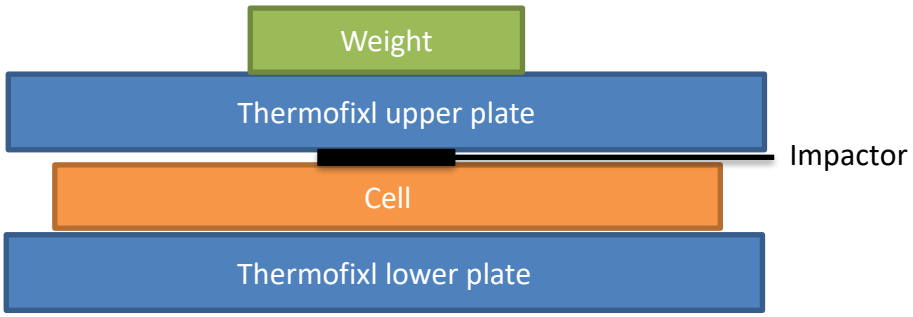

Figure 3.10: Setup of cell in Thermofixl with additional impactor

For the impactor a 50 mm diameter cathode sample with a thickness of 142 µm, shown in Figure 3.11, is used. With 70 kg weight on top of the Thermofixl, it enables approximately 50 % higher local pressure in addition to a global cell surface force of 300 N. The calculations are based on the cell data in Table 3.1.

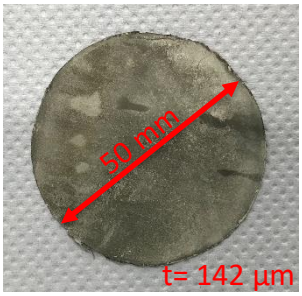

Figure 3.11: Cathode sample impactor with 50 mm diameter to induce a localized pressure

The analysis of the localized pressure is performed with a special data acquisition system (DAQ), available at BSCG. Therefore, a pressure mat is used between the impactor and the Thermofixl upper plate to identify the distribution over the cell surface. Figure 3.12 shows the stepwise procedure to measure the pressure distribution. It starts with placing the cathode sample impactor on top of the cell surface. In step 2 the pressure mat is placed above and the Thermofixl upper plate is put on top in step 3. To achieve the desired local and global force values, finally a mass of 70 kg is put on top of Thermofixl in form of lead granulate bags. The

analysis of the data provides a pressure map over the cell surface, where the local deformations due to the impactor can be seen in the centre (red circle) and additional high pressure areas on the cell edges (yellow circles). Reason for outer centre deformation is an unevenness of the cell surface due to cell disassembly, glue residues or other cell manufacturing defects. Compared to the higher localized pressure resulting from the impactor, the pressure increases are small and can be neglected. The pressure distribution measurement of two different cells with and without the impactor is illustrated in A.2.3.

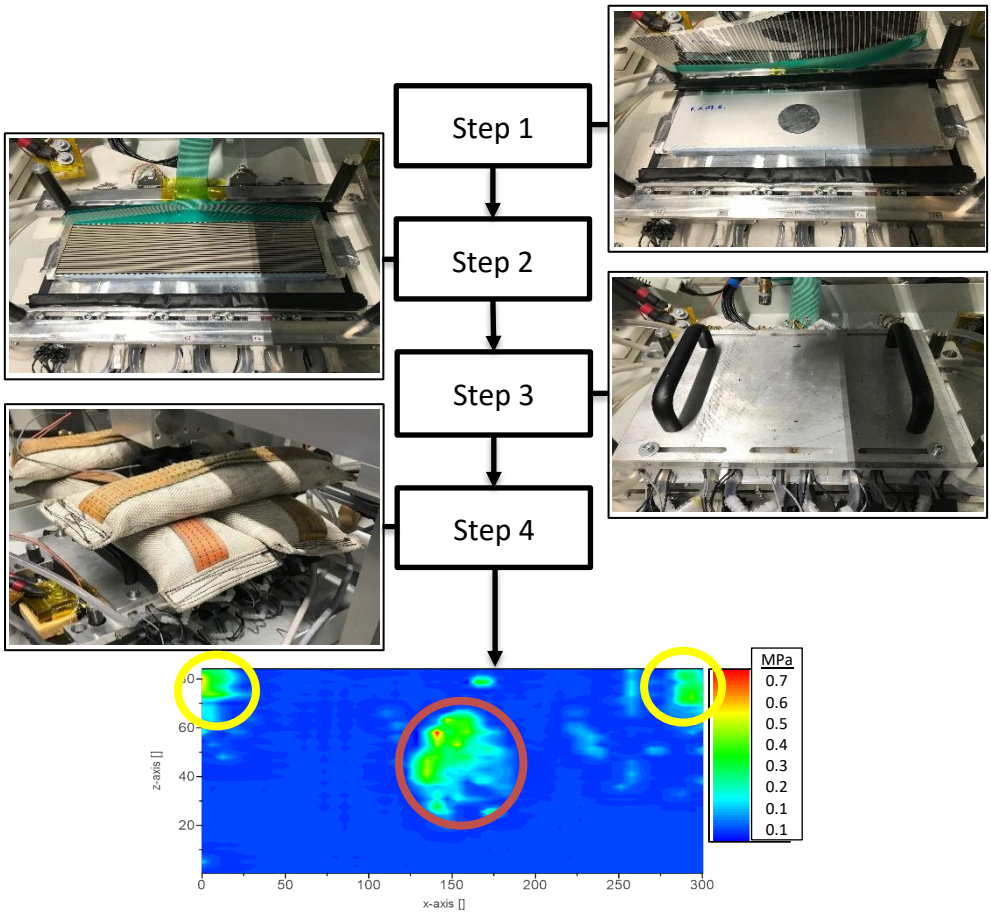

Figure 3.12: Procedure of pressure distribution measurement

3.1.6 Test setup preparation

Before the initial start of charging and discharging the cells, it is important to ensure always the same test conditions. The test setup procedure consists of 4 steps, shown in Figure 3.13 for 2 cells in parallel. To induce a localized pressure at the bottom cell, the first step includes the placement of the cathode impactor on the Thermofixl base plate. In addition, the isolation is wrapped around the 2 cell pack and the pack is placed on top of the impactor. Step 2 starts with the fixation of the voltage measurement cables on both cell tabs, followed by placing the

cathode impactor on top of the upper cell surface. After this, the special designed charging clamps are fixed on the cell tabs in step 3. In the last step 4, the Thermofixl upper half is put on top and the weight is placed with special caution for even distribution. For safety reasons all blank screws are isolated with tapes afterwards. After the test setup assembly, the temperature control unit started. When the target temperature is reached, the charging and discharging begins. This procedure is the same for all tests.

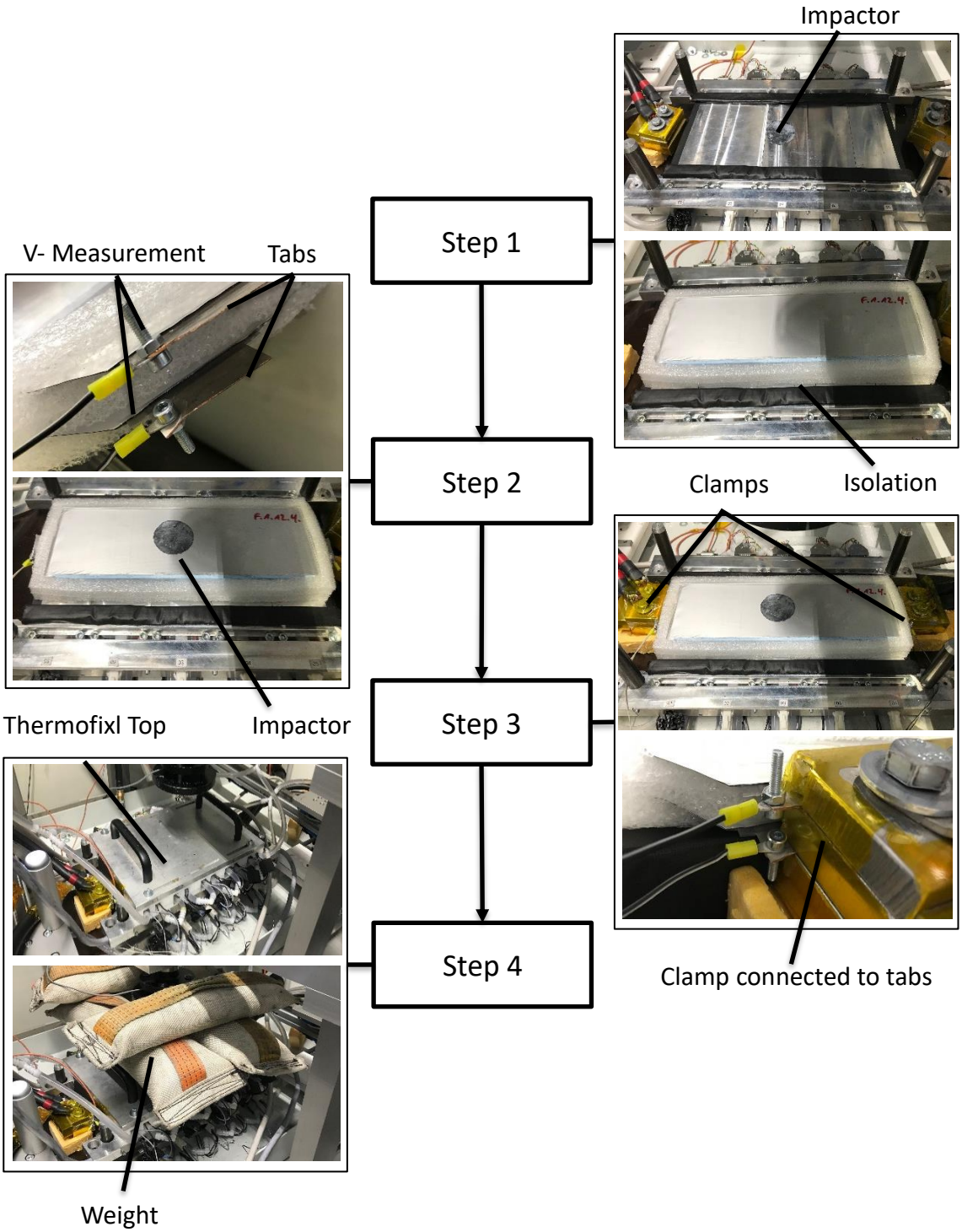

Figure 3.13: Stepwise procedure of the test setup preparation

3.2 Cell Cycling

Based on the theoretical section, specific favourable BCs are known for the ageing mechanism of LP in LIBs. This section gives a more detailed look into the cell cycling with the help of the before mentioned test setup to induce LP in commercial cells. The following subchapters include the breakdown of the cell cycling in two parts, the chosen BCs with creation of the test matrix and the different cycling procedures.

3.2.1 Pre- & Main-Study

The goal of the whole study is to induce LP in commercial high energy cells and identify its occurrence with different electrochemical methods. Therefore, the before shown test setup serves as a basis to cycle cells under special BCs. To get familiar with the test setup and see which BCs are achievable, the cell cycling is split up into a pre-study and main-study part. The pre-study deals with the limit identification of the setup and is divided into following 4 parts:

Pre-study 1: Reference electrode

- Proof of concept of the RE cell
- Investigation if the cell behaviour changes after the insertion of the RE
- Measurement of RE vs. anode voltage
- Voltage relaxation profile after RE insertion

Pre-study 2: Temperature and C-rate

- Investigation of the maximal possible C-rate
- Check the possibility of charging 2 cells in parallel with a safe use of the peak C-rate
- Investigation of the lowest possible stable temperature while charging and discharging
- Temperature evolution during cycling at different C-rates and temperatures

Pre-study 3: Localized Pressure

- Realization of a localized high pressure with respect to the cell surface
- Proof of concept that a localized pressure is achievable with the test setup

Pre-study 4:

- Voltage evolution of anode vs RE during charge/discharge and rest at lowest test temperature
- Influence of relaxation time on DVA (discharging cell with no relaxation time)

The outcome of the pre-study tests are known test setup limits and achievable BCs to induce LP in commercial high energy cells. To examine this part, a specific test matrix is created. Based on this matrix the commercial and RE cells are charged and discharged with different cycling protocols. Afterwards, in the main-study, cells are cycled over 20 cycles with the before found out BC to induce LP and reach a State of Health (SoH) of about 80 %. For SoH comparison the capacity before and after the cell cycling is used. Following subsection shows the test matrix with the different BCs in more detail.

3.2.2 Test matrix & Boundary Conditions

Basis of the pre-study cycling is a test matrix with different BCs to induce LP in high energy cells. The following Table 3.2 shows the test matrix, which is built up on theoretical favourable BCs for LP and limitations of the test setup. It includes 4 different C-rates in the range of 1C to 3C in combination with 3 different temperatures from 0 °C to 22 °C. Charging and discharging the cells based on these combinations allows the identifications of their individual influence on the onset of LP. Based on pre-defined rules, shown in the following sub chapter 3.2.2.1, this matrix is filled up after the pre-study cycling. Afterwards, clear BCs for the main-study cycling are known.

Boundary Conditions					
		C-rate			
Temperature		**1C**	**1.5C**	**2C**	**3C**
	22 °C				
	10 °C				
	0 °C				

Table 3.2: Test Matrix for pre- and main-study with C-Rates and temperatures

3.2.2.1 Test matrix interpretation

After cell charging and discharging based on the test matrix with defined cycling protocols (Chapter 3.2.3) the data is analysed with the electrochemical identification methods, described in Chapter 2.5:

- Voltage Relaxation Profile
- Differential Voltage Analysis
- Incremental Capacity Analysis
- Anode Potential Measurement

For each method the empty spaces of the test matrix are filled up with respect to the following rules:

- "No" & marked red – If no sign for LP is visible

No

- "Observed" & marked yellow – If a sign for LP is visible but only in a small extent

Observed

- "Prominent" & marked green – If a sign for LP is clearly visible

Prominent

An overlap of the filled up test matrices give the best possible boundary condition for the main-study cycling and enables a comparison of the four identification methods.

3.2.2.2 Cell combinations & termination criterion

As shown in the following Table 3.3, the test combinations of the test matrix are performed with different cells for varying C-rates. One cell is used for all 1C and 1.5C test combinations, another cell is used for the 2C tests and a third for all 3C tests. The whole test matrix is performed with the commercial cells and additionally the RE cells. Therefore, the same division for C-rates is done for 3 different RE cells.

Cell	Combination C-rate & Temperature		
1	1C & 1.5X with 22°C	1C & 1.5X with 10°C	1C & 1.5X with 0°C
2	2C with 22°C	2C with 10°C	2C with 0°C
3	3C with 22°C	3C with 10°C	3C with 0°C
4_RE	1C & 1.5X with 22°C	1C & 1.5X with 10°C	1C & 1.5X with 0°C
5_RE	2C with 22°C	2C with 10°C	2C with 0°C
6_RE	3C with 22°C	3C with 10°C	3C with 0°C

Table 3.3: Cells with different combinations based on the test matrix

To support the onset of LP with a high state of charge (high SOC), all cells are charged and discharged between 0 % and 90 % SOC. The 90 % limit is selected to prevent a cell overcharge. To achieve the specific SOC value, current and time are used as references. As shown in the previous chapter, the commercial cell has a capacity of 64.6 Ah. Charging the cell with 1C in the constant current (CC) phase, means the current is 64.6 A. A reduced charging current of 0.5C would be 32.3 Ah or an increased one of 1.5C would be 96.9 A. To calculate the charging time for a specific SOC value, in dependence of the current, following formula is used.

$$t = 360 \times \frac{C}{I} \times p \tag{5}$$

With:

- t = time [s]
- C = capacity [Ah]
- I = current [A]
- p = charging/discharging SOC amount in percentage $0 \leq p \leq 1$

The time which is used to charge and discharge each cell between 0 % and 90 % SOC with a different C-rate is listed in Table 3.4.

C-rate	Capacity [%]	Charge/ Discharge time [s]
1C	90	3240
1.5C	90	2160
2C	90	1620
3C	90	1080

Table 3.4: Charge and discharge times for different C-rates

Based on the test matrix the commercial and RE cells are cycled with special designed cycling protocols in the mentioned SOC range. In the following section the different cycle protocols for pre- and main-study are shown in more detail.

3.2.3 Cycles

Cell charging and discharging, based on the before shown test matrix, is done with special designed cycling protocols. For the pre- and main-study the cycling pattern is the same, but the amount of cycles differs. The cycling pattern is illustrated in Figure 3.14. The first cycle and the fifth cycle always include a relaxation period between the charge and discharge process, repeating every additional fifth cycle. For the cycles in between no relaxation period is added and discharging follows directly after charging. This pattern enables the usage of the voltage relaxation profile (VRP) as an identification method for LP in the cycles with additional relaxation period and differential voltage analysis (DVA) is used in the cycles in between. The incremental capacity analysis (ICA) and the measurement of the anode potential (AP) with RE cells is always possible.

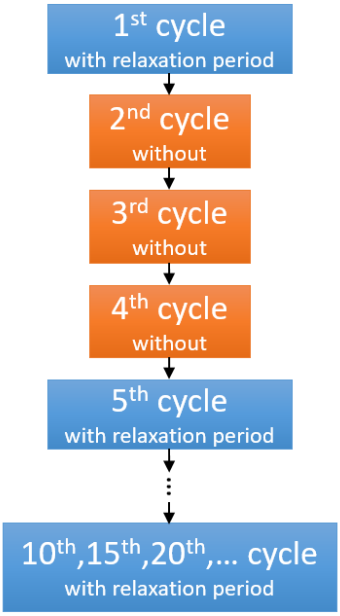

Figure 3.14: Pattern of the cell cycling for pre- and main-study

All of the cycles are based on a constant current-constant voltage (CC-CV) profile. It means, that the cell is charged at a constant current until an upper voltage limit is reached. After this, the voltage keeps constant and the current is decreased to a specific cut-off value. For the discharge it is similar, where the cell is discharged at a constant current until a lower cut-off voltage limit is reached. While keeping the voltage constant, the current is decreased gradually to the specific cut-off value. The voltage limits can be taken out of Table 3.1. For all tests a cut-off current limit of C/10 is used, where C represents the initial cell capacity. Following Figure 3.15 illustrates an example cycle without a relaxation period. The charging and discharging current in this example is 64.6 A.

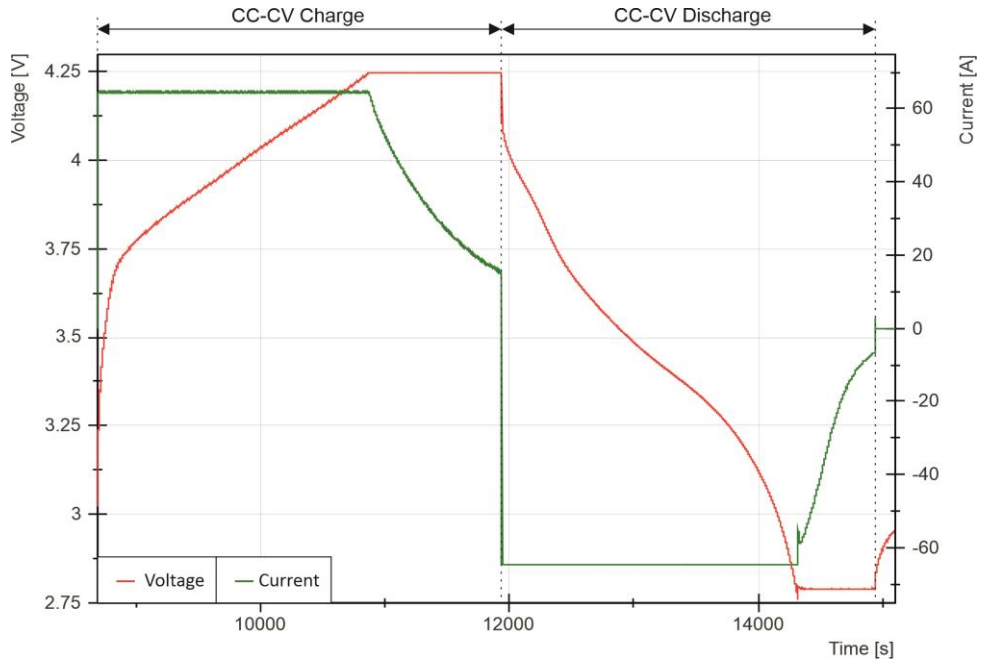

Figure 3.15: CC-CV charging-discharging cycle of the cell at 1C without relaxation time

An example cycle with additional relaxation time between the cycles is shown in Figure 3.16, where 64.6 A is used for charge and discharge current. This added time between the cycles enables the usage of the VRP in this cycle.

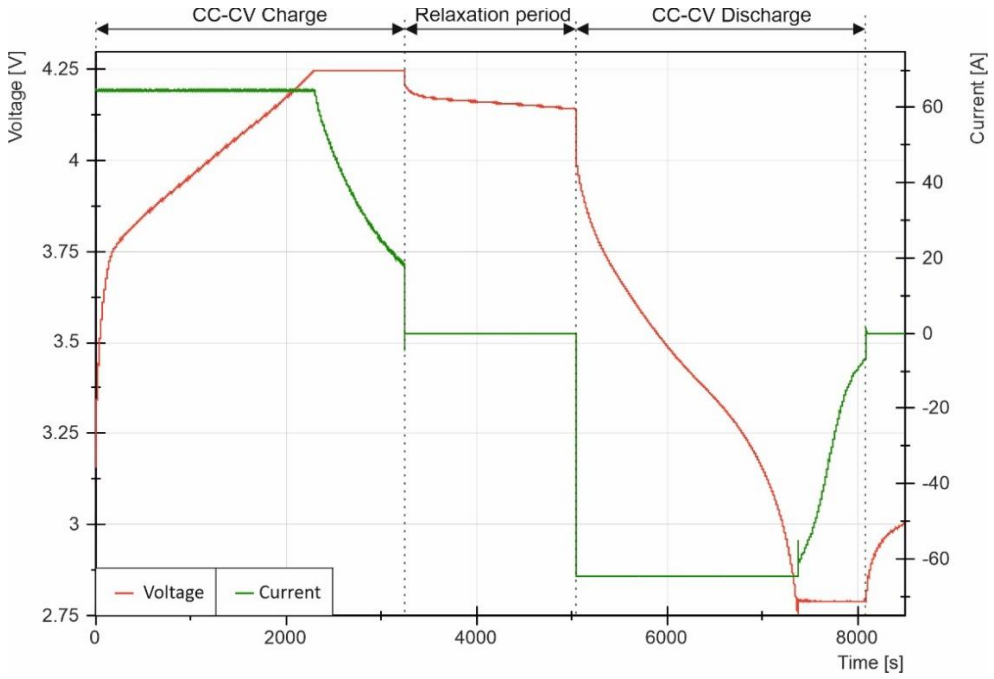

Figure 3.16: CC-CV charging-discharging cycle of the cell at 1C with additional relaxation time

The in Figure 3.15 and Figure 3.16 shown cycles are lined up based on the before shown cycling pattern and performed in different quantity during pre- and main-study cycling. Next sections show the different cycling protocols and adjustments for each study part in more detail.

3.2.3.1 Pre-study – commercial cells

The pre-study cycling of the commercial cells consists of 5 cycles in a row with the cycling pattern shown in Figure 3.14. Each cycle is based on a constant current-constant voltage (CC-CV) charging and discharging phase between 0 % and 90 % SOC. C/10 is used for the cut-off current, where the initial cell capacity deals as the reference. Between each cycle there is a waiting period of 15 minutes to relax the cell. Following Table 3.5 shows each step of the cycling protocol for the pre-study with commercial cells in more detail.

Steps	Action	
1	Charge to 90 % SOC	**Cycle 1**
2	Relaxation period of t= 5400 s	
3	Discharge to 0 % SOC	
4	Waiting period of t= 900 s = 15 min	
5	Charge to 90 % SOC	**Cycle 2**
6	Discharge to 0 % SOC	
7	Waiting period of t= 900 s = 15 min	
8	Charge to 90 % SOC	**Cycle 3**
9	Discharge to 0 % SOC	
10	Waiting period of t= 900 s = 15 min	
11	Charge to 90 % SOC	**Cycle 4**
12	Discharge to 0 % SOC	
13	Waiting period of t= 900 s = 15 min	
14	Charge to 90 % SOC	**Cycle 5**
15	Relaxation period of t= 5400 s	
16	Discharge to 0 % SOC	
17	Waiting period of t= 900 s = 15 min	

Table 3.5: Steps of cycling protocol - pre-study with commercial cells

A visualisation of the whole voltage profile is shown in Figure 3.17. It shows the cell voltage, green curve, on the y-axis plotted in respect to the time on the x-axis, where the relaxation period after the CC-CV charging phase in cycle 1 and cycle 5 is visible. To enable a comparison of each test, the same starting point must be ensured. Therefore, every cell is discharged to 0 % SOC with 1C and a cut-off current of C/10 before the initial cycling start.

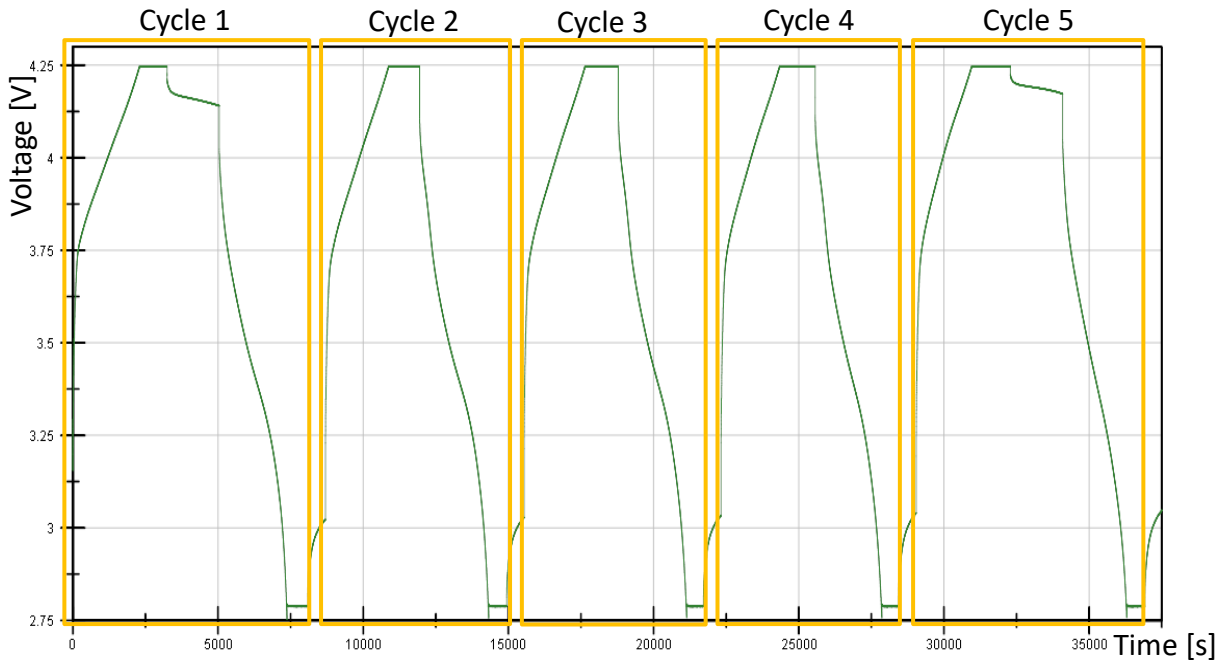

Figure 3.17: Voltage profile of pre-study cycling protocol for commercial cells

3.2.3.2 Pre-study – Reference Electrode Cells

The pre-study cycling of the RE cells consists of 2 cycles, based on the cycling pattern shown in Figure 3.14. Only 2 cycles are used to save testing time and examine the anode potential measurement, a first cycle with added relaxation period and a second one without. Table 3.6 shows the detailed steps of the cycling protocol. Both cycles are based on a constant current-constant voltage (CC-CV) charging and discharging phase between 0 % and 90 % SOC, where the first cycle includes the relaxation period. C/10 is taken as a cut-off current and between each cycle there is a waiting period of 15 minutes to relax the cell.

Steps	Action	
1	Charge to 90 % SOC	**Cycle 1**
2	Relaxation period of t= 5400 s	
3	Discharge to 0 % SOC	
4	Waiting period of t= 900 s = 15 min	
5	Charge to 90 % SOC	**Cycle 2**
6	Discharge to 0 % SOC	
7	Waiting period of t= 900 s = 15 min	

Table 3.6: Steps of cycling protocol - pre-study with reference electrode cells

Figure 3.18 illustrates the voltage profile of the two cycles with the RE cell. There, the cell voltage in blue is plotted on the y-axis in respect to the time on the x-axis.

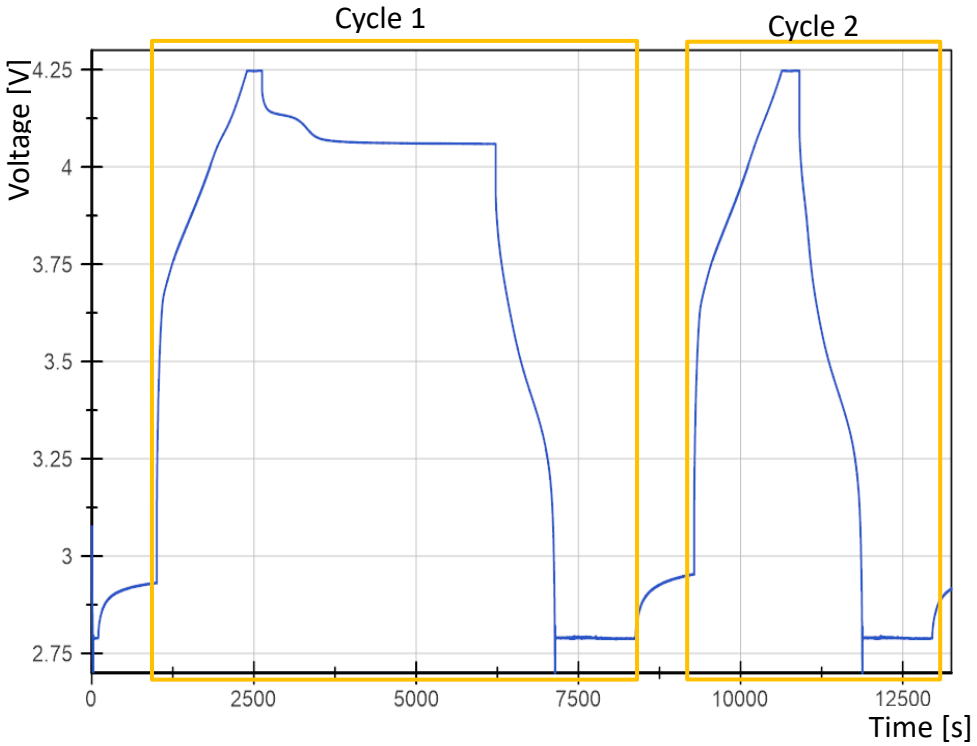

Figure 3.18: Voltage profile of pre-study cycling protocol for reference electrode cells

3.2.3.3 Main-study

The main-study cycling with commercial cells consists out of 20 cycles in a row, based on the in Figure 3.14 shown cycling pattern. Before and after the 20 cycles an additional electrical characterization (EC) cycle is added. Based on this EC cycles the SoH values are calculated and possible changes in the cell behaviour during cycling can be determined. Table 3.7 shows the detailed steps of the EC cycle. It is based on a CC-CV charging phase with a cut-off current of C/25, followed by a 2 hour relaxation period and a CC-CV discharge phase to the cut-off voltage of 2.8 V. 0.5C is used for C-rate. The cycling process is similar to the one shown in Figure 3.16, only the BCs are adjusted.

Steps	Action	C-rate 0.5C
1	Charge to 100 % SOC	**EC Cycle**
2	Relaxation period of t= 7200 s	
3	Discharge to 0 % SOC	
4	Waiting period of t= 900 s = 15 min	

Table 3.7: Steps of cycling protocol – Electrical characterization cycle

Between both EC cycles, the actual 20 cycles are performed with a C-rate of 1.5C and a temperature of 10 °C. These BCs are taken from the pre-study results to induce LP during the cycles and reduce the SoH of the cell to 80 %. Following Table 3.8 shows a compact form of the cycling protocol with the additional EC. The whole cycling protocol is shown in 7A.2.4. All of the performed cycles are based on a constant current-constant voltage (CC-CV) charging and discharging phase between 0% and 90% SOC. C/10 is used for the cut-off current and a 15 minute waiting period is used between each cycle.

Steps	**Action**	
1	Charge to 100 % SOC	**Electrical Characterization**
2	Relaxation period of t= 7200 s	
3	Discharge to 0 % SOC	
4	Waiting period of t= 900 s = 15 min	
5	Charge to 90 % SOC	**Cycle 1**
6	Relaxation period of t= 5400 s	
7	Discharge to 0 % SOC	
8	Waiting period of t= 900 s = 15 min	
9	Charge to 90 % SOC	**Cycle 2**
10	Discharge to 0 % SOC	
11	Waiting period of t= 900 s = 15 min	
12	Charge to 90 % SOC	**Cycle 3**
13	Discharge to 0 % SOC	
14	Waiting period of t= 900 s = 15 min	
15	Charge to 90 % SOC	**Cycle 4**
16	Discharge to 0 % SOC	
17	Waiting period of t= 900 s = 15 min	
18	Charge to 90 % SOC	**Cycle 5**
19	Relaxation period of t= 5400 s	
20	Discharge to 0 % SOC	
21	Waiting period of t= 900 s = 15 min	
22-24	Cycle without relaxation period	**Cycle 6**
25-27	Cycle without relaxation period	**Cycle 7**
28-30	Cycle without relaxation period	**Cycle 8**

31-33	Cycle without relaxation period	**Cycle 9**
34-37	Cycle with relaxation period	**Cycle 10**
38-40	Cycle without relaxation period	**Cycle 11**
41-43	Cycle without relaxation period	**Cycle 12**
44-46	Cycle without relaxation period	**Cycle 13**
47-49	Cycle without relaxation period	**Cycle 14**
50-53	Cycle with relaxation period	**Cycle 15**
54-56	Cycle without relaxation period	**Cycle 16**
57-59	Cycle without relaxation period	**Cycle 17**
60-62	Cycle without relaxation period	**Cycle 18**
63-65	Cycle without relaxation period	**Cycle 19**
66-69	Cycle with relaxation period	**Cycle 20**
70	Charge to 100 % SOC	**Electrical Characterization**
71	Relaxation period of t= 7200 s	
72	Discharge to 0 % SOC	
73	Waiting period of t= 900 s = 15 min	

Table 3.8: Steps of cycling protocol compressed- main-study

4 RESULTS

After the test setup preparation, the different cells are charged and discharged based on the cycling protocol, as described in Chapter 3.2.3. This chapter includes the results of the electrochemical identification methods for the pre-study cycling to identify the BCs for LP and gives a more detailed look into the outcome of the main-study cycling to reach a SoH of 80 %.

4.1 Voltage Relaxation Profile

First sub chapter deals with the analysis of the voltage relaxation profiles (continuous curve) and their time derivatives (dotted curve) from the pre-study cycling. Following Figure 4.1 shows the voltage relaxation profile (VRP) and time derivative curve for 0.5C and two different temperatures. The voltage on the left y1-axis and the time derivative on the right y2-axis is shown over the time on the x-axis in all following figures. This curve is part of the EC cycle, illustrated in Figure 4.16. A CFC60 filter in combination with a smoothening function is used for the curves. The continuous curve in turquoise represents the VRP for 0 °C and in black the VRP for 22 °C. Additional, the time derivative is represented by the dotted curve with the same color coding for both temperatures. The VRP curve for 22 °C relaxes to a voltage of ~4.22 V and for 0 °C to a lower value of ~4.16 V. Both VRP curves have a smooth curve and no plateau can be seen. For 22 °C the time derivative shows a smooth curve too and for 0 °C a slight slope change can be seen at ~0.3 h. These curves serve as a reference to the EC cycles, illustrated in Figure 4.16, where no LP occurred during the charging cycle.

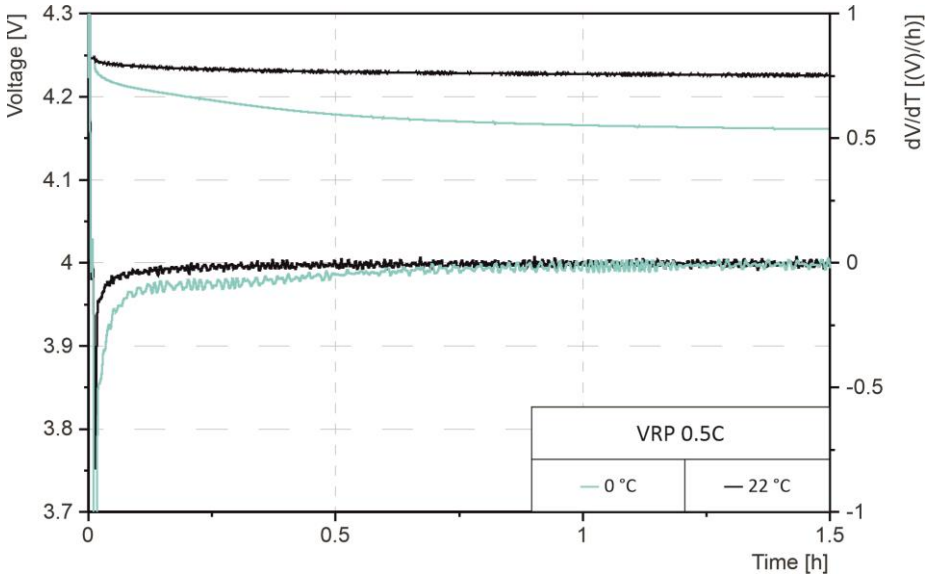

Figure 4.1: Voltage Relaxation Profile - Reference test 0.5C with 0 °C & 22 °C

Following Figure 4.2 shows the VRP and their time derivative for different C-rates at a temperature of 22 °C. Both curves for 1C, 1.5C, 2C and 3C are colored in red, green, blue, purple respectively. With a closer look on the 1C curves no plateau can be seen in the VRP and no peak in the time derivative. The voltage in the VRP relaxes to a value of ~4.07 V. For 1.5C, the voltage in the VRP relaxes to ~4.06 V and shows a slight slope change at ~0.08 h. In the time derivative curve a corresponding peak occurs at the same time. The minimum in the time derivative curve represents the steepest point in the VRP. After this point the voltage stabilizes. A clear plateau and peak are visible in the VRP and time derivative curve for 2C. The end of the plateau corresponds with the peak at ~0.2 h, afterwards the voltage in the VRP relaxes to a value of ~4.062 V. For 3C the VRP curve relaxes to a lower value of ~4 V. A clear plateau with an end at ~0.23 h can be seen and therefore a peak in the timer derivative curve. With increasing C-rate the time period of the plateau and the peak position shifts to higher values on the x-axis. In comparison with the VRP slope change for 1.5C, the 2C plateau occurs at a higher voltage, but the relaxed voltage is almost ident. The 3C shows a bigger drop of the plateau to lower voltages compared to the 2C plateau. It can be seen that the voltage drop after charging is increased with higher C-rate, which is related to the higher polarization of the cell [13].

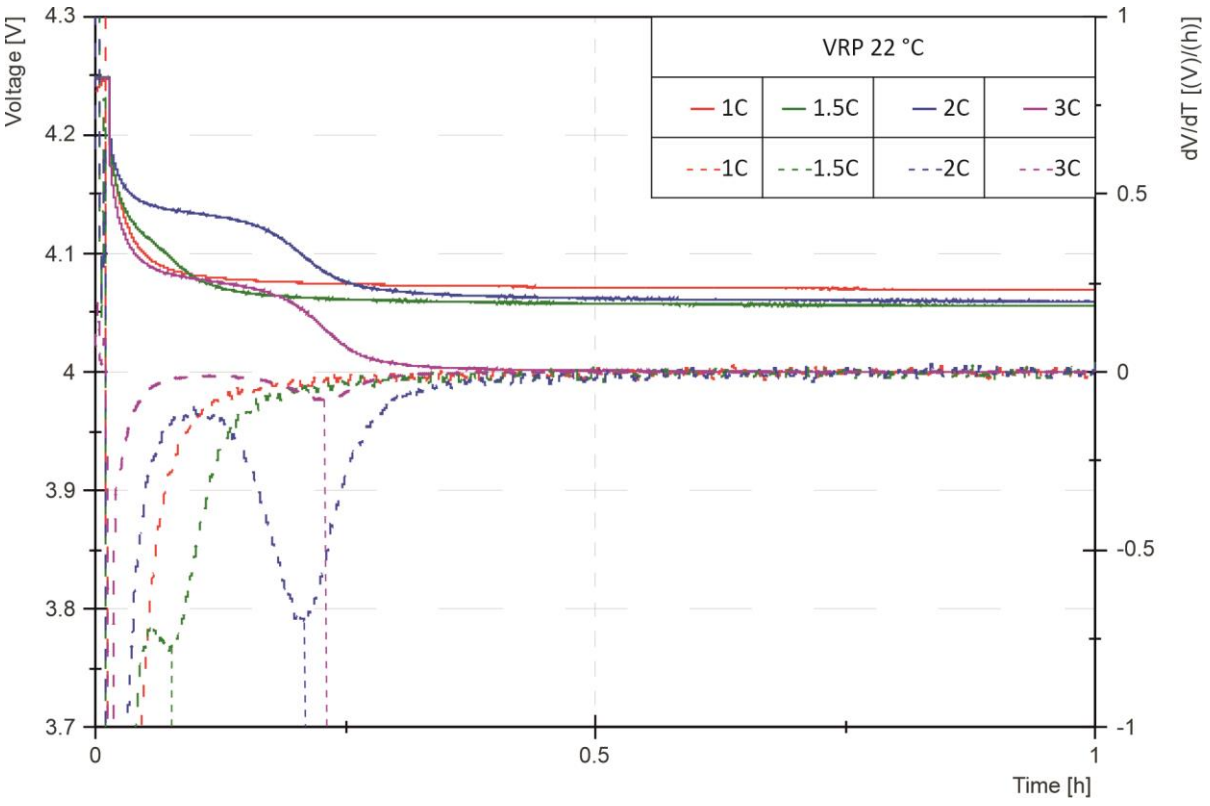

Figure 4.2: Voltage Relaxation Profile - 22 °C & all C-rates

Next Figure 4.3 represents the VRP and their time derivative curves for the four C-rates at a temperature of 10 °C. The curves for each C-rate have the same color coding as in Figure 4.2 before. For the temperature of 10 °C each VRP curve relaxes to a lower value in comparison with the 22 °C. This happens due to the higher cell polarization at lower temperatures. The 1C VRP curve relaxes to ~4.06 V, a slight slope change is visible at ~0.12 h and a corresponding peak occur at the same time in the derivative curve. A clear VRP plateau with a time period of ~0.24 h is visible for 1.5C, while a lithium stripping peak exists in the derivative curve at this point. For 2C the VRP plateau ends and the derivative peak occurs at a time of ~0.41 h. A clear plateau and peak are visible in both 3C curves at ~0.36 h. Compared to the 22 °C curves, the time period of the plateaus and peaks increased with the lower temperature of 10 °C. With a more detailed look on the 2C and 3C curves at this temperature, the lithium stripping period for the 3C is shorter compared to 2C. For the 22 °C curve in Figure 4.2 this decrease is not visible. For the lower temperature the cell polarization is higher and this shortens the CC-phase in the charge cycle for 3C in comparison with 2C [13]. The 1.5C and 2C VRP plateau occurs at higher voltages compared to the slope change in the 1C VRP curve. A plateau drop to lower voltages is visible or 3C. The amplitude of the peaks at lower temperatures is reduced, compared to the higher temperature peaks.

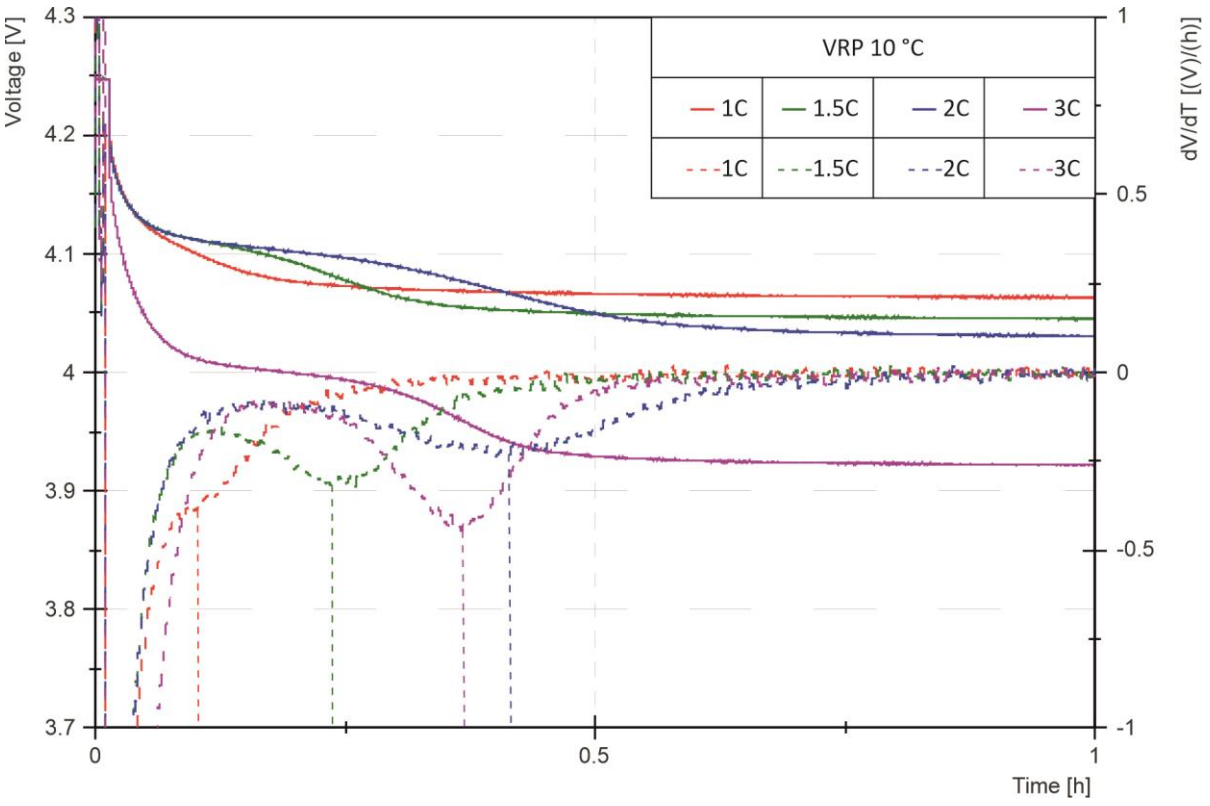

Figure 4.3: Voltage Relaxation Profile - 10 °C & all C-rates

The VRP and time derivative curves for the four different C-rates at a temperature of 0 °C are shown in following Figure 4.4. Same color coding as in the figures before is used for each C-rate, but the x-axis is increased to 1.5 h to illustrate the whole signals. The graph shows a slightly longer relaxation time to catch the whole signal. Compared with Figure 4.2 and Figure 4.3 for all C-rates the voltages in the VRP curves relax to lower values. At 0 °C the 1C VRP curve relaxes to ~4.05 V with a visible plateau in the VRP curve and a peak in the corresponding time derivative at ~0.31 h. For 1.5C the VRP curve relaxes to ~3.99 V. A plateau in the VRP at this C-rate is prominent and the peak in the derivative is visible at ~0.6 h. For 2C the plateau in the VRP and the peak in the dotted curve last until ~0.78 h and the voltage relaxes to a value of ~3.96 V. The 3C VRP curve relaxes to the lowest value of ~3.85 V. A clear plateau in the VRP and a peak in the time derivative curve is visible, positioned at ~0.56 h. With increasing C-rate the occurrence of the VRP plateaus is shifted to lower voltages. As already seen in Figure 4.3, the lithium stripping period for 3C is shorter compared to the one for 2C and this phenomenon is much more pronounced at 0 °C compared to 10 °C. The reason of the shortened CC phase during charging is already explained. At this temperature, clear plateaus and peaks can be observed in the corresponding curves for all C-rates.

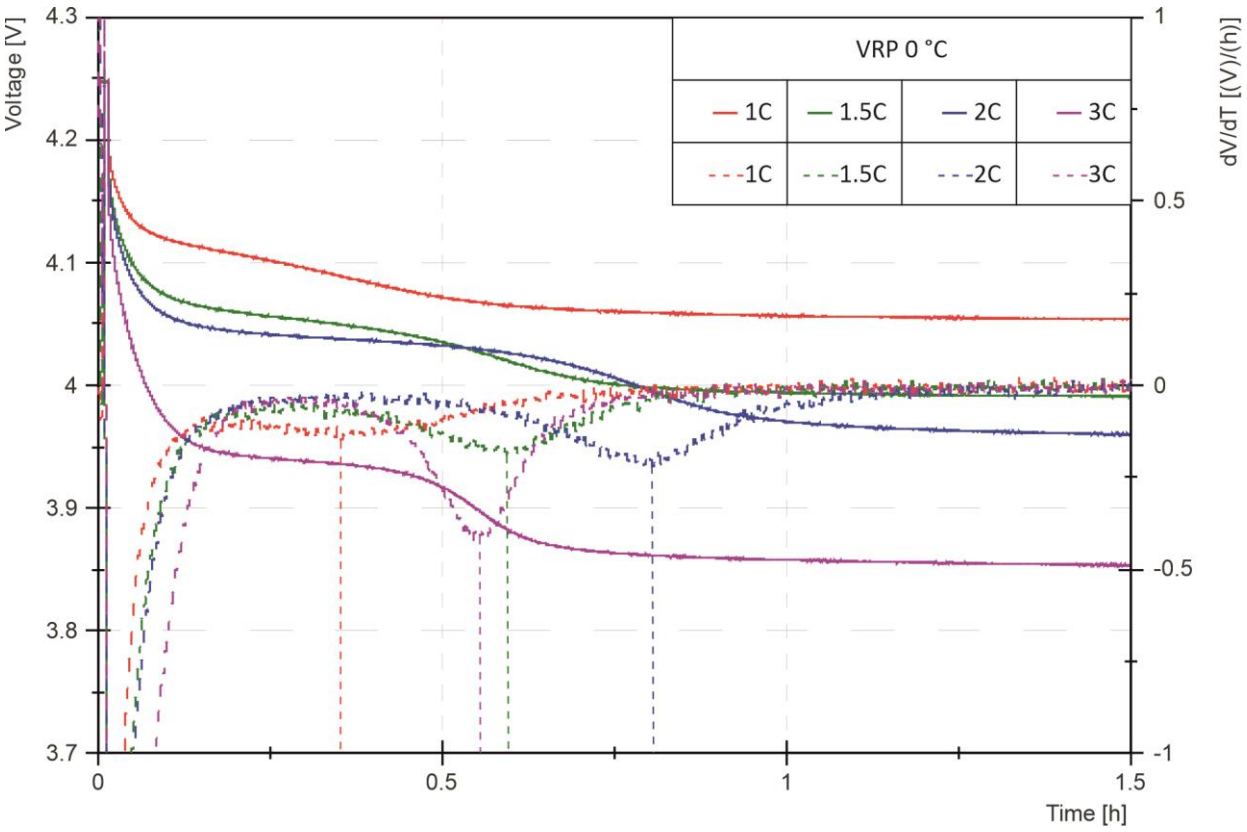

Figure 4.4: Voltage Relaxation Profile - 0 °C & all C-rates

All of the voltage relaxation profiles and their time derivatives show an increased lithium stripping period with lower temperatures. Until 2C an increased C-rate also shift the peaks on the x-axis to higher values, which corresponds to lithium stripping amount. For lower temperatures in combination with high C-rates a higher cell polarization has to be taken into account [13], which influence the charging cycles and the amount of stripped lithium during relaxation. Based on results out of the shown voltage relaxation curves with their corresponding time derivatives the test matrix is filled up for all the combinations of C-rates and temperatures, Table 4.2. For all green marked combinations, clear visible signs for the onset of lithium plating during the charging cycles are identified.

Boundary Conditions					
		C-rate			
Temperature		**1 C**	**1.5 C**	**2 C**	**3 C**
	22 °C	**No**	**Observed**	**Prominent**	**Prominent**
	10 °C	**Observed**	**Prominent**	**Prominent**	**Prominent**
	0 °C	**Prominent**	**Prominent**	**Prominent**	**Prominent**

Table 4.1: Test Matrix for pre-study with C-Rates and temperatures – Results Voltage Relaxation Profile

4.2 Differential Voltage Analysis

The results of the differential voltage analysis are shown in this second sub chapter. As explained already in the theoretical part, for this analysis the discharge cycle CC-phase is used. In all following figures the differential dV/dQ on the y-axis is plotted against the capacity on the x-axis after smoothening the curves with a smoothening function of ten points. Figure 4.5 shows the differential voltage analysis for 0.5C and two different temperatures, where the curve for 0 °C is colored turquoise and the curve for 22 °C black. The curve for 0 °C follows a smooth course with no extra peak. Compared to this, the 22 °C has a slight slope change between 10 Ah and 20 Ah, referred to de-lithiation phase change in graphite [43], [49], [47]. At higher capacities some additional peaks are visible between 50 Ah and 65 Ah. These peaks can be referred to the cathode side, intercalation into NMC and NMC phase change [43], [49], [47]. For the 0 °C curve no peaks are visible at a higher capacity. Both curves serve as a reference to the EC cycles, illustrated in Figure 4.16, where no lithium stripping peak is visible in lower capacity regions.

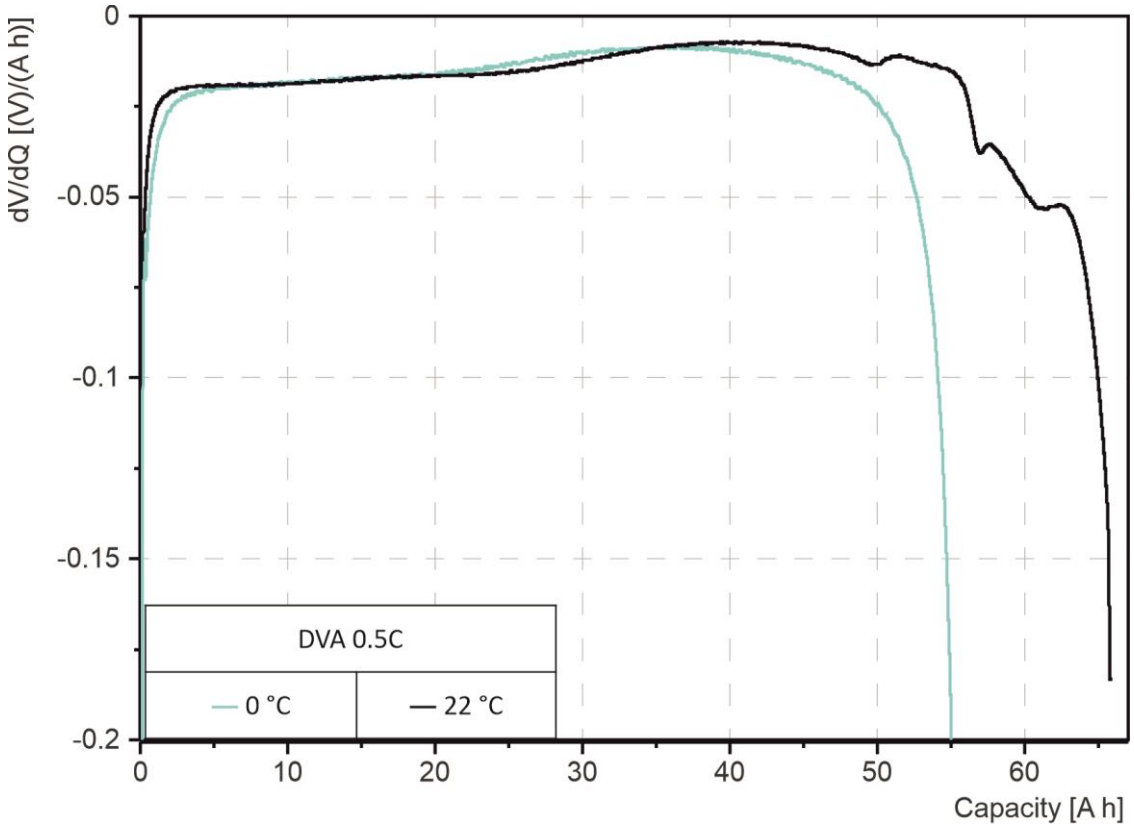

Figure 4.5: Differential Voltage Analysis - Reference test 0.5C with 0 °C & 22°C

The DVA curves for different C-rates at a temperature of 22 °C are shown in following Figure 4.6. 1C, 1.5C, 2C and 3C curves are colored in red, green, blue and purple. This color coding is the same in all further DVA graphs. The 1C DVA curve in red shows no slope changes in the capacity region below 15 Ah. Between 15 Ah and 20 Ah a slight change can be observed, which is related to the de-intercalation of the lithium-ions out of the graphite anode [49], [46]. In higher capacity regions between 40 Ah and 50 Ah also some changes are recognized, referred to the cathode NMC material [49], [43], [47]. In the 1.5C DVA a slope change occurs at a capacity of ~2.5 Ah and another small change is visible at ~15 Ah. At higher capacities the graph is smooth. For 2C a clear peak at ~4.9 Ah can be seen and a slight change in the curve between 10 Ah and 15 Ah. The highest C-rate 3C has a first peak positioned at ~7 Ah and some further small peaks at higher capacities. With increasing C-rate the peak in lower capacity regions gains in width on the x-axis, which is related to the amount of stripped back lithium [43], [49], [46], [48].

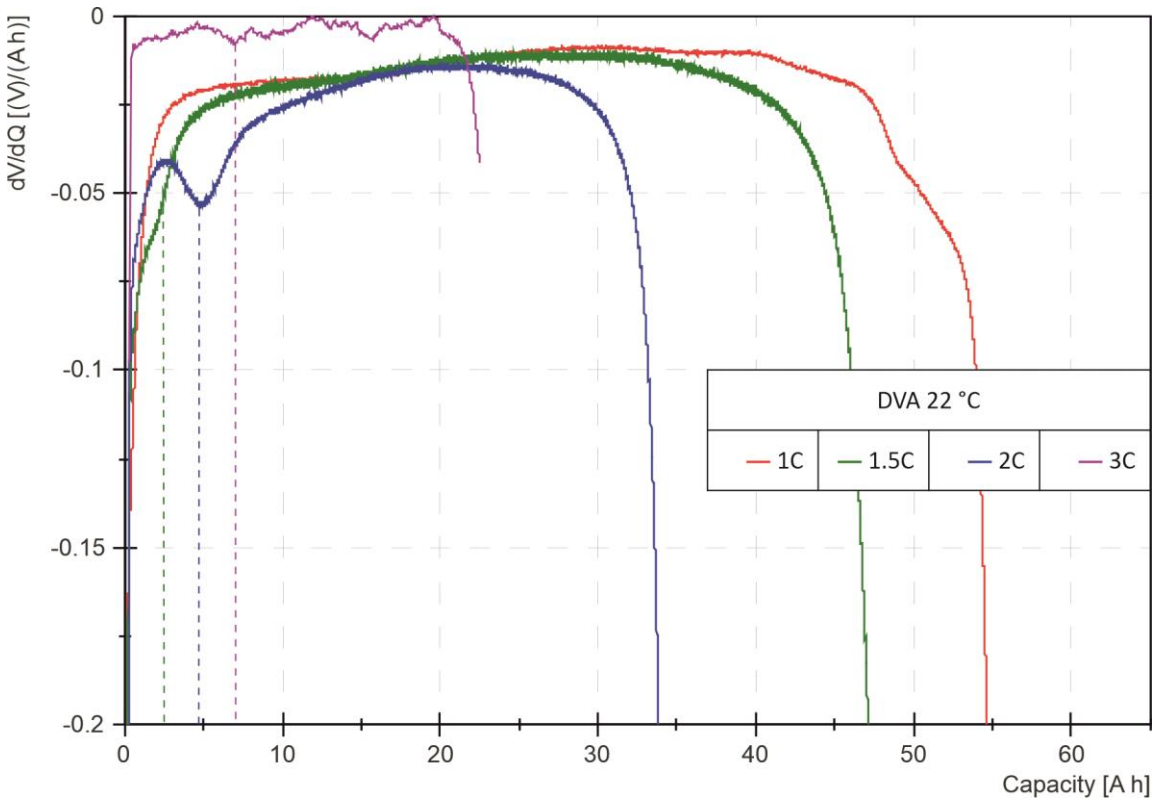

Figure 4.6: Differential Voltage Analysis - 22 °C & all C-rates

In following Figure 4.7 the DVA curves for different C-rates at a temperature of 10 °C are shown in more detail. The 1C DVA curve shows a slope change at a capacity of 2.5 Ah. Like for the higher temperature of 22 °C, the 10 °C curve for 1C shows a slight change between 15 Ah

and 20 Ah. In higher capacity regions above 20 Ah the curve is smooth. At this temperature the 1.5C DVA curve has a clear visible peak at ~4.5 Ah. The rest of the curve has no considerable changes in slope. For 2C a lithium stripping peak is observed at a capacity of ~9 Ah with a smooth rest curve. In comparison with Figure 4.6 the peak for 2C moved to higher capacity. The same shift towards right on x-axis is visible for the 3C DVA curve, where the peak occurs at a capacity of ~10 Ah. In this graph an approximation of the 2C and 3C lithium stripping peak can be seen. This shows again the effect of the reduced CC-phase during charging with higher C-rates at lower temperatures [43]. The cell polarization is higher, the CC-phase is shorter and less lithium arises at the anode surface and can be plated. The phenomenon of the cell polarization is also visible in the comparison of the different charging capacities on the x-axis. With increasing C-rate the charge capacity is reduced. In comparison with the higher temperature curves, illustrated in Figure 4.6, the charge capacity for each C-rate is reduced too for lower temperatures. For lower temperatures and higher C-rates an increase of the peak amplitude is visible, means LP is more prominent and the homogeneity of the lithium distribution in the cell is reduced [47].

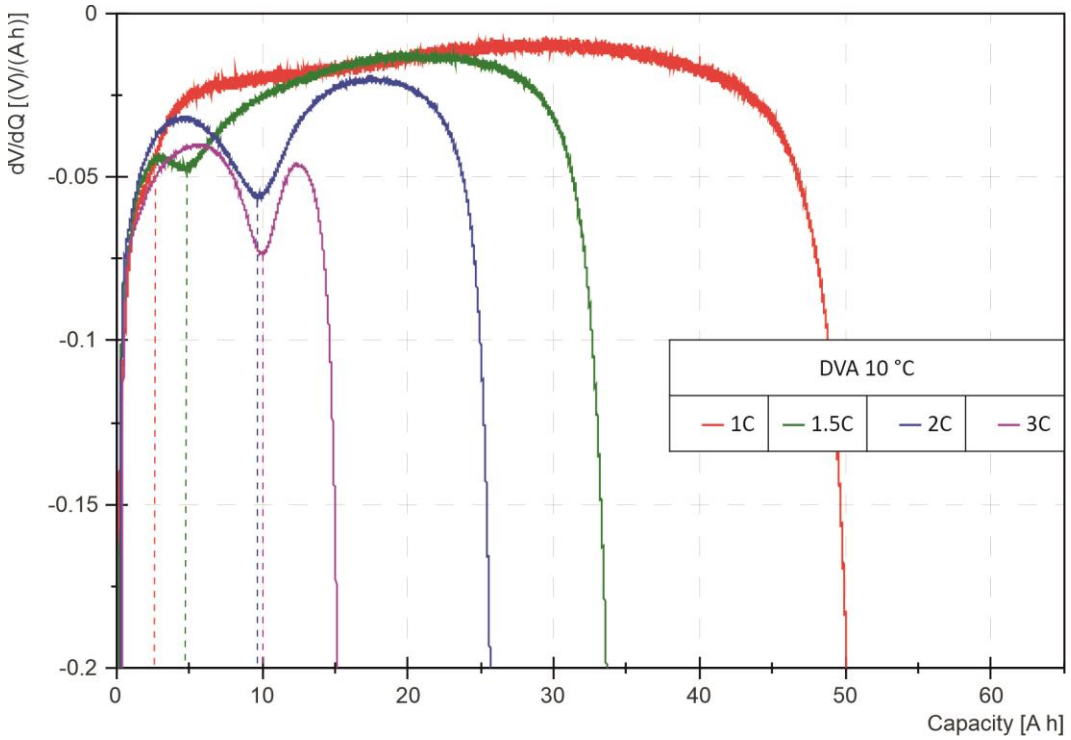

Figure 4.7: Differential Voltage Analysis - 10 °C & all C-rates

The DVA curve for the four different C-rates at the lowest temperature of 0 °C are shown in Figure 4.8. At this temperature a lithium stripping peak is visible for the 1C DVA curve at a

capacity of ~5 Ah. The 1.5C DVA curve in green has a peak at ~8.5 Ah and a smooth curve above this capacity. Compared to the DVA curves at higher temperatures, the peak moved towards higher capacity. This shift to the right on the x-axis is also visible for the 2C lithium stripping peak, which is prominent at ~12 Ah. For the 3C DVA curve a peak occurs at a capacity of ~10.5 Ah. This C-rate shows only a small peak shift on the capacity axis compared to the other cycling rates. With a closer look it can be seen that the peak for 3C is prominent at a lower capacity compared to 2C. This is again related to the high cell polarization at the low temperature charging cycle [43]. Compared to the DVA cycles at higher temperatures, the charging capacities for each C-rate are reduced due to the higher cell polarization. For 0 °C all peaks show the highest amplitude, which means more LP happened during the charge cycle and the lithium distribution in the cell is inhomogeneous [47].

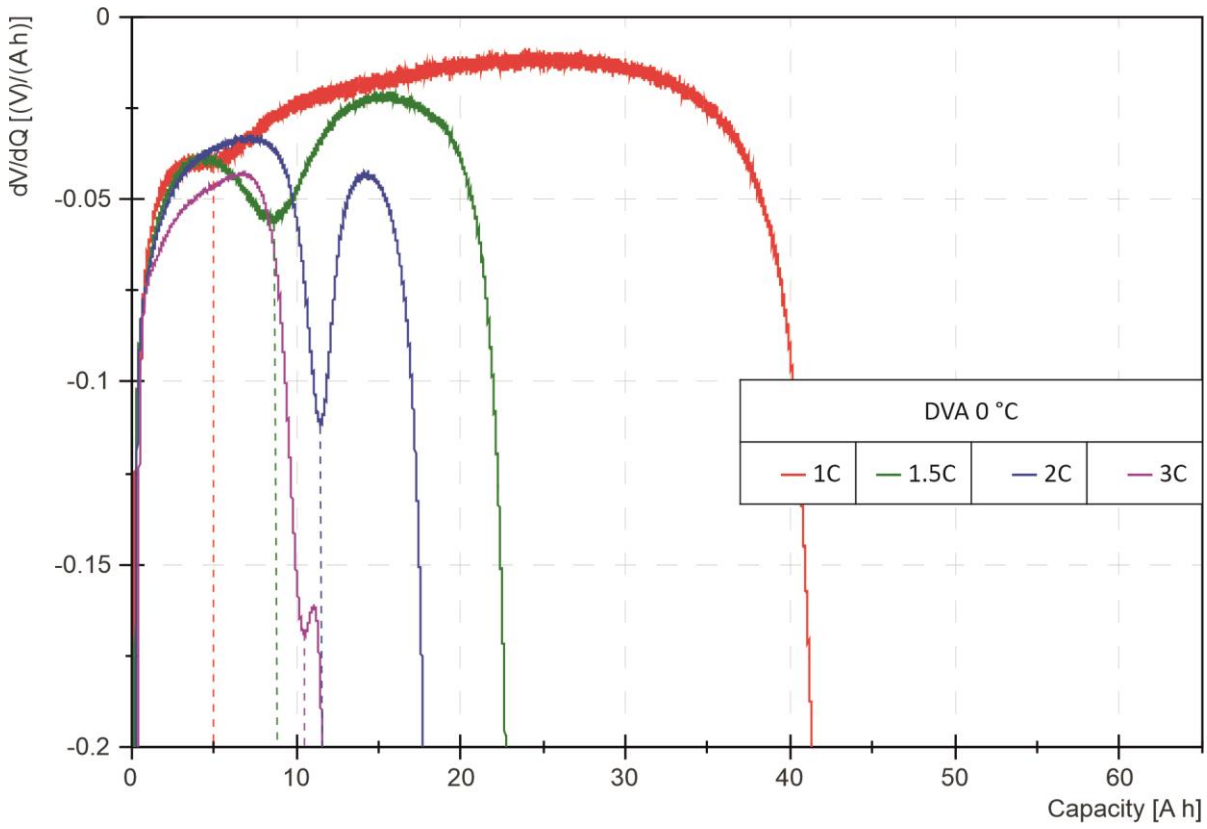

Figure 4.8: Differential Voltage Analysis - 0 °C & all C-rates

The differential voltage curves show the appearance of a lithium stripping peak with lower temperatures and higher C-rates. With lower temperatures the peak occurs also for lower C-rates like 1C and 1.5C. Until a specific value, an increased C-rates shifts the peaks to higher capacities at the same temperature and define a higher lithium stripping amount. For higher

C-rates and lower temperatures an increase of the peak height is visible and lower temperatures reduce the charging capacity due to high cell polarization. Based on the results of the differential voltage curves the test matrix is filled up for all the combination of C-rates and temperatures, Table 4.2. For all green marked combinations, clear visible signs for the onset of lithium plating during the charging cycles are identified.

Boundary Conditions					
		C-rate			
Temperature		1 C	1.5 C	2 C	3 C
	22 °C	No	Observed	Prominent	Observed
	10 °C	Observed	Prominent	Prominent	Prominent
	0 °C	Prominent	Prominent	Prominent	Prominent

Table 4.2: Test Matrix for pre-study with C-Rates and temperatures – Results Differential Voltage Analysis

4.3 Incremental Capacity Analysis

The following sub chapter deals with the results of the incremental capacity analysis (ICA), where the charge cycle CC-phase is used for analysis. In all following figures, the differential dQ/dV on the y-axis is plotted against the voltage on the x-axis. Before calculating the differential the data is filtered with a CFC60 filter. After the calculation a smoothening function with 30 points is performed on the data. Figure 4.9 shows the incremental capacity analysis for a charge rate of 0.5C and two different temperatures. The 0 °C curve is colored turquoise and the 22 °C is colored black. For the 22 °C ICA curve four signal changes are visible. A first peak 1 at ~3.52 V and a slope change 1* at ~3.55 V are observed at a lower voltage level, which are related to the lithium intercalation process into the graphite anode [12], [54]. Peak 2 at ~3.67 V and a slope change 2* at ~3.77 V represent the NMC phase change and solid solution in the active material on the cathode side [12], [44]. The 0 °C ICA curve shows a first lithium intercalation peak 1 at ~3.65 V. At ~3.77 V a second peak 2 and at ~3.8V a slope change 2* represent the NMC reactions [12], [44]. Both curves serve as a reference to the EC cycles, illustrated in Figure 4.16, where no LP peak is visible in higher voltage regions above ~4 V.

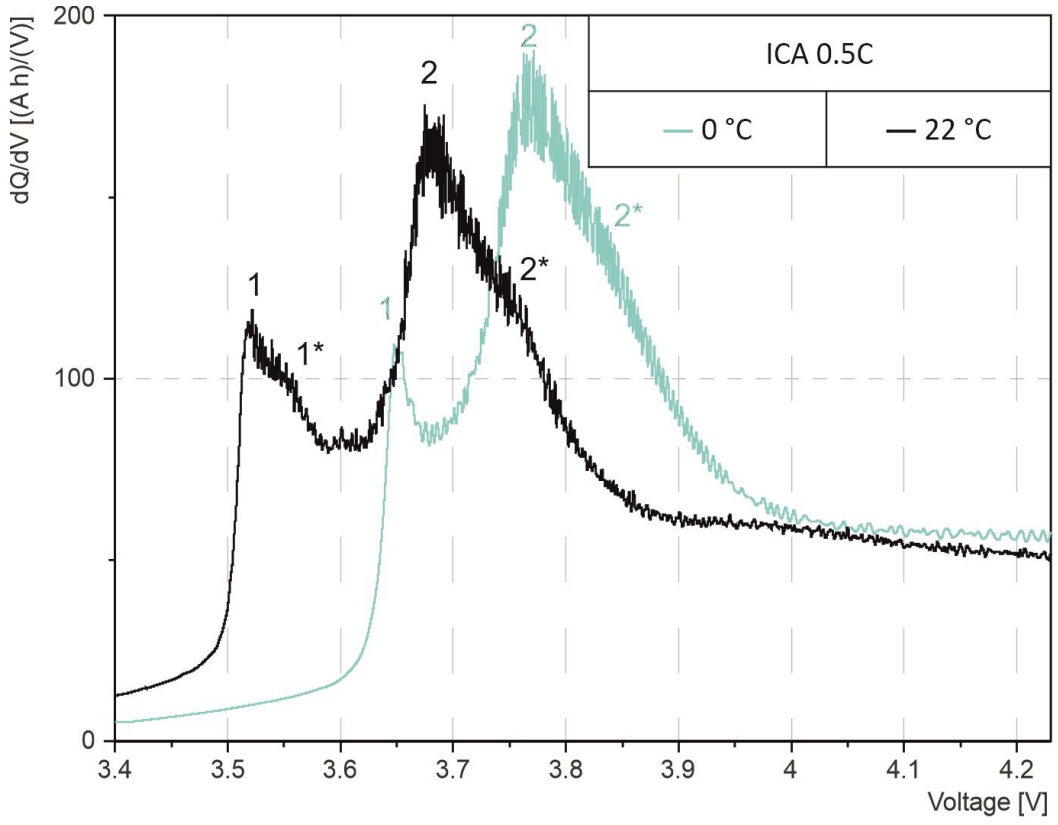

Figure 4.9: Incremental Capacity Analysis - Reference test 0.5C with 0 °C & 22 °C

In Figure 4.10 the ICA graphs for different C-rates are shown at a temperature of 22 °C. 1C, 1.5C, 2C and 3C curves are colored in red, green, blue and purple. This color coding is the same in all further ICA graphs. For the 1C ICA curve a first peak is prominent at ~3.58 V. Additional two peaks occur at ~3.72 V and ~3.85 V. In higher voltage regions no slope changes or plateaus can be seen. The 1.5C ICA curve has three peaks at ~3.62 V, ~3.77 V and ~3.85 V. A slight slope change can be seen above ~4.1 V. In comparison with the lower C-rate of 1C, the whole curve shows a shift to the right and the peak intensions in the lower voltage regions are reduced. For the 2C ICA curve a first peak at ~3.7 V is prominent and a second one between ~3.8 V and ~3.95 V is recognized. At this C-rate an additional peak 4 occurs at ~4.08 V. 3C ICA curve shows a slope change 1 at ~3.76 V and a peak 2 at ~3.87 V. This purple curve has a prominent LP peak 4 at a voltage of ~4.12 V, which shows a shift to the right compared to the 2C LP peak. For these ICA curves at 22 °C a higher C-rate leads to a curve shift to higher voltage regions and the peak intensities at lower voltages are reduced. Further an additional LP peak arise with increasing C-rate. For higher C-rates the signal noise increases, which is visible for the 3C curve.

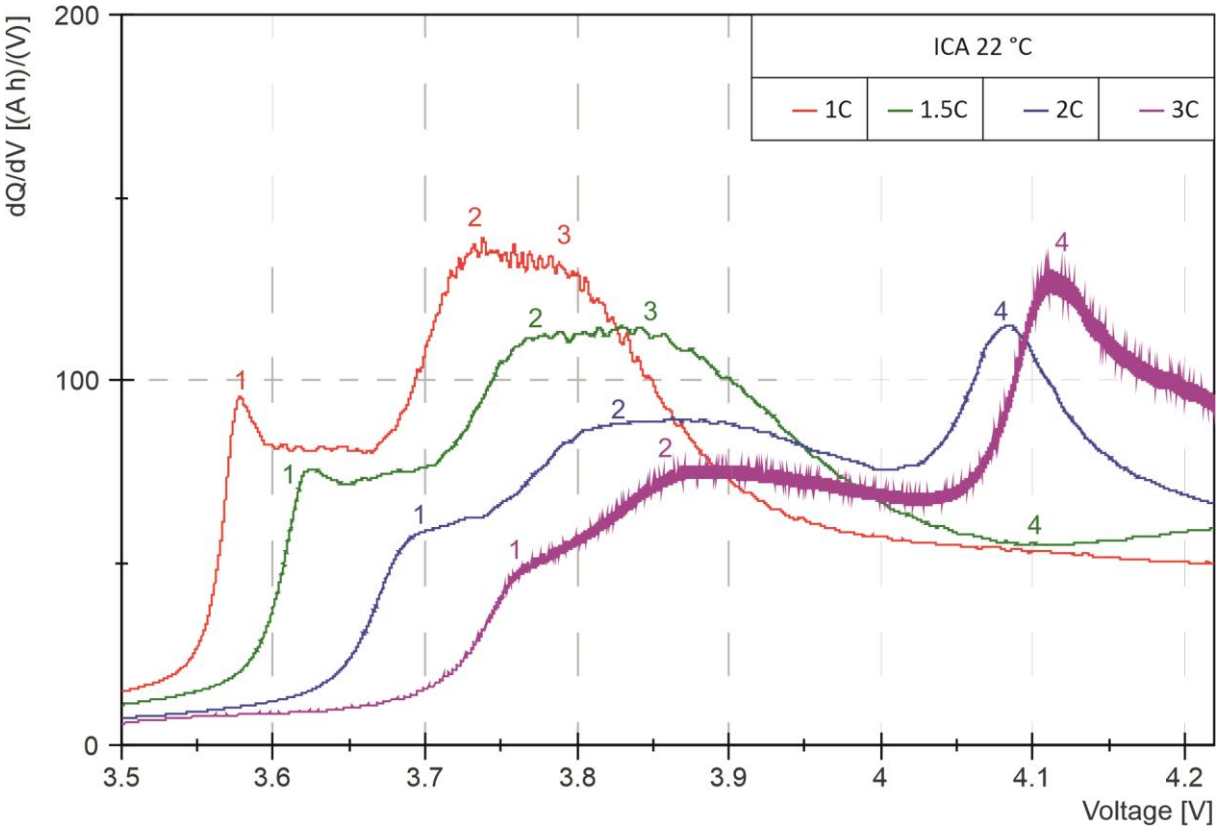

Figure 4.10: Incremental Capacity Analysis - 22 °C & all C-rates

The ICA curves for the four C-rates at a temperature of 10 °C are shown in Figure 4.11. For the 1C ICA curve two peaks are prominent at voltages of ~3.62 V and ~3.8 V. In voltage regions above 4V no slope changes or peaks are visible. The first peak of the 1.5C ICA curve occurs at ~3.68 V, followed by a second one at ~3.85 V and a small peak at ~4.13 V. For the 2C ICA curve a slope change at ~3.81 V and a peak at ~3.95 V is visible. This C-rate shows an additional pronounced peak at ~4.16 V, which is referred to a filter artefact. The purple 3C ICA curve has two visible slope changes at ~3.94 V and ~4.05 V. An additional peak 4 for the LP occurrence at ~4.22 V is prominent. It can be seen that with higher C-rate the curve shifts to higher voltage regions, the peak intensities at lower voltages are reduced and an additional peak arise in higher voltage regions. For higher C-rates the LP peak is shifted towards higher voltages. In comparison with the 22 °C ICA curve, Figure 4.10, all reaction peaks shift to higher voltages towards the right on the x-axis. With higher temperatures a decrease in the peak intensity can be seen for all the C-rates.

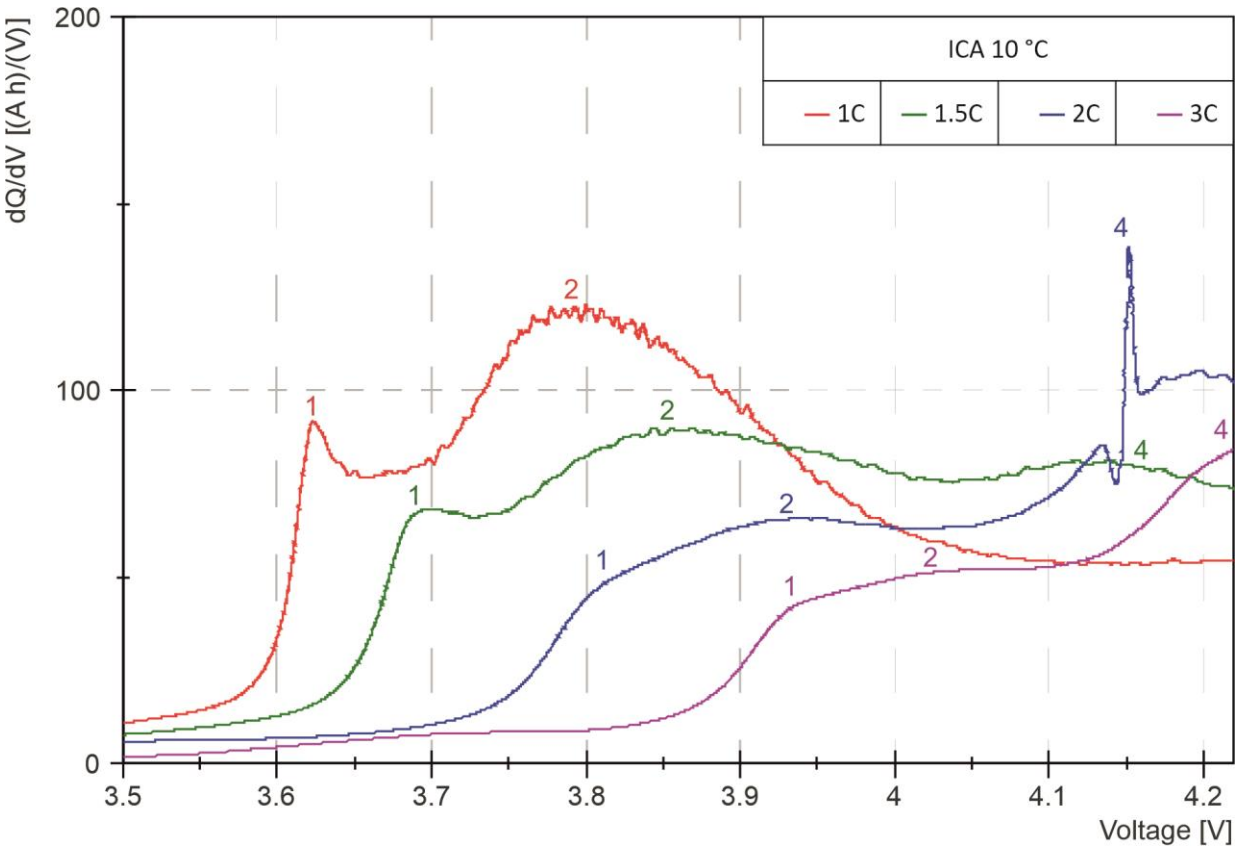

Figure 4.11: Incremental Capacity Analysis - 10 °C & all C-rates

In following Figure 4.12 the ICA curves for different C-rates at a temperature of 0 °C are shown in more detail. For the red 1C ICA curve a first peak at ~3.72 V, a second one at ~3.87 V and

an additional LP plating peak 4 can be observed at ~4.11 V. The 1.5C ICA curve shows a slight change in slope at ~3.82 V and two separate peaks at ~3.96 V and ~4.15 V. For the 2C curve in blue only slope change is visible at ~4 V, but a clear LP peak 4 at a voltage of ~4.17 V. No reaction in lower voltage regions below ~4 V is prominent for the 3C ICA curve. In higher voltage regions a pronounced peak 4 at ~4.18 V is observed for the highest C-rate curve, which is referred to a filter artefact. All of the reactions in the 0 °C curves show a shift to higher voltage with an increased C-rate. Also, the peak intensities in lower regions are reduced for higher C-rates and additional peak arise in higher voltage regions. In comparison with the ICA curves at higher temperatures, all reaction peaks shift to higher voltages. Also, the peak intensities in voltage regions below 4 V reduced and the peak intensities above 4 V increased.

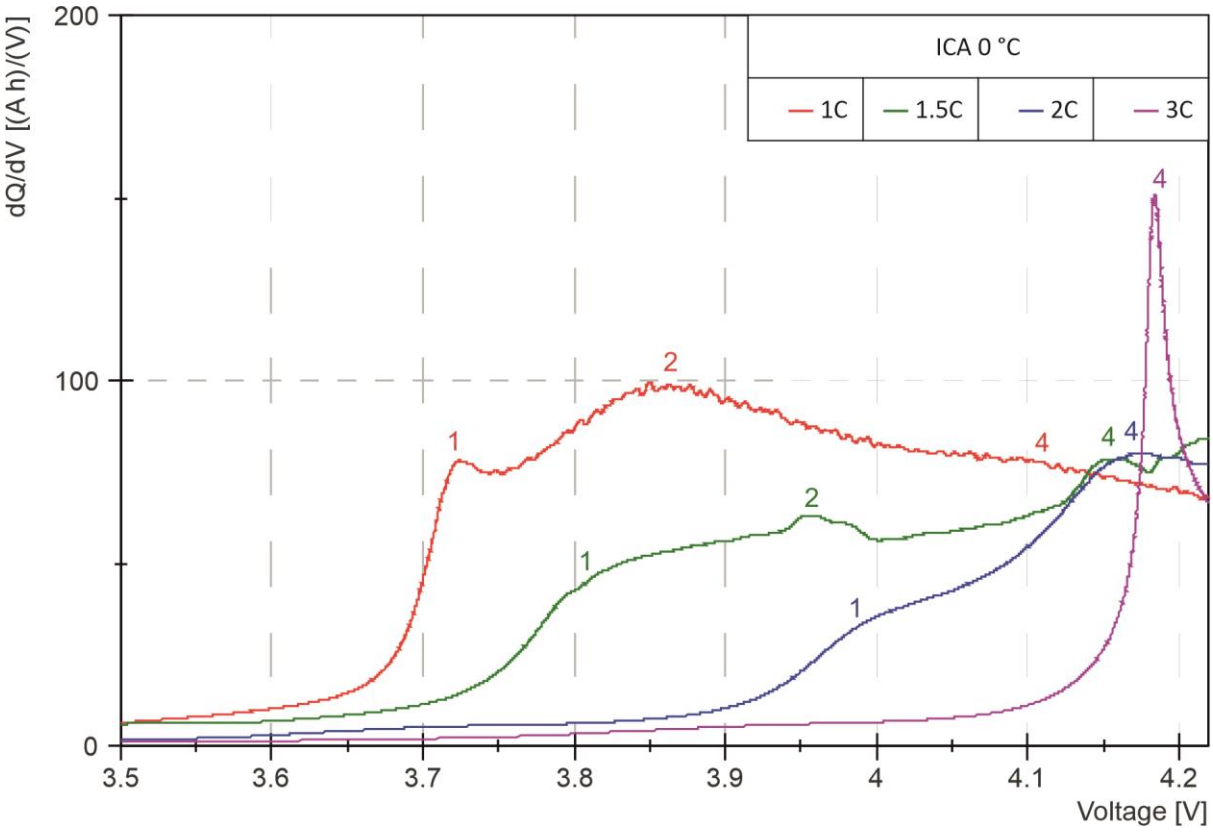

Figure 4.12: Incremental Capacity Analysis - 0 °C & all C-rates

The incremental capacity analysis curves show the appearance of an additional LP peak for lower temperatures and higher C-rates. With the lowest temperature of 0 °C the peak occurs also for the lowest cycling rate of 1C. For all the curves a shift of the reaction peaks towards higher voltages and a reduced intensity of the peaks in voltage regions below ~4 V can be seen for higher C-rates. For higher C-rates and lower temperatures an increase of the plating peak

can be seen. Based on the results of the ICA curves the test matrix is filled up for all the combination of C-rates and temperatures, Table 4.3. For all green marked combinations, clear visible signs for the onset of LP during the charging cycles are identified.

Boundary Conditions					
		C-rate			
Temperature		1 C	1.5 C	2 C	3 C
	22 °C	No	Observed	Prominent	Prominent
	10 °C	No	Prominent	Prominent	Prominent
	0 °C	Prominent	Prominent	Prominent	Prominent

Table 4.3: Test Matrix for pre-study with C-Rates and temperatures – Results Incremental Capacity Analysis

4.4 Anode Potential Measurement

The main focus in this sub chapter lies on the results of the identification of lithium plating with the anode potential measurement (AP), as described in chapter 2.5.1. For this method the reference electrode cell, shown in chapter 3.1.4.1, is cycled under the pre-defined boundary conditions of the test matrix. Before the initial cycles the same EC cycles, as illustrated in Figure 4.16, are performed, to check that the insertion of the RE has no effect on cell behavior. The voltage profiles, of the EC cycles before and after the insertion, have the same slope changes at the same voltage and overlap the red voltage curve in Figure 4.16. As the other described methods show clear lithium plating hints for 1.5C, only the results for this C-rate are shown in this chapter. Figure 4.13 illustrates the anode potential measurement for 1.5C at 10 °C during the relaxation phase after the first charge cycle. Both electrode voltages and the cell voltage are plotted unfiltered and unsmoothed on three different y-axes over the time on the x-axis. For the cell voltage in red a clear plateau is visible until ~0.28 h afterwards the voltage relaxes to ~4.04 V. This correlates to the VRP without the RE at this C-rate and temperature, illustrated in Figure 4.3. The cathode voltage in green nearly has the same plateau until ~0.31 h and relaxes to ~4.23 V. For the anode voltage in blue a slight decrease to a minimum voltage of ~0.156 V is visible during the relaxation period.

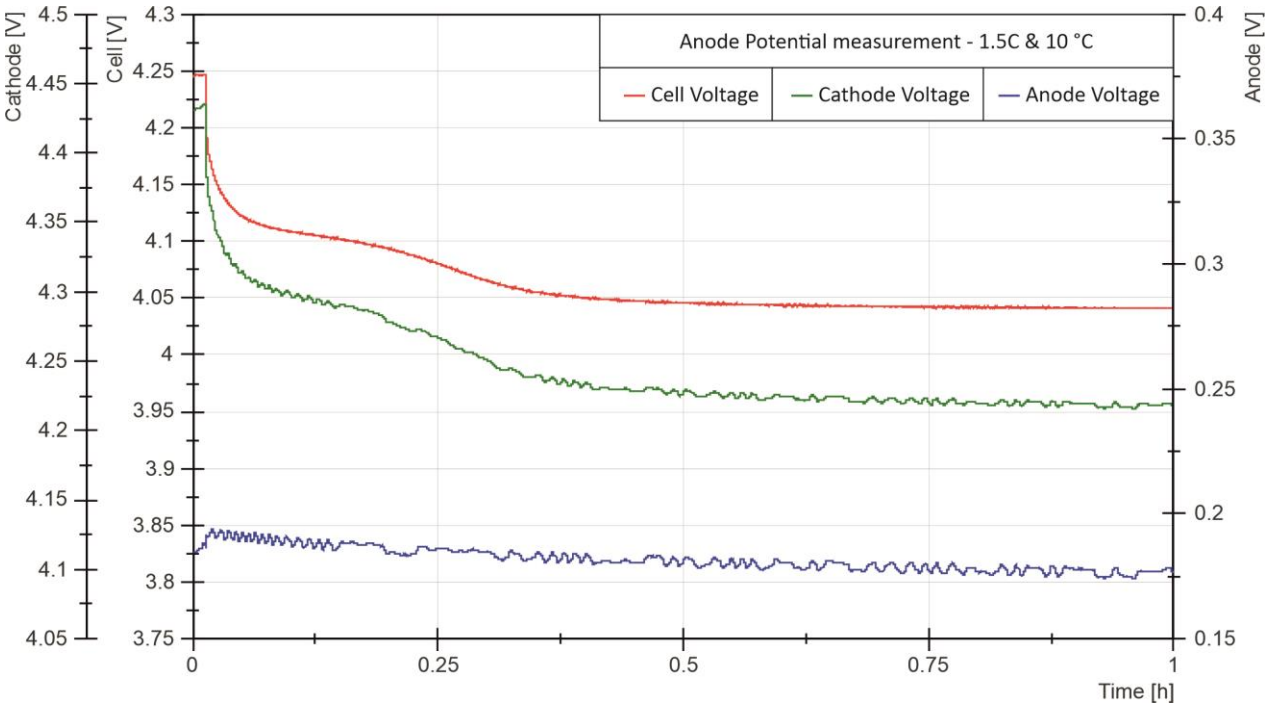

Figure 4.13: Anode Potential Measurement during relaxation – 1.5C at 10 °C – first measurement

Because of the signal noise, visible in Figure 4.13, an improved test setup with new shielded cables, directly connected from the cell tabs to BATMAN, is used. Additional, only the cell voltage and the anode voltage are measured, because additional tests show influence of the cathode on the anode signal. The additional measurement at 1.5C and 10 °C is illustrated in Figure 4.14. For the cell voltage a broad plateau with a time duration of ~0.35 h is visible and the voltage relaxes to ~4.08 V. Compared to Figure 4.13 the voltage plateau occurs at higher voltages and the duration is increased. It has to be mentioned that these tests are not performed directly after each other and should only show the signal noise improvement. For the anode the voltage relaxes to ~0.177 V and no change in slope or drop below 0 V is visible.

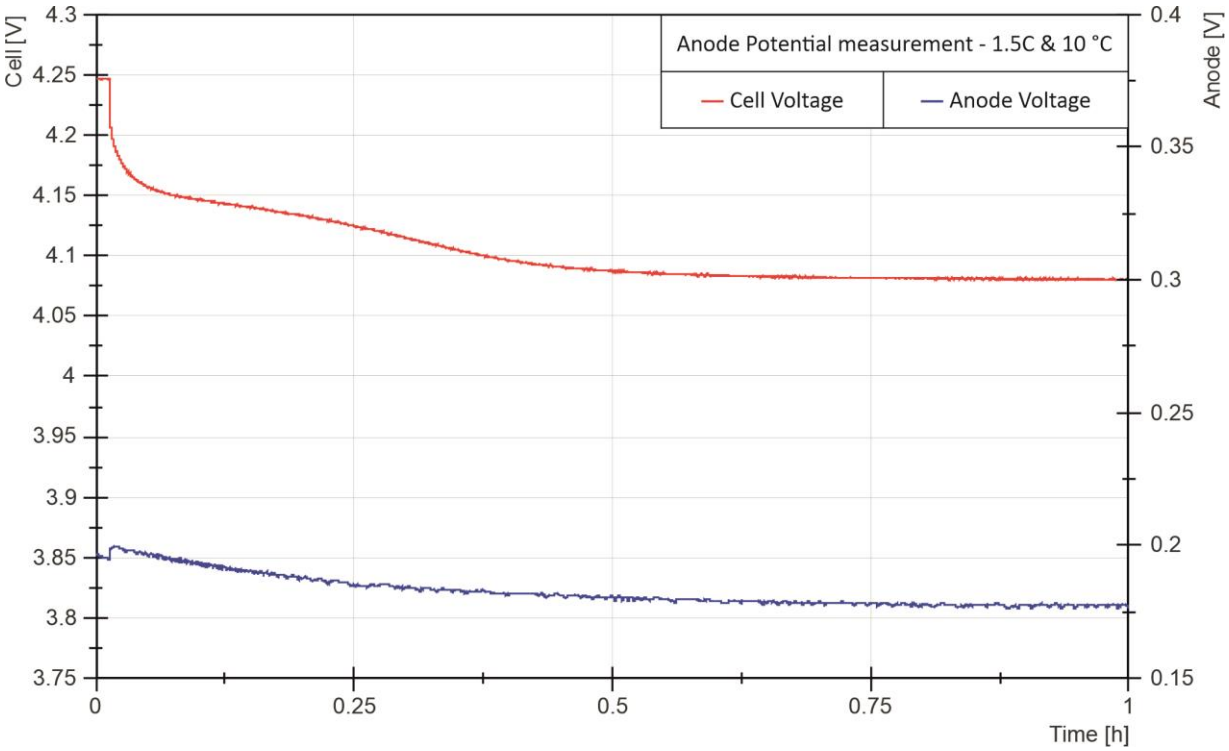

Figure 4.14: Anode Potential Measurement during relaxation – 1.5C at 10 °C – updated test setup

Additional to the relaxation voltages Figure 4.15 illustrates the cell voltage and the anode voltage during the charge cycle. The anode voltage in blue starts from ~0.25 V and drops down to ~0.17 V during the charge cycle. A slight slope change is visible at the change into CV-phase but no drop below 0 V occurs.

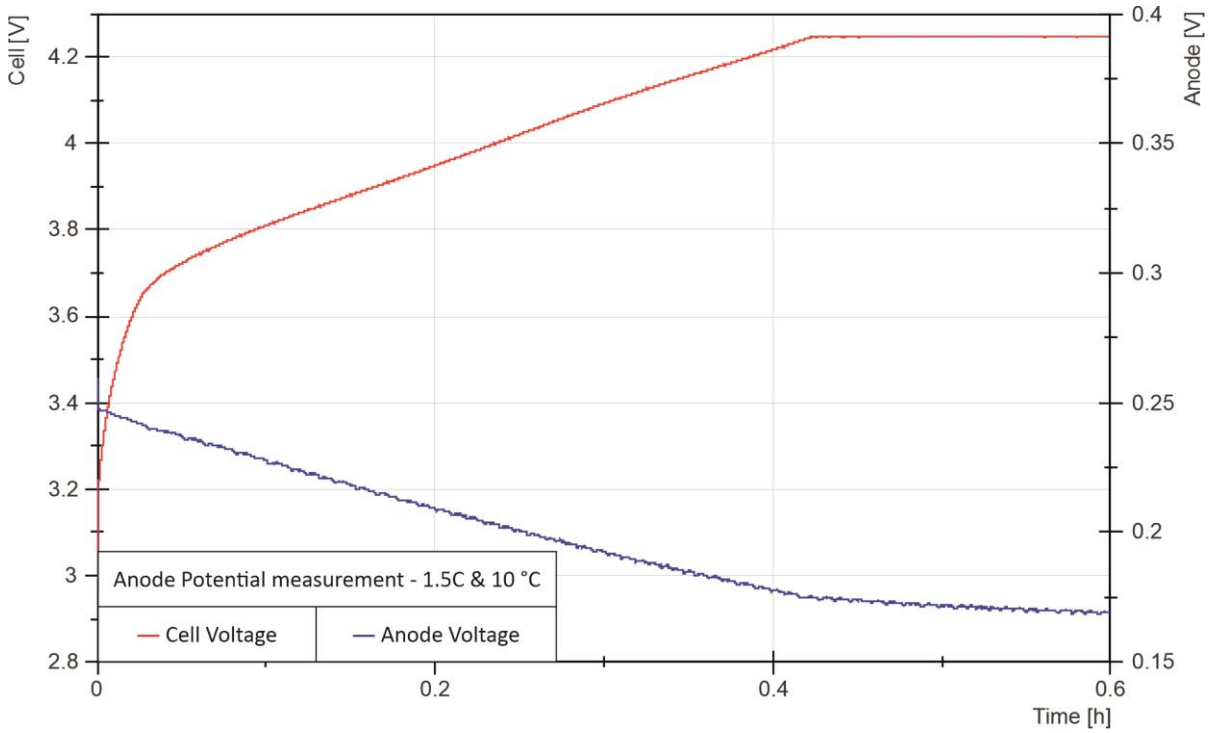

Figure 4.15: Anode Potential Measurement during charging – 1.5C at 10 °C – updated test setup

The anode potential measurement shows no drop of the anode potential below 0 V vs Li/Li^+. Based on this, the test matrix is filled up for all the combination of C-rates and temperatures with "No" sign for LP, Table 4.4.

Boundary Conditions					
		C-rate			
Temperature		**1 C**	**1.5 C**	**2 C**	**3 C**
	22 °C	**No**	**No**	**No**	**No**
	10 °C	**No**	**No**	**No**	**No**
	0 °C	**No**	**No**	**No**	**No**

Table 4.4: Test Matrix for pre-study with C-Rates and temperatures – Results Anode Potential Measurement

4.5 Temperature Evaluation

As mentioned in the experimental Chapter 3.1.3, the temperature control during the cell cycling is done by the Thermofixl. Following Table 4.5 shows the cell temperature evaluation during the pre-study tests based on the test matrix. For each C-rate and temperature combination the maximum, minimum and delta values are shown. The first two values are

determined by calculation of the average temperature of all ten temperature control modules during the whole cell cycling. Based on this, the Δ T is calculated by subtract the maximum and minimum temperature values. At a stable temperature, higher C-rates lead to more temperature difference during the cycling process. This evolution is also visible by comparing one C-rate for decreasing temperatures. A decrease in the temperature goes hand in hand with an increase in the temperature difference. With a minimum Δ T value of 0.1 °C at 1C & 22 °C and a maximum Δ T value of 0.763 °C at 3C & 0 °C a maximum temperature deviation of 3.3 %, based on a room temperature of 23 °C, was measured. This deviation during the cell cycling is considered to be in a neglect able range and the test result can be interpreted as unaffected.

	Boundary Conditions					
			C-rate			
Temperature			**1 C**	**1.5 C**	**2 C**	**3 C**
	22 °C	**Max. T. [°C]:**	21.977	22.054	22.019	22.135
		Min. T. [°C]:	21.877	21.938	21.865	21.863
		Δ T [°C]:	0.100	0.116	0.154	0.272
	10 °C	**Max. T. [°C]:**	10.145	10.215	11.087	10.317
		Min. T. [°C]:	10.048	10.055	10.647	10.06
		Δ T [°C]:	0.097	0.160	0.440	0.257
	0 °C	**Max. T. [°C]:**	1.360	1.712	1.659	1.258
		Min. T. [°C]:	0.915	1.184	1.042	0.495
		Δ T [°C]:	0.445	0.528	0.615	0.763

Table 4.5: Cell temperature maximum and minimum values during cycling

4.6 Main-study cycling

This sub chapter deals with the results of the main-study, where cells are cycled over 20 cycles with the before found out BC to induce LP and reach a SoH of about 80 %. An overlap of the previous shown test matrixes makes 1.5C in combination with a temperature of 10 °C to the most promising boundary condition to induce LP during cell cycling. After cell cycling, the results are analysed with three electrochemical LP identification methods and a comparison of the electrical characterization cycles shows the calculation of the SoH and its evolution during storage. Following Figure 4.16 shows the voltage profile of the EC before the cycles

(red curve), the EC directly after the 20 cycles (green curve) and the EC 140 h after the 20 cycles plotted over time. In the overlay of the green and blue curve no change in slope is visible. The blue curve has a slightly longer charging CC-phase and is therefore shifted to the right. For another cell the comparison of the EC cycles before, directly after and 67h after the 20 cycles is done. Between 67 h and 140 h after the cycling procedure no fading of the effect is seen, as illustrated in Appendix A.1.

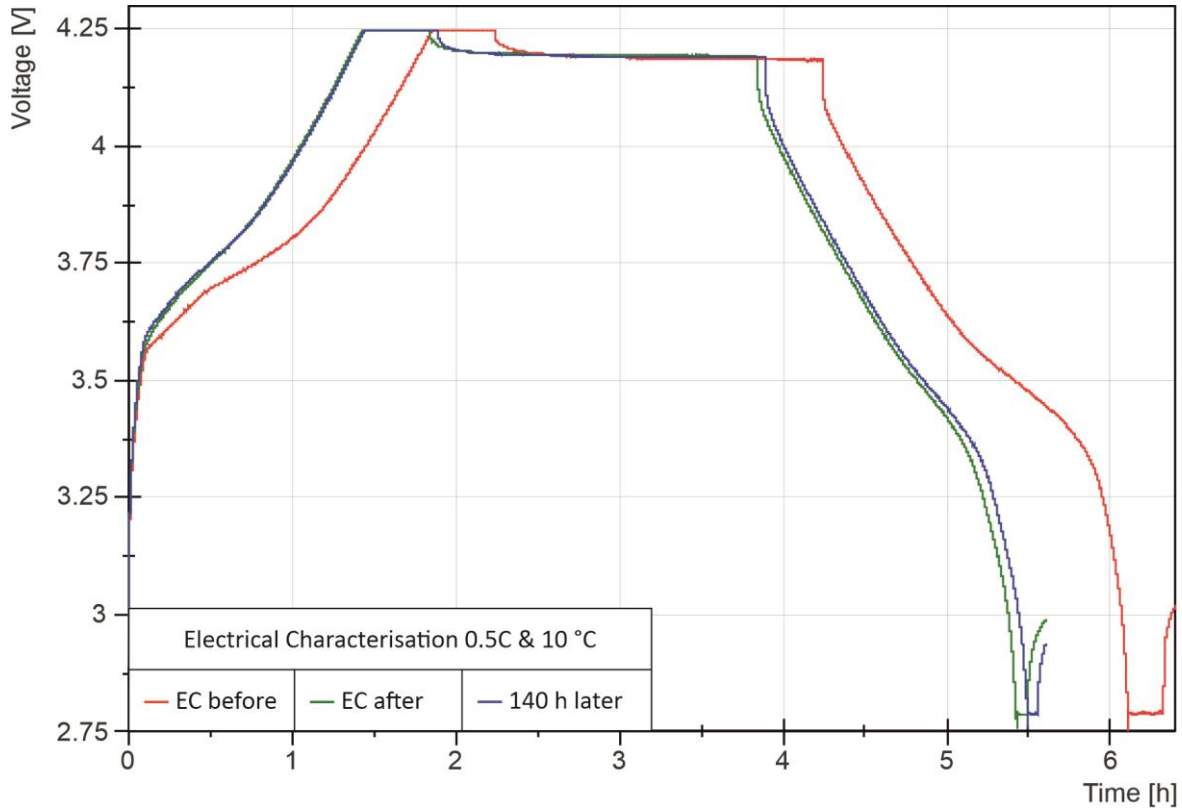

Figure 4.16: Electrical Characterization test cell 1 - before vs. after 20 cycles vs. 140 h later

To compare the SoH out of these EC curves, the capacity is calculated with integration of the charging current over the CC-phase charging time. For the initial SoH 100 % the EC cycle before the cycles is used. Following Table 4.6 shows the result of the SoH comparison.

	Calculated Capacity [Ah]	**SoH [%]**
EC before 20 cycles	65.50	100
EC after 20 cycles	52.27	79.8
EC after 140h storage	52.48	80

Table 4.6: SoH comparison before and after the main-study cycling

In Figure 4.17 the VRP (continues curves) and their time derivatives (dotted curves) of the 20 cycles are illustrated. The golden curve deals as a reference where no plateau in the VRP and no peak in the dV/dT is visible. As already seen in the chapter before, the 1st cycle at these boundary conditions has a prominent plateau in the VRP and relaxes to a voltage of ~4.06 V. Also, a peak in the time derivative is prominent in the 1st cycle. For the 5th and 10th cycle the plateau slightly decreases its width in comparison to cycle 1. This is also visible in the shift of the peak position towards shorter time. The 15th and 20th cycle show again an increase in the plateau width and a shift of the peak towards the right on the x-axis. The amplitude of the peak first decreases with the cycles and increases after the 10th cycle. A maximum peak amplitude occurs for the 20th cycle and a shift of the relaxation voltage towards higher voltages is visible.

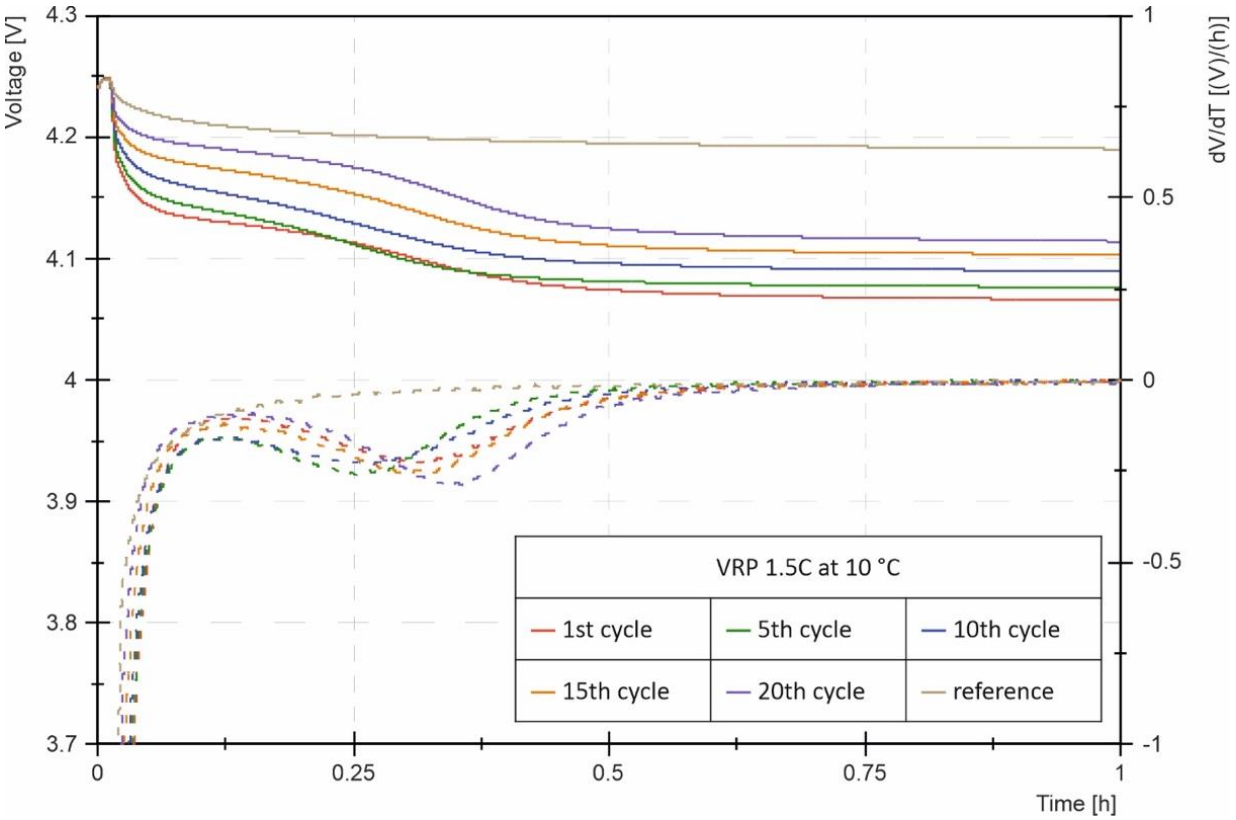

Figure 4.17: Voltage Relaxation Profile comparison of main-study cycling

The DVA of the 20-cycle main-study with 1.5C at a temperature of 10 °C is illustrated in Figure 4.18 . For better data illustration not all 20 cycles are plotted, only the cycles before the relaxation are shown. A reference test where no peak is observed is shown with the gold-colored curve. The 4th cycle, represented by the orange curve, has a prominent peak at a

capacity of ~10 Ah. During further cycles until cycle 9 the peak flattens out and occurs at a capacity of ~8.5 Ah. An increase in the capacity can be seen for the 14th cycle. There, the peak is visible at ~11 Ah. For cycle 19 the peak position shift towards ~12 Ah and it shows an increased amplitude compared to cycles before.

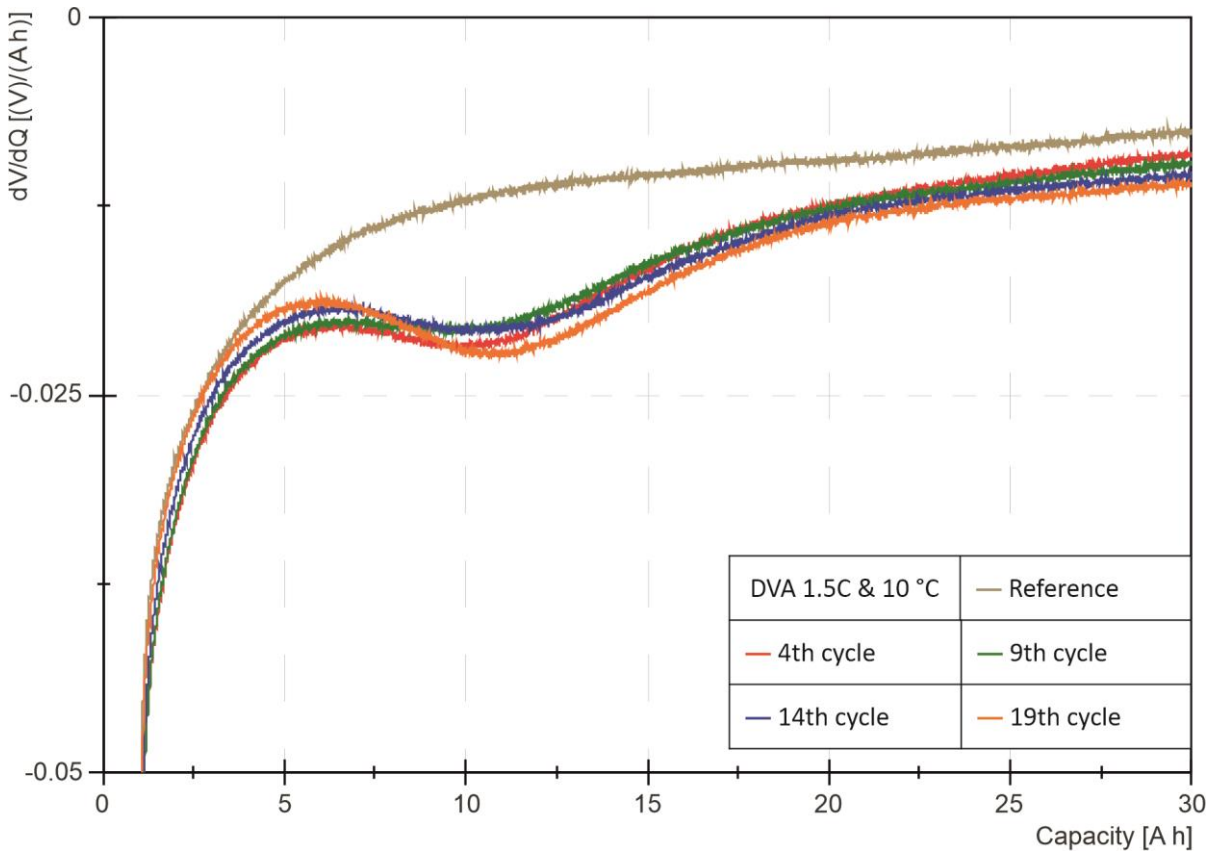

Figure 4.18: Differential Voltage Analysis comparison of main-study cycling

Figure 4.19 shows the ICA comparison of the main-study cycling with 1.5C at 10 °C for 20 cycles in a row. For the reference curve in turquoise 2 peaks are visible. A first one at ~3.57 V, related to the lithium intercalation [54], [12], and a second one at ~3.71 V, related to the NMC phase change [44], [12]. This reference curve shows no additional lithium plating peak in higher voltage regions above ~4 V. The ICA curve of the first cycle, colored in purple, has three prominent peaks at ~3.7 V, ~3.86 V and ~4.06 V. For cycle 2 the 1st peak occurs at ~3.68V. With increasing cycles this 1st peak shift to higher voltages, decrease its intensity and disappear after ~8 cycles. The 2nd peak shows a similar shift to ~3.84V compared to the 1st cycle. Ongoing cycling decreases the peak intensity and shifts the peak slightly towards higher voltages. Compared to the first cycle lithium plating peak, the second cycle only shows a slight slope

change at ~4.05 V. This slope change decreases until ~7th cycle and increases after ~8th cycles to a maximum peak intensity for cycle 20.

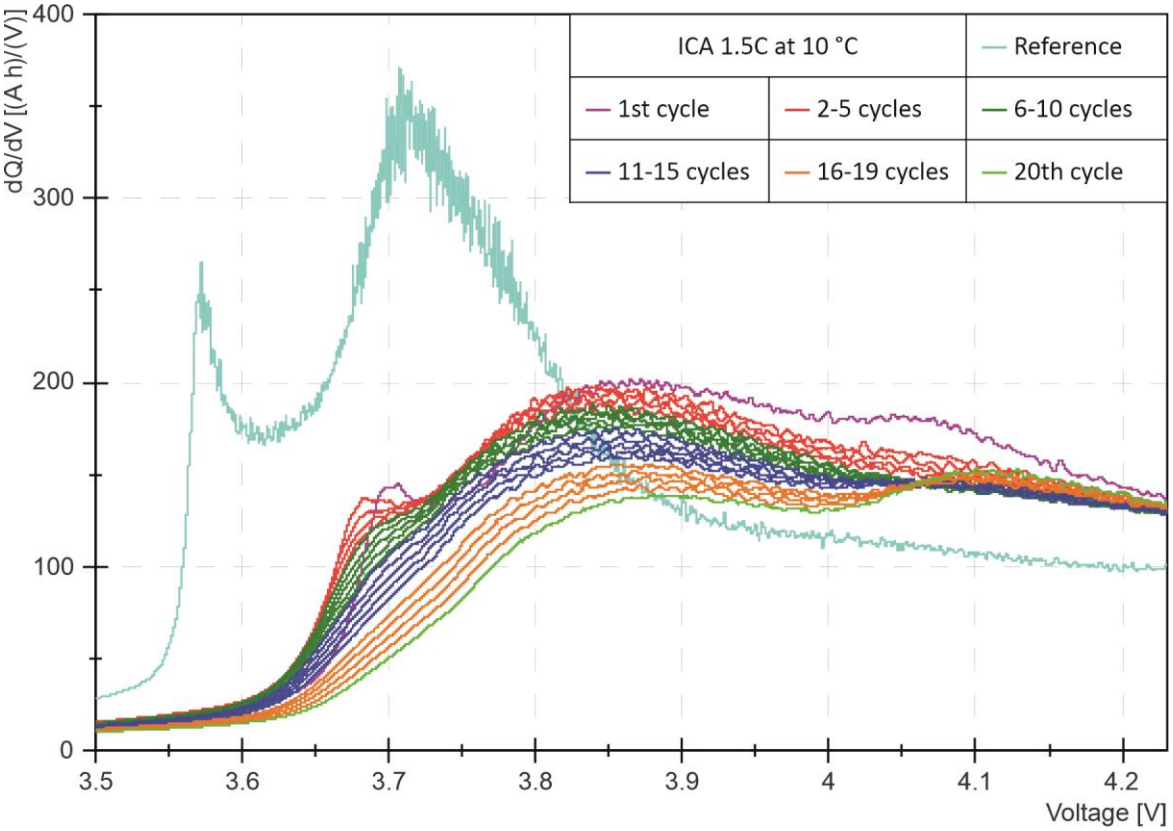

Figure 4.19: Incremental Capacity Analysis comparison of main-study cycling

5 DISCUSSION

In this chapter the previously shown results are discussed in more detail. An interpretation of the results and comparison with the theoretical background is done for the described electrochemical identification methods.

5.1 Voltage Relaxation Profile

Based on the literature, the VRP has a prominent plateau when lithium plating occurred during charging [23], [42], [51]. It arises during the relaxation phase through the chemical intercalation of deposited lithium into the graphite anode material [42], [51]. For some of the boundary condition this plateau is clearly visible in the test results. With a look on the time derivative curves, a peak occurs at the steepest point in the VRP and represents the point, when the lithium stripping rate is decreased [42]. Overall, the tests show an increase of the VRP plateau with increasing C-rates, but only until a specific value. The decrease in the plateau length for higher C-rates is explained with the shortened charging CC-phase as a result of the increased cell polarization [13]. In case of a shortened charging CC-phase, less lithium ions are moved to the anode side due the shortened charge time and can form metallic lithium on the surface. This phenomenon can be seen in the comparison of the 2C and 3C graphs. A clear decrease in the VRP plateau time duration and a shift of the derivative peak position to the left is visible. Another reason for a decrease of the 3C plateau could be the dendrite formation. For higher C-rates the dendrite formation is more sharp needle-like in comparison with smaller mossy-like dendrites for lower C-rates [61]. The thinner peaks can break easily and form dead lithium [18]. The effect of lithium stripping is therefore decreased, but the amount of irreversible lithium plating is increased. For lower temperatures, the results show a clear increase in the VRP plateau time duration and an increased peak width in the time derivative. Again this is related to a higher amount of lithium stripping during the relaxation time after charging with lower temperatures [45]. For lower temperatures the effect of higher cell polarization is observed with lower relaxation voltages in the VRP, but this effect is much more influenced by the C-rate. The overall lithium stripping duration increases much more for lower temperatures compared to higher C-rates.

5.2 Differential Voltage Analysis

In the DVA, a peak at the start of the discharge process represents the occurrence of the lithium stripping process [43]. Overall, the graphs show clear visible peaks for some of the boundary conditions. For lower temperatures and higher C-rates a peak occurs in lower capacity regions. Until 2C, an increasing C-rate leads to a shift of this lithium stripping peak to higher capacities. This is a sign for a higher amount of plated lithium during charging and lithium stripping during discharging [43], [46], [48], [49]. For C-rates of 3C the peak width decreases and shows a less lithium stripping amount compared to 2C. This decrease for higher C-rates is again explained with the shortened charging CC-phase as a result of the increased cell polarization, reference to Chapter 5.1. This shortened CC-phase during discharging can be seen in a DVA curve end at lower capacities for higher C-rates. Again the dendrite formation in combination with the C-rate has to be considered, as explained in the VRP before [18], [61]. For lower temperatures the mentioned increase in the DVA peak and plated lithium amount is confirmed [43]. The results show a peak shift towards higher capacities on the x-axis and also the amplitude increases for reduced temperatures with same C-rates. A sharpness and deepness increase of the peak is referred to lithium plating hot spots and less homogenous plating on the graphite surface [62]. As also seen in the VRP, the temperature has much more influence in the lithium stripping duration as the C-rate. In the results it can be seen that low temperatures in combination with high C-rates lead to a reduction of the small signal changes in lower capacity regions, referred to the lithium de-intercalation out of the anode [49], and further to a reduction of the signal reaction in higher capacity regions, referred to the intercalation process in cathode [49]. Therefore, it is assumed that lithium plating is the most prominent cell reaction in these tests.

5.3 Incremental Capacity Analysis

Literature shows, that each peak in the ICA is related to an electrochemical reaction inside the cell [12], [44], [53], [55]. A peak in lower voltage regions of the curve belongs to the intercalation process in the negative electrode [12], [54] and peaks in higher voltage regions are referred to the NMC phase change and solid solution [12], [44]. For this method, an additional peak arises in voltage regions above 4 V when lithium plating happens and increases its size for lower temperatures in combination with higher C-rates [44]. Compared to the results, the reference curve shows no onset of lithium plating during the charging process. An

increased C-rate at stable temperature shows a curve shift towards higher voltages on the x-axis. The peaks at lower voltage regions, related to the lithium intercalation process into the graphite anode [12], [54], disappear at high C-rates. It is assumed that all of the lithium is plated on the active material during these cycles. It can be seen that the peaks, which are referred to the NMC phase change and the solid solution in the active material [12], [44], flatten out for an increased C-rate. This is related to the high cell polarization and the high current gradient at the positive electrode. A high lithium plating amount is assumed, which decreases the LLI. This indicates that the amount of available lithium in the NMC decreases and leads to a decrease of the peak. For higher C-rates the tests show the additional lithium plating peak above 4 V. With lower temperatures this plating peak also arises for low C-rates and a shift of the curve to higher voltages is visible. This occurs due to the higher cell polarization at lower temperatures. Additionally, a reduction of the peaks in lower voltage regions and a rise of lithium plating peaks is visible for lower temperatures with the same C-rate. This serves again as an indicator that no intercalation reactions take place and lithium is plated on the anode surface. The surface under the ICA charging curve is related to the capacity. A decrease of the capacity with increasing lithium plating peaks is visible in the results. This strengthens the fact that lithium plating leads to a loss of capacity.

5.4 Anode Potential Measurement

Based on the literature, the drop of the anode potential below 0 V vs. Li/Li^+, is the most reliable sign for the detection of lithium plating, because then LP is thermodynamically possible [1], [3], [13]. The voltage relaxation profile, the differential voltage analysis and the incremental capacity analysis show prominent lithium plating signs for cycles with 1.5C and temperatures of 10 °C or below. In the anode potential measurements, no drop below 0 V vs. Li/Li^+ is visible for this BCs during the charging process, as illustrated in Figure 4.15. This calls the correct use of this method in question. A possible error source could be the inserted reference electrode. The material, location, and size of the reference electrode can affect the potential measurements [57], [58]. Due to this, the initial resistance might be too high and the anode voltage curve never reaches regions of 0 V vs. Li/Li^+. Another possible error source could be due to anode active material mixture out of graphite with silicon particles. Silicon has working potential of about 400 mV vs. Li/Li^+ [63]. Due to the particles mixed in the graphite active material, the overall anode potential could be increased and therefore never reaches the

region of 0 V vs. Li/Li^+. This could also be an indication for underpotential lithium plating [64]. Further, the measurement of the anode and cathode potential calls the use of the VRP as an identification method for LP in question. The results during the relaxation phase show only a visible plateau in the cathode voltage signal, as shown in Figure 4.13. No notable changes are observed in the anode voltage curve and the cathode voltage follows the slope of the overall cell voltage curve. Therefore, it is assumed that the whole reaction takes place at the positive electrode.

5.5 Main-study cycling

The main-study results, which are based on the cell cycling with 1.5C and 10 °C for 20 cycles, show a decrease of the SoH to 80 %. An additional electrical characterization cycle, performed some storage time after the cell cycling, shows no fading effect of the capacity. Only a slight increase due to the cell polarization after cycling is visible, which was expected. The comparison of the VRP, DVA and ICA over the 20 cycles show similar correlations. For the first cycle all methods show their respective signs which are referred to lithium plating. A plateau in the VRP, a peak in the DVA and an additional peak in the ICA are visible. This is a clear indicator for the occurrence of lithium plating since cycle 1. Until cycle 8 a decrease in the lithium plating amount is observed. The plateau length in the VRP gets shorter, the DVA peak position shifts to lower capacities and the plating peak in the ICA decreases. After the 8^{th} cycle the lithium plating sing increase in every method and reach its maximum for the 20^{th} cycle. This reduction after the first cycle with a subsequent increase of the lithium plating sign is interpreted as follows. It is assumed that the first cycle acts like a formation cycle for the fresh cell, where a first expansion of the graphite anode happens and cracks in the SEI layer occur. At these cracks a new SEI is formed and during further cycling the cell stabilize these processes. It also has to be taken into account that the overall cell cycling leads to a cell degradation and reduces the capacity [4].

6 CONCLUSION

In this thesis LP, as an ageing mechanism, is studied in commercially available high energy pouch cells. Favourable BCs were evaluated with special cycling programs to induce the deposition of metallic lithium on the graphite anode. VRP, DVA, ICA and AP as non-destructive identification methods were investigated to analyse this ageing mechanism in LIBs. The cycling of commercial pouch cells showed that LP is an intensified reaction for increasing C-rates and decreasing temperatures. For both BCs, the cells showed a higher sensitivity to temperatures rather than the charging rate. With a cycling temperature of 10 °C in combination with 1.5C clear signs of LP are visible in high energy cells, for 0 °C LP occurred also with 1C. For too high C-rates the increased cell polarization must be taken into account during cell cycling, which affects the amount of LP due to a shortened charging CC-phase.

To analyse LP in commercial high energy pouch cells DVA and ICA successfully showed lithium plating signs. VRP showed clear visible signs in form of lithium stripping plateaus in the cell voltage, but the additional measurement of each electrode potential calls this identification method in question. There, the stripping plateau is only visible in the cathode potential. For the anode potential the plateau would be expected during relaxation, but no changes in signal are observed after cell charging with LP favourable BCs.

Also, the measurement of the AP in commercial pouch cells should be viewed with caution, because this method did not show the potential drop below 0 V vs. Li/Li^+. There, the cell characteristic with the special graphite/silicon anode active material and the whole reference electrode setup must be taken into account. The use of this method for non-pure graphite anodes is called in question.

Both, VRP and AP, give hints for further study on these specific methods. An outlook for the DVA could be a further study of the LP mass quantification based on the work from literature. After the identification of feasible LP boundary conditions and methods for identification, artificial aged cells with a SoH of 80 % and primarily LP as ageing mechanism were successfully produced for further studies. To verify the used electrochemical methods for the identification of LP in commercial cell, destructive methods can be used on the before mentioned artificial aged cells.

7 REFERENCES

[1] X. Lin, K. Khosravinia, X. Hu, J. Li, and W. Lu, “Lithium Plating Mechanism, Detection, and Mitigation in Lithium-Ion Batteries,” *Progress in Energy and Combustion Science*, vol. 87, p. 100953, 2021, doi: 10.1016/j.pecs.2021.100953.

[2] IEA (2023), Global EV Outlook 2023, IEA, Paris, “Trends in electric light-duty vehicles,” [Online]. Available: https://www.iea.org/reports/global-ev-outlook-2023/trends-in-electric-light-duty-vehicles

[3] Q. Liu *et al.,* “Understanding undesirable anode lithium plating issues in lithium-ion batteries,” *RSC Adv.*, vol. 6, no. 91, pp. 88683–88700, 2016, doi: 10.1039/C6RA19482F.

[4] X. Han *et al.,* “A review on the key issues of the lithium ion battery degradation among the whole life cycle,” *eTransportation*, vol. 1, 1–2, p. 100005, 2019, doi: 10.1016/j.etran.2019.100005.

[5] Automotive Cells Company, *Battery Cell, Module or Pack. What's the difference?* [Online]. Available: https://www.acc-emotion.com/stories/battery-cell-module-or-pack-whats-difference-infographics

[6] R. Korthauer, *Handbuch Lithium-Ionen-Batterien*. Berlin, Heidelberg: Springer Berlin Heidelberg, 2013.

[7] C. v. Lüders, *Experimentelle und simulative Untersuchung von Lithium-Plating und Lithium-Stripping in Lithium-Ionen-Zellen*. München: Universitätsbibliothek der TU München, 2019.

[8] S. Goriparti, E. Miele, F. de Angelis, E. Di Fabrizio, R. Proietti Zaccaria, and C. Capiglia, “Review on recent progress of nanostructured anode materials for Li-ion batteries,” *Journal of Power Sources*, vol. 257, pp. 421–443, 2014, doi: 10.1016/j.jpowsour.2013.11.103.

[9] S. S. Zhang, “A review on the separators of liquid electrolyte Li-ion batteries,” *Journal of Power Sources*, vol. 164, no. 1, pp. 351–364, 2007, doi: 10.1016/j.jpowsour.2006.10.065.

[10] C. R. Birkl, M. R. Roberts, E. McTurk, P. G. Bruce, and D. A. Howey, “Degradation diagnostics for lithium ion cells,” *Journal of Power Sources*, vol. 341, no. 1, pp. 373–386, 2017, doi: 10.1016/j.jpowsour.2016.12.011.

[11] J. Vetter *et al.,* “Ageing mechanisms in lithium-ion batteries,” *Journal of Power Sources*, vol. 147, 1-2, pp. 269–281, 2005, doi: 10.1016/j.jpowsour.2005.01.006.

[12] J. Liu, Y. Zhang, J. Bai, L. Zhou, and Z. Wang, “Influence of lithium plating on lithium-ion battery aging at high temperature,” *Electrochimica Acta*, vol. 445, p. 142362, 2023, doi: 10.1016/j.electacta.2023.142362.

[13] T. Waldmann, B.-I. Hogg, and M. Wohlfahrt-Mehrens, “Li plating as unwanted side reaction in commercial Li-ion cells – A review,” *Journal of Power Sources*, vol. 384, pp. 107–124, 2018, doi: 10.1016/j.jpowsour.2018.02.063.

[14] P. Kuntz *et al.,* “Identification of Degradation Mechanisms by Post-Mortem Analysis for High Power and High Energy Commercial Li-Ion Cells after Electric Vehicle Aging,” *Batteries*, vol. 7, no. 3, p. 48, 2021, doi: 10.3390/batteries7030048.

[15] W. Waag, C. Fleischer, and D. U. Sauer, “Critical review of the methods for monitoring of lithium-ion batteries in electric and hybrid vehicles,” *Journal of Power Sources*, vol. 258, pp. 321–339, 2014, doi: 10.1016/j.jpowsour.2014.02.064.

[16] E. Bekaert, L. Buannic, U. Lassi, A. Llordés, and J. Salminen, “Electrolytes for Li- and Na-Ion Batteries: Concepts, Candidates, and the Role of Nanotechnology,” in *Emerging Nanotechnologies in Rechargeable Energy Storage Systems*: Elsevier, 2017, pp. 1–43.

[17] M. B. Pinson and M. Z. Bazant, “Theory of SEI Formation in Rechargeable Batteries: Capacity Fade, Accelerated Aging and Lifetime Prediction,” *J. Electrochem. Soc.*, vol. 160, no. 2, A243-A250, 2013, doi: 10.1149/2.044302jes.

[18] A. Jana, D. R. Ely, and R. E. García, “Dendrite-separator interactions in lithium-based batteries,” *Journal of Power Sources*, vol. 275, pp. 912–921, 2015, doi: 10.1016/j.jpowsour.2014.11.056.

[19] P. G. Balakrishnan, R. Ramesh, and T. Prem Kumar, “Safety mechanisms in lithium-ion batteries,” *Journal of Power Sources*, vol. 155, no. 2, pp. 401–414, 2006, doi: 10.1016/j.jpowsour.2005.12.002.

[20] A. Tomaszewska *et al.,* “Lithium-ion battery fast charging: A review,” *eTransportation*, vol. 1, p. 100011, 2019, doi: 10.1016/j.etran.2019.100011.

[21] T. R. Jow, S. A. Delp, J. L. Allen, J.-P. Jones, and M. C. Smart, “Factors Limiting Li + Charge Transfer Kinetics in Li-Ion Batteries,” *J. Electrochem. Soc.*, vol. 165, no. 2, A361-A367, 2018, doi: 10.1149/2.1221802jes.

[22] N. Legrand, B. Knosp, P. Desprez, F. Lapicque, and S. Raël, “Physical characterization of the charging process of a Li-ion battery and prediction of Li plating by electrochemical modelling,” *Journal of Power Sources*, vol. 245, pp. 208–216, 2014, doi: 10.1016/j.jpowsour.2013.06.130.

[23] C. Uhlmann, J. Illig, M. Ender, R. Schuster, and E. Ivers-Tiffée, “In situ detection of lithium metal plating on graphite in experimental cells,” *Journal of Power Sources*, vol. 279, pp. 428–438, 2015, doi: 10.1016/j.jpowsour.2015.01.046.

[24] S. Ahmed *et al.,* “Enabling fast charging – A battery technology gap assessment,” *Journal of Power Sources*, vol. 367, pp. 250–262, 2017, doi: 10.1016/j.jpowsour.2017.06.055.

[25] R. Chandrasekaran, “Quantification of bottlenecks to fast charging of lithium-ion-insertion cells for electric vehicles,” *Journal of Power Sources*, vol. 271, pp. 622–632, 2014, doi: 10.1016/j.jpowsour.2014.07.106.

[26] Y. Tian, C. Lin, H. Li, J. Du, and R. Xiong, “Detecting undesired lithium plating on anodes for lithium-ion batteries – A review on the in-situ methods,” *Applied Energy*, vol. 300, p. 117386, 2021, doi: 10.1016/j.apenergy.2021.117386.

[27] K.-H. Chen *et al.,* “Dead lithium: mass transport effects on voltage, capacity, and failure of lithium metal anodes,” *J. Mater. Chem. A*, vol. 5, no. 23, pp. 11671–11681, 2017, doi: 10.1039/C7TA00371D.

[28] X. Zhao, Y. Yin, Y. Hu, and S.-Y. Choe, “Electrochemical-thermal modeling of lithium plating/stripping of Li(Ni0.6Mn0.2Co0.2)O2/Carbon lithium-ion batteries at subzero ambient temperatures,” *Journal of Power Sources*, vol. 418, pp. 61–73, 2019, doi: 10.1016/j.jpowsour.2019.02.001.

[29] D. Hu *et al.,* “Research Progress of Lithium Plating on Graphite Anode in Lithium-Ion Batteries,” *Chin. J. Chem.*, vol. 39, no. 1, pp. 165–173, 2021, doi: 10.1002/cjoc.202000512.

[30] F. Sagane, K.-i. Ikeda, K. Okita, H. Sano, H. Sakaebe, and Y. Iriyama, “Effects of current densities on the lithium plating morphology at a lithium phosphorus oxynitride glass electrolyte/copper thin film interface,” *Journal of Power Sources*, vol. 233, pp. 34–42, 2013, doi: 10.1016/j.jpowsour.2013.01.051.

[31] N. Ghanbari, T. Waldmann, M. Kasper, P. Axmann, and M. Wohlfahrt-Mehrens, “Inhomogeneous Degradation of Graphite Anodes in Li-Ion Cells: A Postmortem Study Using Glow Discharge Optical Emission Spectroscopy (GD-OES),” *J. Phys. Chem. C*, vol. 120, no. 39, pp. 22225–22234, 2016, doi: 10.1021/acs.jpcc.6b07117.

[32] C. Birkenmaier, B. Bitzer, M. Harzheim, A. Hintennach, and T. Schleid, “Lithium Plating on Graphite Negative Electrodes: Innovative Qualitative and Quantitative Investigation Methods,” *J. Electrochem. Soc.*, vol. 162, no. 14, A2646-A2650, 2015, doi: 10.1149/2.0451514jes.

[33] J. Cannarella and C. B. Arnold, “The Effects of Defects on Localized Plating in Lithium-Ion Batteries,” *J. Electrochem. Soc.*, vol. 162, no. 7, A1365-A1373, 2015, doi: 10.1149/2.1051507jes.

[34] Y. Ji, Y. Zhang, and C.-Y. Wang, “Li-Ion Cell Operation at Low Temperatures,” *J. Electrochem. Soc.*, vol. 160, no. 4, A636-A649, 2013, doi: 10.1149/2.047304jes.

[35] S. Ma *et al.,* “Temperature effect and thermal impact in lithium-ion batteries: A review,” *Progress in Natural Science: Materials International*, vol. 28, no. 6, pp. 653–666, 2018, doi: 10.1016/j.pnsc.2018.11.002.

[36] S. Zhang, K. Xu, and T. Jow, “Low-temperature performance of Li-ion cells with a LiBF4-based electrolyte,” *J Solid State Electrochem*, vol. 7, no. 3, pp. 147–151, 2003, doi: 10.1007/s10008-002-0300-9.

[37] F. B. Spingler, S. Friedrich, S. Kücher, S. Schmid, D. López-Cruz, and A. Jossen, “The Effects of Non-Uniform Mechanical Compression of Lithium-Ion Cells on Local Current Densities and Lithium Plating,” *J. Electrochem. Soc.*, vol. 168, no. 11, p. 110515, 2021, doi: 10.1149/1945-7111/ac33e1.

[38] G. Fuchs, L. Willenberg, F. Ringbeck, and D. U. Sauer, “Post-Mortem Analysis of Inhomogeneous Induced Pressure on Commercial Lithium-Ion Pouch Cells and Their Effects,” *Sustainability*, vol. 11, no. 23, p. 6738, 2019, doi: 10.3390/su11236738.

[39] Z. Li, J. Huang, B. Yann Liaw, V. Metzler, and J. Zhang, “A review of lithium deposition in lithium-ion and lithium metal secondary batteries,” *Journal of Power Sources*, vol. 254, pp. 168–182, 2014, doi: 10.1016/j.jpowsour.2013.12.099.

[40] X. Xu *et al.,* “Recent progresses in the suppression method based on the growth mechanism of lithium dendrite,” *Journal of Energy Chemistry*, vol. 27, no. 2, pp. 513–527, 2018, doi: 10.1016/j.jechem.2017.11.010.

[41] P. P. Paul *et al.,* "A Review of Existing and Emerging Methods for Lithium Detection and Characterization in Li-Ion and Li-Metal Batteries," *Adv. Energy Mater.*, vol. 11, no. 17, p. 2100372, 2021, doi: 10.1002/aenm.202100372.

[42] S. Schindler, M. Bauer, M. Petzl, and M. A. Danzer, "Voltage relaxation and impedance spectroscopy as in-operando methods for the detection of lithium plating on graphitic anodes in commercial lithium-ion cells," *Journal of Power Sources*, vol. 304, pp. 170–180, 2016, doi: 10.1016/j.jpowsour.2015.11.044.

[43] M. Petzl and M. A. Danzer, "Nondestructive detection, characterization, and quantification of lithium plating in commercial lithium-ion batteries," *Journal of Power Sources*, vol. 254, pp. 80–87, 2014, doi: 10.1016/j.jpowsour.2013.12.060.

[44] Y. Chen *et al.,* "Operando detection of Li plating during fast charging of Li-ion batteries using incremental capacity analysis," *Journal of Power Sources*, vol. 539, no. 4, p. 231601, 2022, doi: 10.1016/j.jpowsour.2022.231601.

[45] X.-G. Yang, S. Ge, T. Liu, Y. Leng, and C.-Y. Wang, "A look into the voltage plateau signal for detection and quantification of lithium plating in lithium-ion cells," *Journal of Power Sources*, vol. 395, pp. 251–261, 2018, doi: 10.1016/j.jpowsour.2018.05.073.

[46] I. D. Campbell, M. Marzook, M. Marinescu, and G. J. Offer, "How Observable Is Lithium Plating? Differential Voltage Analysis to Identify and Quantify Lithium Plating Following Fast Charging of Cold Lithium-Ion Batteries," *J. Electrochem. Soc.*, vol. 166, no. 4, A725-A739, 2019, doi: 10.1149/2.0821904jes.

[47] J. Sieg *et al.,* "Local degradation and differential voltage analysis of aged lithium-ion pouch cells," *Journal of Energy Storage*, vol. 30, no. 1, p. 101582, 2020, doi: 10.1016/j.est.2020.101582.

[48] F. Ringbeck, C. Rahe, G. Fuchs, and D. U. Sauer, "Identification of Lithium Plating in Lithium-Ion Batteries by Electrical and Optical Methods," *J. Electrochem. Soc.*, vol. 167, no. 9, p. 90536, 2020, doi: 10.1149/1945-7111/ab8f5a.

[49] I. Bloom *et al.,* "Differential voltage analyses of high-power, lithium-ion cells," *Journal of Power Sources*, vol. 139, 1-2, pp. 295–303, 2005, doi: 10.1016/j.jpowsour.2004.07.021.

[50] A. Adam, E. Knobbe, J. Wandt, and A. Kwade, "Application of the differential charging voltage analysis to determine the onset of lithium-plating during fast charging of lithium-ion cells," *Journal of Power Sources*, vol. 495, p. 229794, 2021, doi: 10.1016/j.jpowsour.2021.229794.

[51] Z. M. Konz, E. J. McShane, and B. D. McCloskey, "Detecting the Onset of Lithium Plating and Monitoring Fast Charging Performance with Voltage Relaxation," *ACS Energy Lett.*, vol. 5, no. 6, pp. 1750–1757, 2020, doi: 10.1021/acsenergylett.0c00831.

[52] M. Berecibar, M. Dubarry, I. Villarreal, N. Omar, and J. van Mierlo, "Degradation Mechanisms Detection for HP and HE NMC Cells Based on Incremental Capacity Curves," in *2016 IEEE Vehicle Power and Propulsion Conference (VPPC)*, Hangzhou, China, Oct. 2016 - Oct. 2016, pp. 1–5.

[53] M. Dubarry, V. Svoboda, R. Hwu, and B. Yann Liaw, "Incremental Capacity Analysis and Close-to-Equilibrium OCV Measurements to Quantify Capacity Fade in Commercial Rechargeable Lithium Batteries," *Journal of Power Sources*, vol. 9, no. 10, A454, 2006, doi: 10.1149/1.2221767.

[54] M. Dubarry and D. Anseán, “Best practices for incremental capacity analysis,” *Front. Energy Res.*, vol. 10, 2022, doi: 10.3389/fenrg.2022.1023555.

[55] X. Han, M. Ouyang, L. Lu, J. Li, Y. Zheng, and Z. Li, “A comparative study of commercial lithium ion battery cycle life in electrical vehicle: Aging mechanism identification,” *Journal of Power Sources*, vol. 251, pp. 38–54, 2014, doi: 10.1016/j.jpowsour.2013.11.029.

[56] S. P. Rangarajan, Y. Barsukov, and P. P. Mukherjee, “In operando signature and quantification of lithium plating,” *J. Mater. Chem. A*, vol. 7, no. 36, pp. 20683–20695, 2019, doi: 10.1039/C9TA07314K.

[57] R. Raccichini, M. Amores, and G. Hinds, “Critical Review of the Use of Reference Electrodes in Li-Ion Batteries: A Diagnostic Perspective,” *Batteries*, vol. 5, no. 1, p. 12, 2019, doi: 10.3390/batteries5010012.

[58] E. McTurk, C. R. Birkl, M. R. Roberts, D. A. Howey, and P. G. Bruce, “Minimally Invasive Insertion of Reference Electrodes into Commercial Lithium-Ion Pouch Cells,” *ECS Electrochemistry Letters*, vol. 4, no. 12, A145-A147, 2015, doi: 10.1149/2.0081512eel.

[59] Technische Universität Graz, *Battery Safety Center Graz.* [Online]. Available: https://www.tugraz.at/sites/bscg/home/

[60] Nigel, *LG E66a: Battery Design*. from chemistry to pack. [Online]. Available: https://www.batterydesign.net/lg-e66a/

[61] L. Kong, Y. Xing, and M. G. Pecht, “<italic>In-Situ</italic> Observations of Lithium Dendrite Growth,” *IEEE Access*, vol. 6, pp. 8387–8393, 2018, doi: 10.1109/ACCESS.2018.2805281.

[62] M. Lewerenz, A. Marongiu, A. Warnecke, and D. U. Sauer, “Differential voltage analysis as a tool for analyzing inhomogeneous aging: A case study for LiFePO4|Graphite cylindrical cells,” *Journal of Power Sources*, vol. 368, pp. 57–67, 2017, doi: 10.1016/j.jpowsour.2017.09.059.

[63] M. Raić *et al.,* “Nanostructured Silicon as Potential Anode Material for Li-Ion Batteries,” *Molecules (Basel, Switzerland)*, vol. 25, no. 4, 2020, doi: 10.3390/molecules25040891.

[64] H. Wang *et al.,* “Underpotential lithium plating on graphite anodes caused by temperature heterogeneity,” *Proceedings of the National Academy of Sciences of the United States of America*, vol. 117, no. 47, pp. 29453–29461, 2020, doi: 10.1073/pnas.2009221117.

A APPENDIX

A.1 Additional test results

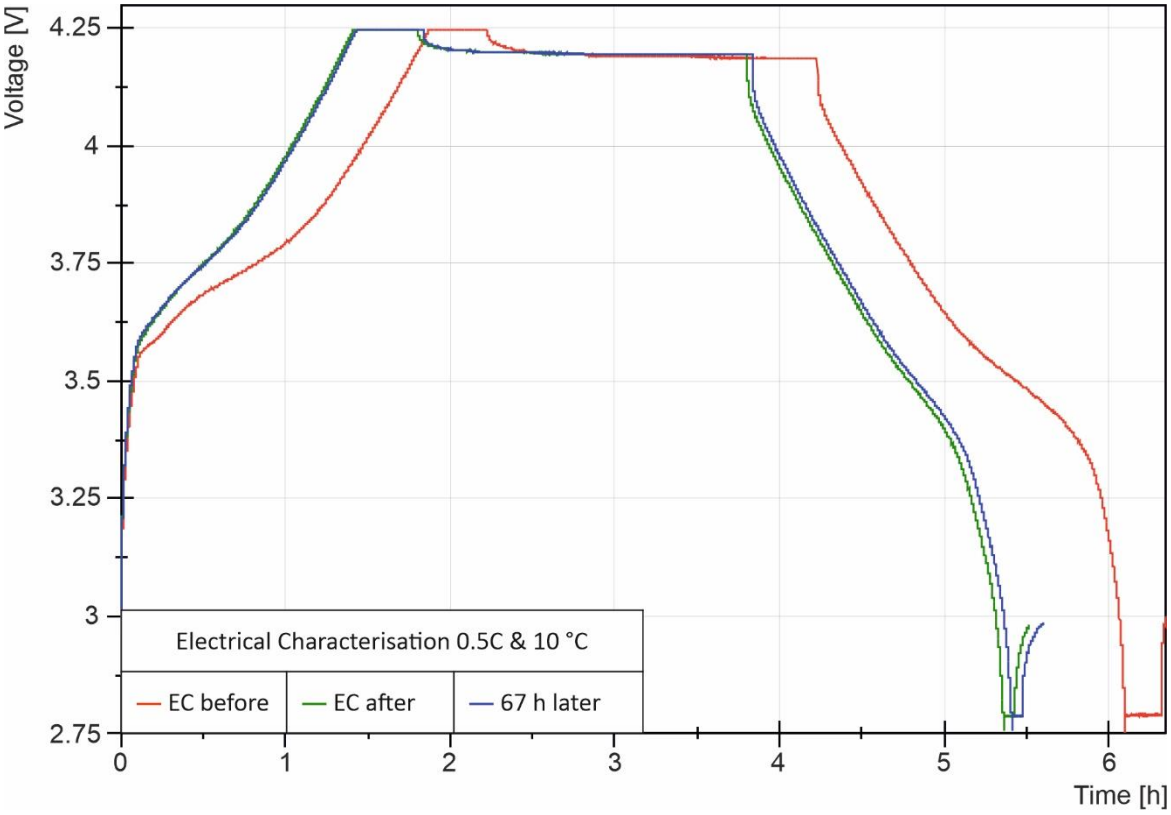

Figure Appendix A.1-1: Electrical Characterization test cell 2- before vs. after 20 cycles vs. 67 h later

A.2 Instrumentation

A.2.1 Charging device – Power supply

Manufacturer	**Elektro-Automatic**
Model	EA-PSI 9080-340
Product type	DC Laboratory power supply
Housing	19'' rack
Max voltage	80 V
Output voltage accuracy	< 0.1 %
Max current	340 A
Output current accuracy	< 0.02 %
Max power	10 kW
Output power accuracy	< 1 %
Slew rate 10% - 90%	< 30 ms
Operation temperature	0-50 °C

Table Appendix A.2-1: Data information about the Elektronik-Automatic power supply EA-PSI 9080-340

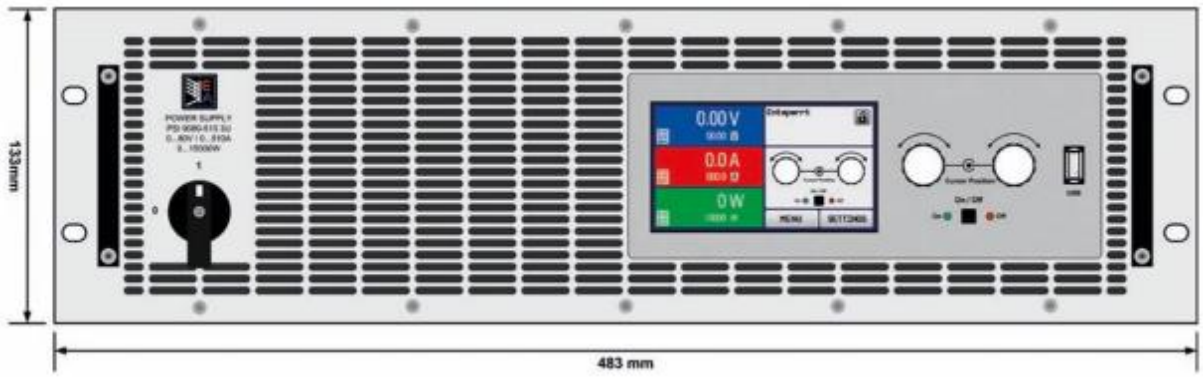

Figure Appendix A.2-1: Front view of the Elektro-Automatik power supply

A.2.2 Discharging device – Electronic load

Manufacturer	**Elektro-Automatic**
Model	EA-EL 9080-340 B
Product type	DC electronic load
Housing	19'' rack
Max voltage	80 V
Input voltage accuracy	< 0.1 %
Max current	340 A
Input current accuracy	< 0.2 %
Max power	4800 kW
Input power accuracy	< 0.5 %
Resistance	0.03 – 7.5 Ω
Resistance accuracy	≤ 1 % + 0.3 % of nominal current
Operation temperature	0-50 °C

Table Appendix A.2-2: Data information about the Elektronik-Automatic electronic load EA-EL 9080-340 B

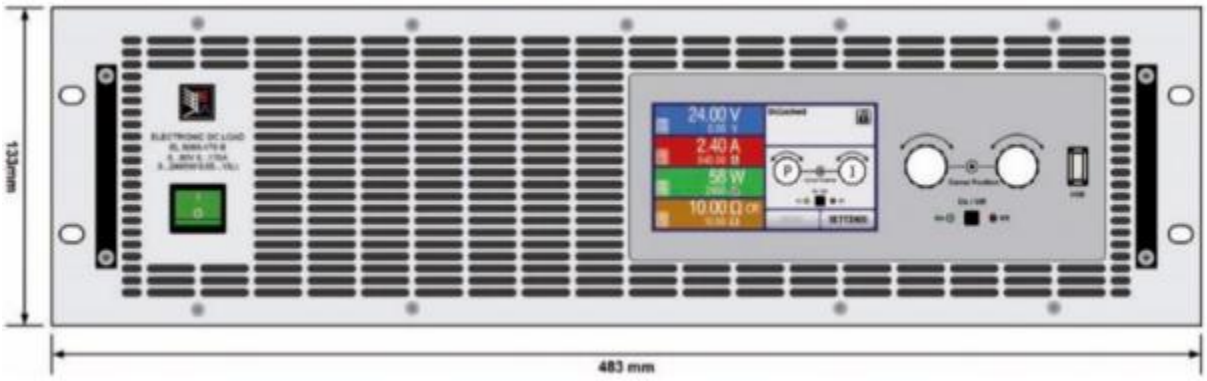

Figure Appendix A.2-2: Front view of the Elektro-Automatik electronic load

A.2.3 Pressure distribution measurement

This section shows the results of the pressure distribution measurement for two cells with and without the impactor.

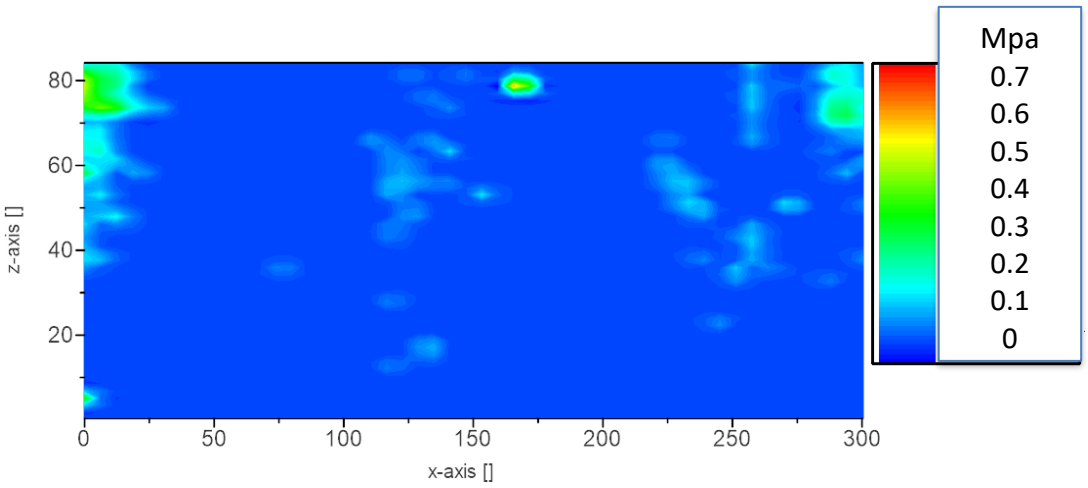

Figure Appendix A.2-3: Pressure distribution of cell F.1.12.6 without impactor

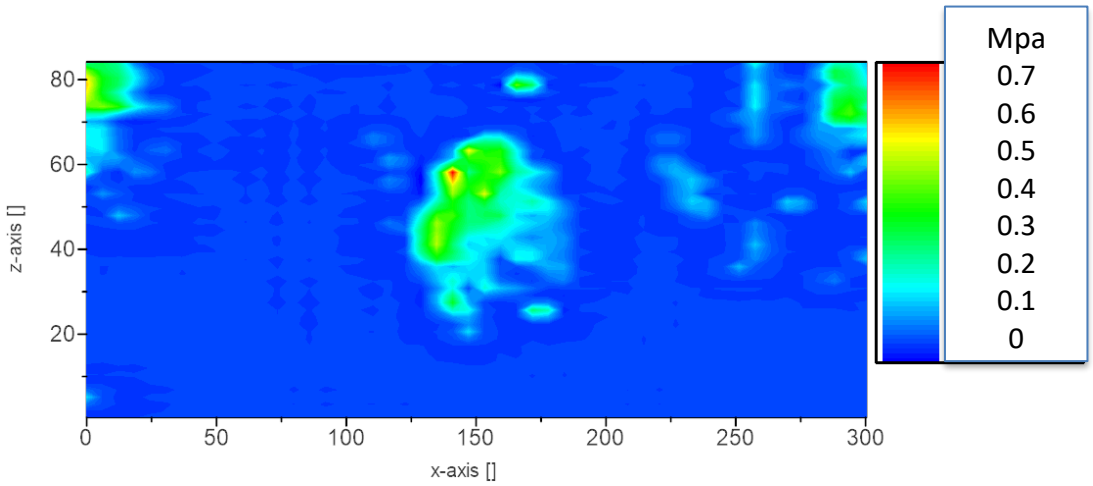

Figure Appendix A.2-4: Pressure distribution of cell F.1.12.6 with impactor

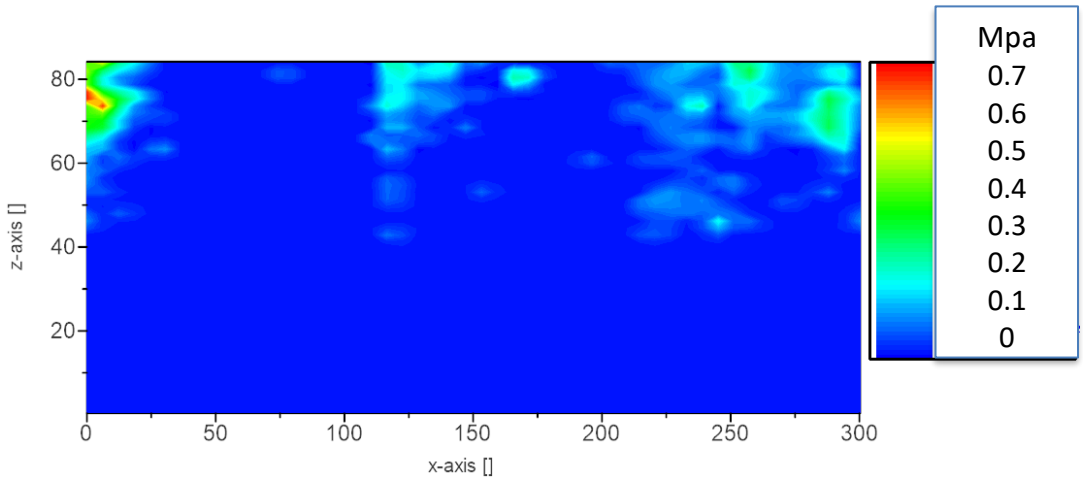

Figure Appendix A.2-5: Pressure distribution of cell F.1.12.7 without impactor

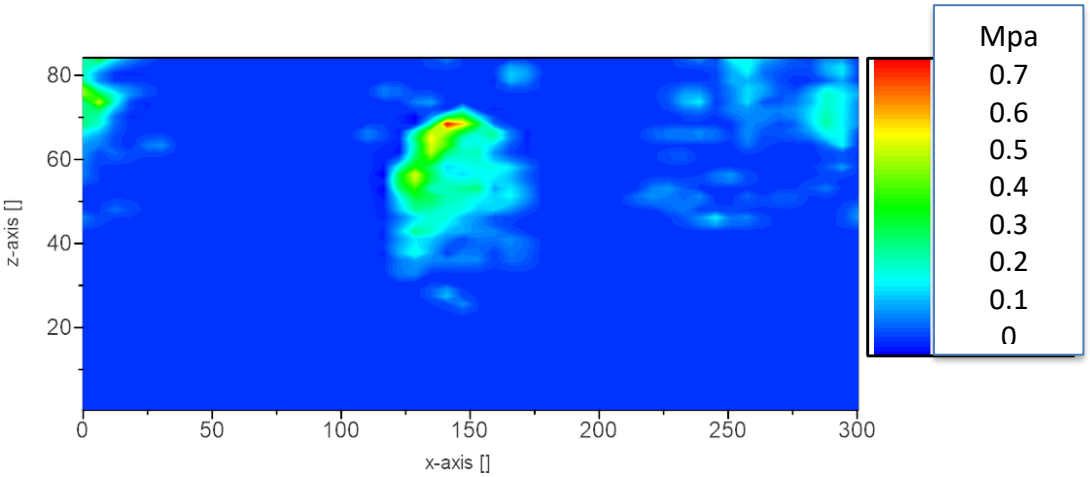

Figure Appendix A.2-6: Pressure distribution of cell F.1.12.7 with impactor

A.2.4 Cycling protocol main-study

Steps	Action	
1	Charge to 100 % SOC	**Electrical Characterization**
2	Relaxation period of t= 7200 s	
3	Discharge to 0 % SOC	
4	Waiting period of t= 900 s = 15 min	
5	Charge to 90 % SOC	**Cycle 1**
6	Relaxation period of t= 5400 s	
7	Discharge to 0 % SOC	
8	Waiting period of t= 900 s = 15 min	
9	Charge to 90 % SOC	**Cycle 2**
10	Discharge to 0 % SOC	
11	Waiting period of t= 900 s = 15 min	
12	Charge to 90 % SOC	**Cycle 3**
13	Discharge to 0 % SOC	
14	Waiting period of t= 900 s = 15 min	
15	Charge to 90 % SOC	**Cycle 4**
16	Discharge to 0 % SOC	
17	Waiting period of t= 900 s = 15 min	
18	Charge to 90 % SOC	**Cycle 5**
19	Relaxation period of t= 5400 s	
20	Discharge to 0 % SOC	
21	Waiting period of t= 900 s = 15 min	
22	Charge to 90 % SOC	**Cycle 6**
23	Discharge to 0 % SOC	
24	Waiting period of t= 900 s = 15 min	
25	Charge to 90 % SOC	**Cycle 7**
26	Discharge to 0 % SOC	
27	Waiting period of t= 900 s = 15 min	
28	Charge to 90 % SOC	**Cycle 8**
29	Discharge to 0 % SOC	
30	Waiting period of t= 900 s = 15 min	

31	Charge to 90 % SOC	**Cycle 9**
32	Discharge to 0 % SOC	
33	Waiting period of t= 900 s = 15 min	
34	Charge to 90 % SOC	**Cycle 10**
35	Relaxation period of t= 5400 s	
36	Discharge to 0 % SOC	
37	Waiting period of t= 900 s = 15 min	
38	Charge to 90 % SOC	**Cycle 11**
39	Discharge to 0 % SOC	
40	Waiting period of t= 900 s = 15 min	
41	Charge to 90 % SOC	**Cycle 12**
42	Discharge to 0 % SOC	
43	Waiting period of t= 900 s = 15 min	
44	Charge to 90 % SOC	**Cycle 13**
45	Discharge to 0 % SOC	
46	Waiting period of t= 900 s = 15 min	
47	Charge to 90 % SOC	**Cycle 14**
48	Discharge to 0 % SOC	
49	Waiting period of t= 900 s = 15 min	
50	Charge to 90 % SOC	**Cycle 15**
51	Relaxation period of t= 5400 s	
52	Discharge to 0 % SOC	
53	Waiting period of t= 900 s = 15 min	
54	Charge to 90 % SOC	**Cycle 16**
55	Discharge to 0 % SOC	
56	Waiting period of t= 900 s = 15 min	
57	Charge to 90 % SOC	**Cycle 17**
58	Discharge to 0 % SOC	
59	Waiting period of t= 900 s = 15 min	

60	Charge to 90 % SOC	**Cycle 18**
61	Discharge to 0 % SOC	
62	Waiting period of t= 900 s = 15 min	
63	Charge to 90 % SOC	**Cycle 19**
64	Discharge to 0 % SOC	
65	Waiting period of t= 900 s = 15 min	
66	Charge to 90 % SOC	**Cycle 20**
67	Relaxation period of t= 5400 s	
68	Discharge to 0 % SOC	
69	Waiting period of t= 900 s = 15 min	
86	Charge to 100 % SOC	**Electrical Characterization**
87	Relaxation period of t= 7200 s	
88	Discharge to 0 % SOC	
89	Waiting period of t= 900 s = 15 min	

Table Appendix A.2-3: Complete steps of cycling protocol from main-study

A.3 Guidelines

A.3.1 List of abbreviations

Abbreviation	Explanation
AP	Anode potential
BC	Boundary condition
BSCG	Battery Safety Center Graz
BMS	Battery management system
BEV	Battery electric vehicle
CC	Constant current
CV	Constant voltage
DAQ	Data acquisition system
DVA	Differential voltage analysis
EC	Electrical characterization
EV	Electric vehicle
ICA	Incremental capacity analysis
ICTM	Institute of Chemistry & Technology of Materials
LAM	Loss of active material
LE	Loss of electrolyte
LFP	Lithium Iron Phosphate
LIB	Lithium ion battery
LLI	Loss of lithium inventory
LP	Lithium plating
Max.	Maximum
Min.	Minimum
NMC	Nickel manganese cobalt
OCV	Open circuit voltage
RE	Reference electrode
SEI	Solid electrolyte interface
SOC	State of Charge
SoH	State of Health
VRP	Voltage Relaxation Profile

A.3.2 List of measurement units

µm	**Micrometre**	**Length**	$\mathbf{1 \times 10^6 m}$
A	Ampere	Electric current	$\mathbf{A}$
°C	Celsius	Temperature	$\mathbf{°C}$
Hz	Hertz	Frequency	$\boldsymbol{s^{-1}}$
kg	Kilograms	Mass	$\mathbf{kg}$
kN	Kilonewton	Force	$(\mathbf{kg} \times \mathbf{m} \times \boldsymbol{s^{-2}}) \times \mathbf{10^3}$
kW	Kilowatt	Power	$(\mathbf{kg} \times \boldsymbol{m^2} \times \boldsymbol{s^{-3}}) \times \mathbf{10^3}$
mm	Millimetre	Length	$\mathbf{mm}$
m	Metre	Length	$\mathbf{m}$
MPa	Megapascal	Pressure	$(\mathbf{kg} \times \boldsymbol{m^{-1}} \times \boldsymbol{s^{-2}}) \times \mathbf{10^6}$
N	Newton	Force	$\mathbf{kg} \times \mathbf{m} \times \boldsymbol{s^{-2}}$
s	Seconds	Time	$\mathbf{s}$
V	Volt	Voltage	$\mathbf{kg} \times \boldsymbol{m^2} \times \boldsymbol{s^{-3}} \times \boldsymbol{A^{-1}}$
W	Watt	Power	$\mathbf{kg} \times \boldsymbol{m^2} \times \boldsymbol{s^{-3}}$